

Thesis for the degree
Master of Science

Submitted to the Scientific Council of the
Weizmann Institute of Science
Rehovot, Israel

By
Michael Pitt

עבודת גמר (תזה) לתואר
מוסמך למדעים

מוגשת למועצה המדעית של
מכון ויצמן למדע
רחובות, ישראל

מאת
מיכאל פיט

מחקר ניסיוני בפיסיקת חלקיקים: פיתוח גלאי וניתוח תוצאות
Experimental research in particle physics:
Detector development and data analysis

Advisors:
Prof. Amos Breskin
Prof. Eilam Gross

מנחים:
פרופ' עמוס ברסקין
פרופ' עילם גרוס

March 2012

ניסן תשע"ב

Abstract

The thesis work reflects my motivation of getting a broad experience and expertise in experimental physics, more precisely in: Particle-, Astroparticle- and Detector Physics. The latter is the basis for any modern experiments in Particle- and Astroparticle-Physics. Therefore, the work has been divided into detector development activities towards applications at the future International Linear Collider (ILC) as well as to data analysis related to two front-edge topics: the search for the Higgs boson (within CERN-ATLAS detector) and for Dark matter (within XENON100).

The work below summarizes, in three different chapters, the highlights of my activities.

Acknowledgments

It is my pleasure to thank all those who assisted me during my M.Sc thesis research work at the Weizmann Institute of Science.

First and foremost, I would like to extend special thanks to my supervisors **Prof. Amos Breskin** and **Prof. Eilam Gross** who granted me an opportunity to participate in the various experimental research fields in high energy physics, by guiding my projects using their huge knowledge and experience. A very special thanks to **Prof. Ehud Duchovni** who was the first to introduce me to the enchanting world of the Experimental High Energy Physics.

To **Dr. Lior Arazi** for his assistance during my work in the radiation detector physics laboratory, guiding me with his new and elegant ideas and especially for his delicate assistance in the writing effort.

To **Ohad Silbert** for sharing his large experience in working on the ATLAS experiment, for a conceptual guidance and invaluable assistance in his qualitative way of thinking, bringing always new and successful ideas.

To **Dr. Hagar Landsman** for her assistance in the work related to the XENON Dark-Matter search experiment and during for the writing process.

To my collaborators from the Weizmann XENON group, **Dr. Daniel Lelouch**, **Nadav Priel**, **Etai Nativ** and **Ofer Vitells**.

To my lab mates and colleagues from the radiation detection physics laboratory, **Adam Rubin**, **Dr. Sana Shilstein**, **Dr. Sergei Shchemelinin**, **Dr. Marco Cortesi**, **Itamar Israelashvilli** and **Luca Moleri** for many useful discussions.

To **Andrew Wilson**, **Joe Davighi** and **Sebastian Najera** from International Summer Science Institute (ISSI) program for taking a part in the R&D work.

To **Gal Dadiani** supporting the ALTAS group PC farm.

To the electronics lab staff, **Yafa Gil** and **Yaron Gal** and to the workshop master **Yehuda Asher**.

Last but not least, to our laboratory technician **Moshe Klin**.

Preface

What is the nature of the universe? What is the world made of? What holds it together? These questions occupied the minds of scientists and philosophers for thousands of years. The internal structure of the atom began to unravel at the end of the 19th century, with the discovery of the electron by J.J. Thomson in 1897.

The first half of the 20th century was marked by the discovery of the proton in 1919 by E. Rutherford, neutron in the 1932 by J. Chadwick are constitute the atomic nucleus. In the same year (1932) the first anti-particle, the positron, was discovered by Carl D. Anderson. Parallel developments of particle detectors in the following decades paved way towards the discovery of hundreds of particles, leading to a complex puzzle of the subatomic-particles world. Within this "particle zoo" the question whether these particles are elementary or not, concerned the mind of scientists in the mid of the 20th century.

Solutions to the puzzle began to emerge with the finalization in the 1970s of the Standard Model of particle physics - the theory that describes the elementary particles and their interactions. The great triumph of the Standard Model was the correct prediction of the W- and Z-boson masses before their discovery in 1983 at CERN. A decade later, with the discovery of the top quark (1995) and the tau neutrino (2000) at Fermilab, only one standard model particle remains undiscovered - the Higgs boson.

At present, the CERN Large Hadron Collider (LHC) is approaching the highest-energy man-made particle collisions. One of its main purposes is the discovery of this last particle predicted by the Standard Model. The search for the very rare Higgs boson events is very challenging, requiring sophisticated analysis.

Although the Higgs discovery at the LHC is probable, there will remain some unanswered questions. There are evidences that the physics described by the Standard Model is incomplete, e.g. the evidence of accelerating universe against the gravitational forces, pointing at the presence of an unknown energy (Dark energy); the fast rotation of the galaxies and cluster of galaxies that contradict Newtonian dynamics relaying only on a visible matter pointing of an existence of an unseen (Dark) matter.

To be able to answer these intriguing questions, regarding our own universe, more sophisticated experiments must be conceived. Development of a future particle detectors is the basis for any novel experimental research efforts in particle physics and astro-particle physics.

Participating in detector development for the future experiments, like that foreseen at the ILC, and taking a part in the analysis of the current ones, constituted an invaluable opportunity to be part of the front-edge experimental research, dealing with the most fascinating questions that challenge the human mind.

This thesis is touching all of the High Energy Physics frontiers described above: the development of future detectors and searches for the Higgs boson and Dark Matter.

The structure of the thesis is the following:

The first part, chapter 1, contains detector development activities towards applications at the future International Linear Collider (ILC) in particularly the development of potential gas-avalanche sampling elements for the Digital Hadronic Calorimeter of the Silicon Detector (SiD). In this work we investigated very thin sampling configurations based on a novel-geometry of a Thick Gas Electron Multiplier (THGEM)-based detector, developed at the Weizmann Institute's Radiation Detector Physics Laboratory. The proposed sampling elements should permit stable operation at high efficiency, in a highly ionizing environment expected in the future particle experiments our development is expected to have a broad scope of other applications.

The second part, is a Data Analysis related to two front-edge topics:

- Chapter 2 describes the Higgs boson searches with the ATLAS experiment of the Large Hadron Collider (CERN-LHC). Here we concentrated on a specific Higgs boson decay channel, where the Higgs decays also into a pair of tau leptons which decay leptonically. $H \rightarrow \tau_{lep}\tau_{lep}$ events, are associated with a presence of four elusive neutrinos which remain undetected, thus challenging the reconstruction of the Higgs mass. We studied a novel mass reconstruction technique which despite the presence of unmeasured particles, has a significant reconstruction ability.
- Chapter 3 describes my contribution on the analysis of a searches for Dark Matter with the XENON100 liquid-xenon TPC experiment at Gran Sasso national laboratory - LNGS. In the absence of a significant signal of Dark-Matter related weakly interacting particles (WIMPs) we studied and obtained a spin-dependent cross section limit of Dark Matter particle interactions.

Even though the thesis is made of three parts, they are all related to experimental high energy physics at its frontiers.

Contents

I	Detector development	1
1	R&D towards thin, THGEM-based sampling elements for digital hadronic calorimetry.	2
1.1	Introduction	2
1.1.1	Digital Hadronic Calorimeter of the ILC-SiD	3
1.1.2	Active sampling elements for DHCAL	4
1.1.3	The Thick Gas Electron Multiplier (THGEM)	6
1.1.4	Motivation and Goals	8
1.2	Beam tests of THGEM-based sampling elements	9
1.2.1	Experimental setup and methodology	9
1.2.2	Beam test results	11
1.2.3	Conclusions	13
1.3	The Thick-WELL (THWELL)	13
1.3.1	Structure and motivation	13
1.3.2	Gain	14
1.3.3	Pulse shape	19
1.3.4	Study of discharges in the THWELL and induction-gap configurations	20
1.3.5	Discussion	23
1.4	Well-THGEM with resistive anode (RWELL)	24
1.4.1	Motivation	24
1.4.2	Geometry and preparation	24
1.4.3	Gain and pulse measurements	25
1.4.4	Discharges with a resistive anode	26
1.4.5	Gain vs. Rate	26
1.4.6	Charge propagation	26
1.4.7	Cross-talk measurements	31
1.4.8	Discussion	32
1.5	Segmented-GRWELL	33
1.5.1	Motivation	33
1.5.2	Configuration	33
1.5.3	Segmented-GRWELL electron collection efficiency	34
1.5.4	Transparency measurements	35
1.6	Summary, conclusion and discussion	36

II Data Analysis 39

2	Mass reconstruction technique in di-tau resonances for Higgs searches with ATLAS detector	40
2.1	Introduction	40
2.2	Experiment	42
2.2.1	ATLAS detector	42
2.3	Standard model of particle physics	45
2.3.1	Overview	45
2.3.2	Electroweak Gauge Theory	45
2.3.3	Higgs mechanism and the EW symmetry breaking	46
2.3.4	Fermion mass	47
2.4	Higgs $\rightarrow \tau\tau \rightarrow e\mu + 4\nu$ decay channel analysis	48
2.4.1	Higgs production	48
2.4.2	Background	49
2.4.3	Object reconstruction	49
2.4.4	Event selection	50
2.5	Mass reconstruction algorithms in $H \rightarrow \tau\tau$ searches	51
2.5.1	Visible mass	51
2.5.2	Effective mass	51
2.5.3	Collinear approximation	52
2.5.4	MMC algorithm	54
2.6	Modified MMC algorithm	56
2.6.1	Limitation of the old MMC algorithm	56
2.6.2	Modified MMC algorithm	58
2.6.3	MMC Systematics study	61
2.6.4	\cancel{E}_T correction method	62
2.7	Results and conclusions	63
3	Spin Dependent Cross section analysis for XENON100 experiment	65
3.1	Introduction	65
3.1.1	Observational evidence of Dark Matter	66
3.2	Direct detection of DM	66
3.2.1	DM distribution in MW galaxy	67
3.2.2	Rate of WIMP-nucleus interaction	67
3.2.3	Cross section calculation	68
3.3	XENON100 experiment	70
3.4	Setting SD limit	71
3.4.1	Model independent approach	71
3.4.2	Form factors and spin expectation values	72
3.4.3	Systematic unc. from velocity distribution	74
3.4.4	Results	75
3.4.5	Summary	75

List of Figures 79

Bibliography 82

Part I

Detector development

R&D towards thin, THGEM-based sampling elements for digital hadronic calorimetry.

1.1 Introduction

On 30 March 2010 a collision of the first 3.5 TeV proton beams took place at the CERN Large Hadron Collider (LHC), opening a new era of discoveries in fundamental interactions of particle physics. By testing the high energy scale, one of the LHC goals is the discovery of new physics, such as the Higgs boson or other hypothetical particles predicted by various models beyond the Standard Model (SM).

Protons are composite subatomic particles made up of quarks. The rest mass of the quarks contributes about 1% of the proton rest mass, the remaining mass is due to the kinetic energy of the quarks and the energy of the gluon fields that bind them together. Therefore the measurements of fundamental interactions from the colliding protons become less precise due to their composition. While the LHC discoveries will most probably point at some new physics, precise measurements of such physics will be essential.

By colliding truly fundamental particles - electrons with positrons, the future International Linear Collider (ILC) would provide results with extraordinary precision. Consisting of two linear accelerators along 31 km (see figure 1.1.1), the ILC will accelerate these light leptons up to center of mass energy of $\sqrt{s}=500$ GeV, with planned energy upgrade to $\sqrt{s} \sim 1$ TeV [1].

Two complex detectors are considered for the ILC: the International Large Detector (ILD) and the Silicon Detector (SiD). In order to optimize jet energy measurements, the SiD [2], incorporates the Particle Flow Analysis (PFA) [3] strategy as a basic element of its philosophy and design. The basic idea is to measure the momenta of charged particles in the tracker, measure neutral particles in the calorimeter and then add the charged and neutral components together. The challenge is identifying the energy which charged particles deposit in the calorimeters, and discriminating it from the energy deposited by photons and neutral hadrons, so it can be removed.

The SiD design comprises a powerful silicon pixel vertex detector, silicon strips tracker, silicon-tungsten electromagnetic calorimeter, highly segmented hadronic calorimeter, and a muon identification system (see detector scheme in figure 1.1.2). The hadronic calorimeter lies inside a 5T magnetic field created by a superconducting solenoid. SiD calorimetry, requires highly segmented readout, both transversely and longitudinally, in both the electromagnetic and hadronic calorimeters, to allow track reconstruction.

In this thesis chapter we describe the research and development work of novel gas-avalanche sampling elements for the Digital Hadronic Calorimeter (DHCAL) of the SiD. The work is

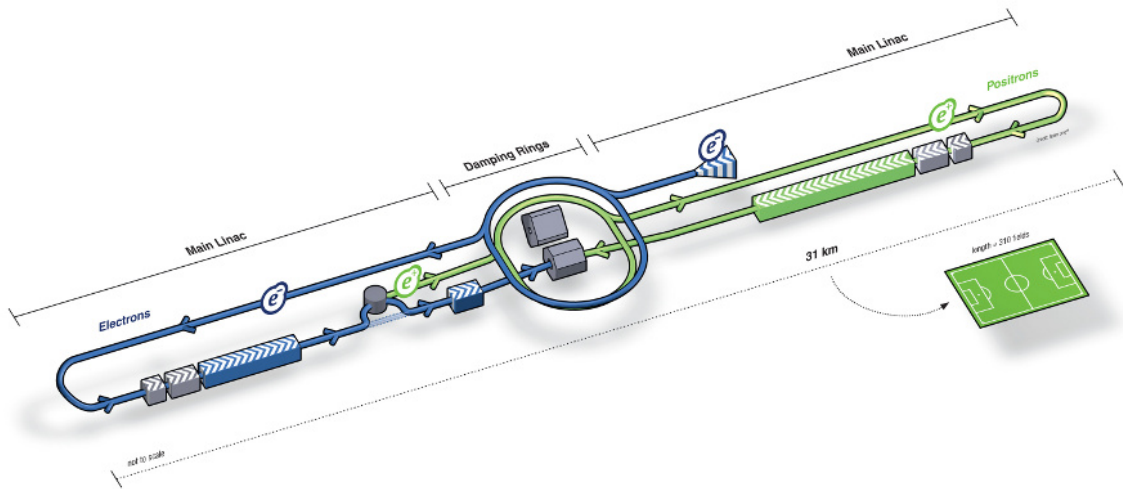


Figure 1.1.1: Schematic layout of ILC (www.linearcollider.org)



Figure 1.1.2: Illustration of a quadrant of SiD (dimensions in mm). From ref. [2]

concentrated on development of a thin, highly efficient detector, with a fine transverse readout segmentation, e.g. 1 cm^2 pixels.

In the following introduction we briefly overview the needs from the ILC DHCAL detectors, and summarize the current existing potential techniques; we motivate the proposed promising sampling elements based on the novel Thick Gaseous Electron Multipliers (THGEM) concept, developed at Weizmann Institute.

In section 1.2 we review the assembly of a THGEM detector prototype, with a summary of the beam test results at CERN; in the sections 1.3, 1.4 and 1.5 we present the results of our study towards thinner and stable THGEM-based detectors and in section 1.6 we summarize the present work in this field.

1.1.1 Digital Hadronic Calorimeter of the ILC-SiD

The DHCAL of the SiD has been proposed for facilitating and improving jet-energy resolution in precise physics measurements. Digital recording of jet-induced hits with pixelated gas sampling elements, accompanied by advanced pattern recognition algorithms (PFA; see above) are

expected to yield very high-precision jet-energy measurements with $\Delta E/E_{jet} = 3\text{-}4\%$ [2, 3].

The baseline design of the SiD DHCAL comprises 40 layers of stainless steel absorber plates (passive material) interlaced by 8 mm thick active sampling gaps, incorporating 1 cm² square pixels and thin readout electronics hybrids [2]. The total absorber depth amounts to $4.5\lambda_A$ ¹. The incoming particles, when passing an absorber, induce multiparticle showers via electromagnetic or/and nuclear interactions. These hadronic showers are generated mostly by the inelastic interactions of hadrons. When these processes occur, they produce a cascade of particles, emitted from particle decay or nuclear excitations. The particles are measured in the active media using gas avalanche multipliers (e.g. our THGEM detectors). The total number of particles created in the shower is proportional to the energy of the incoming primary particle; thus, its energy can be estimated to a good precision by counting the shower particles using appropriate calibration. To accurately count the number of particles in a shower and thus meet the target jet-energy resolution, the sampling elements should have a high detection efficiency and low average pad multiplicity (number of pads triggered per particle).

1.1.2 Active sampling elements for DHCAL

RPC Resistive Plate Counters (RPCs), are the baseline technology for the SiD DHCAL. The RPC, proposed in 1981 [5], is a gas-avalanche detector, with a thin gas volume defined by two parallel resistive plates, typically Bakelite or glass. High voltage is applied between the plates; a charged particle crossing the gas gap initiates a streamer or an avalanche (depending in the applied voltage). This induces signals on the readout strips, or pads located on the outside of the plates, see figure 1.1.3. A report on the progress of RPC sampling elements for DHCAL is given in [6].

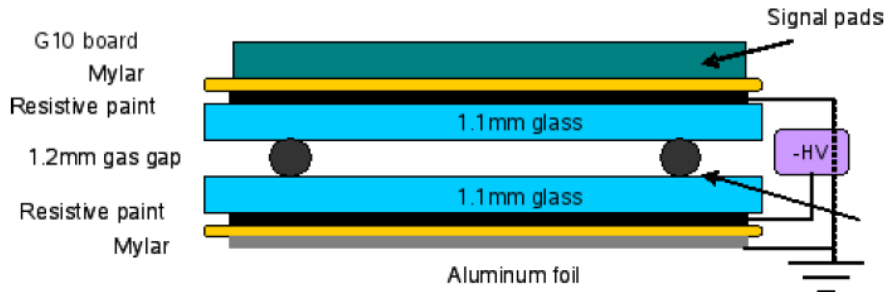


Figure 1.1.3: Schematic of the RPC design with two glass plates. Not to scale. Taken from [2]

MICROMEGAS The MICRO MESH GASEous detector (MICROMEGAS) is a parallel-plate-like detector invented by Giomataris, Charpak et al. in 1995 [7]. It uses a thin metal grid to separate the drift region where the primary electrons are produced from the amplification region (50-100 μm thick) where they are multiplied. The grid has a hole pitch of 20-50 μm and is maintained above the anode plane by means of insulating pillars. High electric Fields (about 40-80 kV/cm) are created in the amplification gap by applying $\sim 400\text{V}$ between the grid and the anode. The operating principle is shown in figure 1.1.4; when an ionizing particle passes through the conversion gap, it creates electron/ion pairs; with an electric field of $\sim 1\text{kV/cm}$ the electrons drift towards the micromesh; they enter the high electric field region in the amplification gap, where they are multiplied by the avalanche effect. The avalanche charges induce a measurable

¹The nuclear interaction length (λ_A) is sometimes written using the approximate formula $\lambda_A \approx 35 \frac{A^{1/3}}{\rho}$ cm [4]

signal; the ions created in the avalanche are rapidly collected on the micromesh, thus providing a high rate capability. Due to the open geometry, avalanche photons may cause secondary avalanches, limiting the gain; thus adequate mixtures with photon quenchers are needed. The progress reached in MICROMEAS-based elements for DHCAL is given in [8].

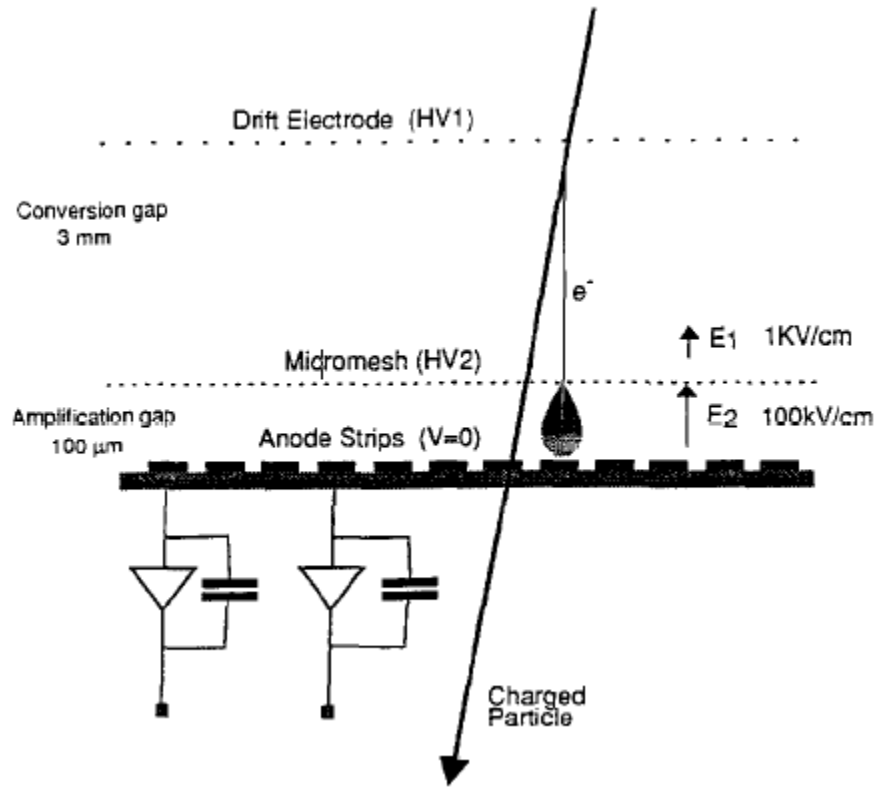


Figure 1.1.4: Schematic view of MICROMEAS: the 3 mm conversion gap and the amplification gap separated by the micromesh and the anode strip electrode. Taken from [7]

The Gas Electron Multiplier (GEM) The GEM, a particularly successful structure, was invented by Fabio Sauli in 1997. The GEM is manufactured by using wet-etching techniques of thin ($\sim 50 \mu\text{m}$) Kapton (polymid) foil, copper-clad on both sides, with holes (typically $75 \mu\text{m}$ in diameter) perforated through at a typical pitch of $140 \mu\text{m}$ (figure 1.1.5). Coupled to a drift electrode above and a readout electrode below, it acts as a highly performing micropattern detector. The main advantages of this detector are high rate capability ($>100 \text{ kHz/mm}^2$ [10]), a closed geometry that decouples multiplication regions from one another, flexible geometry (not necessarily planar) and low mass.

Applying a potential difference between the two copper sides of the GEM (typically 320V to 450 V), a dipole field as high as 100 kV/cm is produced inside the holes (Fig. 1.1.5). These act as independent multiplication channels for ionization electrons focused from the ionization gap above the GEM into the holes. These electrons generate secondary electrons in the high electric field within the holes, resulting in an electron avalanche. The gas amplification depends upon the applied potential across the holes.

In a single-GEM detector, the avalanche leaves the hole and drifts towards the readout plane. Since the GEM gain is limited to $\sim 10^4$, to reach a higher gain one needs to arrange GEMs in a cascade. The avalanche electrons created in the first GEM then drift (with some lateral diffusion) in the transfer gap between the first and second GEMs and then go through second multiplication; This allows the overall maximum gain to be boosted up to 10^6 . Figure

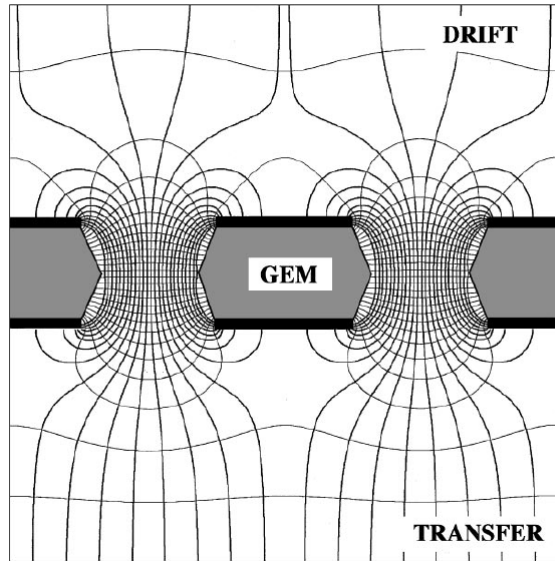


Figure 1.1.5: A schematic drawing of the GEM. Field lines and equi-potentials are shown as well [9]

1.1.6 shows the DHCAL elements with double-GEM sampling elements. Figure 1.1.7 shows a schematic view of a triple-GEM detector, comprising three amplification stages.

Active elements utilizing RPCs, they have yielded so far an average multiplicity of 1.5-2 at 90-95% efficiency [6]. Detection elements based on MICROMEAS, have demonstrated 98% efficiency with a 1.1 average multiplicity [8]. Elements based on double GEMs have shown so far a multiplicity of ~ 1.3 at 95% efficiency [11].

1.1.3 The Thick Gas Electron Multiplier (THGEM)

A relatively new variant of the GEM is the Thick Gas Electron Multiplier (THGEM), suggested in 2004 by the Weizmann Institute (WIS) group² [13]. The THGEM has a hole structure similar to the GEM (figure 1.1.8) but with about 5-20 fold expanded dimensions. The larger thickness (typically 0.4-0.8mm) makes the THGEM a robust structure, which can be easily mounted over large areas, such as needed in the SiD DHCAL. While its spatial resolution is an order of magnitude lower than that of the GEM (0.3-0.7mm [14, 15]), this does not pose a problem for many applications for which the higher GEM resolution is an overkill such as sampling elements for DHCAL.

THGEM's are economically produced in the printed-circuit board (PCB) industry by simple drilling through insulating (e.g. G-10) plates, copper-clad on both sides. Drilling is followed by chemical etching, creating concentric insulating rims around the hole edges (this was found to considerably reduce the discharge probability). The thickness t , hole diameter d , hole distance a , and the rim size h , may be chosen to meet the requirements.

The THGEM's operation principle is basically the same as that of the GEM (figure 1.1.9): a potential difference is applied between the electrodes, creating a strong dipole electric field within the holes. Electrons are generated by incoming ionizing radiation (x-rays or charged particles) in the drift region above the THGEM, or - for UV radiation - by photoelectric absorption in a solid radiation converter (e.g. a CsI photocatode). These electrons drift under

²Similar structures, the Large Electron Multiplier (LEM) [12] and the Modified GEM were suggested by A. Rubia and V. Peskov, respectively. The THGEM differs by the rim incorporated around the holes to prevent discharges.

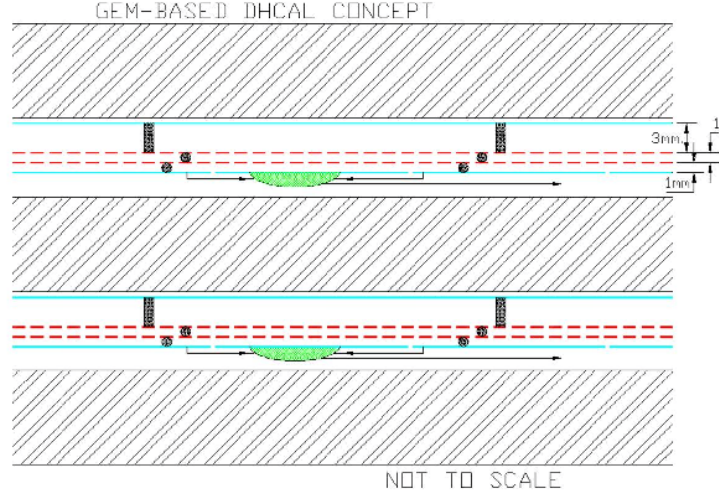


Figure 1.1.6: GEM DHCAL Concept, here with double-DEM elements placed between iron plates [2]

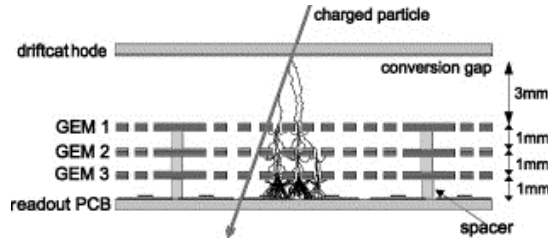


Figure 1.1.7: Schematic view of the detector with three GEM foils .

the influence of the electric field towards the THGEM holes, where they are multiplied in an avalanche process, similar to the GEM but with somewhat lower fields ($\sim 10\text{-}20$ kV/cm).

For electrons generated in the drift gap a drift field of 0.1-1 kV/cm is required, according to the application (in fields lower than ~ 0.1 V/cm electrons and ions would recombine in the gas). The avalanche electrons are either collected by a readout anode following the THGEM, or are transferred to a second amplification stage.

Like GEMs, THGEMs have closed geometry, where each hole acts as an independent multiplier. The avalanche is confined within the holes, so that photon-mediated secondary effects are strongly reduced, leading to high gain operation in a large variety of gases. Unlike "open-geometry" detectors, which require large concentrations of quenchers, for THGEMs the quencher fraction in the gas mixture can be kept low, leading to lower operational voltages at high gains.

The electron collection is more effective than in the GEM because the THGEM's hole-diameter is larger than the electron's transverse diffusion range when approaching the hole [16]. The results of systematic studies of THGEM-based detectors, operating at atmospheric and low gas pressures, have been extensively reported in Refs. [19, 20]. Due to the large hole size, efficient electron transport and reduced photon- and ion-feedback, the THGEM has stable operation in a large variety of gas mixtures, including noble gases. High gains of $>10^4$ and $>10^6$, were reached in single- and double-THGEM detectors, respectively at 1 atm of Ar/CH₄(5%) and Ar/CO₂(30%) [19, 21]. When operating with Ne/CH₄ mixtures, single-photoelectron effective gains in the range of 10^5 and 10^7 are reached with single- and double-THGEM (0.4 mm thick) multipliers [22]. Single-THGEMs with a thickness of 0.8 mm provided single photoelectron effective gains of the order of 10^7 and 10^6 in Ne and Ne/CH₄ mixtures respectively [22].

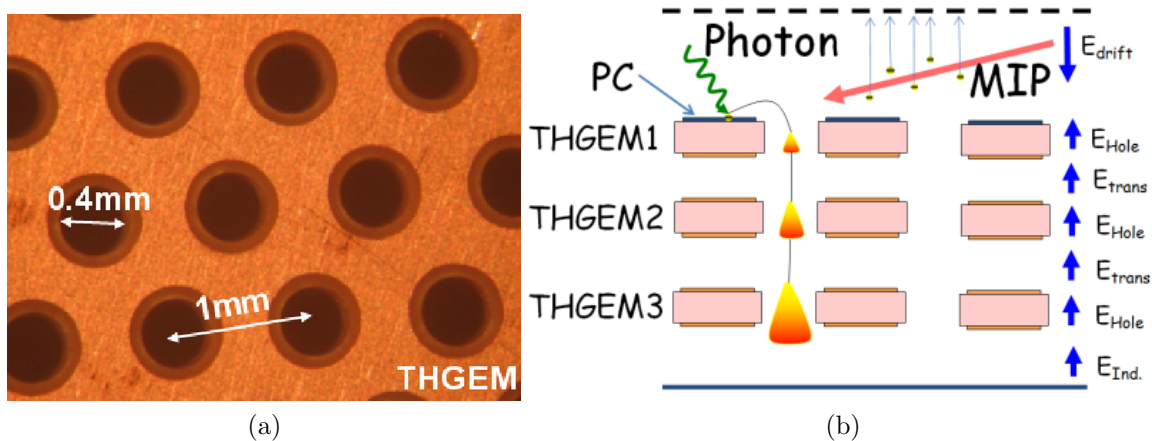


Figure 1.1.8: THGEM: (a) Photograph of typical THGEM electrode: the one shown has a hole-diameter of $d=0.4\text{mm}$ with 0.1mm etched rim, spaced by $a=1\text{mm}$. The thickness is $t=0.5\text{mm}$. Ref. [16]; (b) Scheme of operation principle: UV-photon/MIP detector with 3 cascaded THGEMs and a reflective CsI photocathode on top of the first one Ref. [17].

Compared to argon-based mixtures, neon-based mixtures allow for higher gains for the same THGEM voltage. Effective gain curves of THGEMs are shown in figure 1.1.10.

1.1.4 Motivation and Goals

Space limitations and magnet costs of the ILC-SiD detector dictate a very narrow sampling-element gap, including readout chips, of 8mm . A thin THGEM-based detectors may be attractive as DHCAL sampling element because of its simplicity, thickness and robustness, accompanied by sub-mm spatial resolution, few-ns temporal resolution and up to $1\text{MHz}/\text{mm}^2$ rate capability [16, 22]. The R&D work described in this report was focused on developing sampling elements for the SiD DHCAL; the structures conceived here were evaluated with respect to their ability to meet the requirements of this application – namely: high detection efficiency, low pad multiplicity and small overall thickness, while keeping a low discharge rate and intensity.

We gained considerable experience with THGEM detectors as potential elements for different applications. In the configurations presented above, avalanche electrons induce detectable charges on a segmented readout anode, during their drift towards the anode in an induction (collection) gap. In this work we consider alternative structures, where the readout anode is in contact with the THGEM bottom electrode – closing the THGEM holes (in a WELL configuration). By giving up the induction gap, this configuration allows designing very thin detectors, which may be highly advantageous for DHCAL and other applications as discussed below. The particular field shape of the proposed structure is similar to that of the CAT [23], WELL [24] and closed-geometry GEM [25, 26].

The new configurations studied here aim at reducing the energy and thus the consequences of occasional discharges occurring in gas-avalanche detectors. The latter occur once the total number of radiation-induced avalanche electrons exceeds a certain detector structure-dependent threshold, known as the Raether limit (of typically 10^7 - 10^8 electrons) [27]; when the avalanche charge exceeds this limit a thin plasma filament (streamer) is formed, shortening the cathode and anode (e.g. the top and bottom electrodes in the case of THGEM), causing a discharge ('spark'). Discharges constitute a major limitation, damaging both the electrodes and readout electronics and introducing long dead-times of the detector.

Discharge mechanisms are described in ref. [28]. Discharges that are of particular concerns in

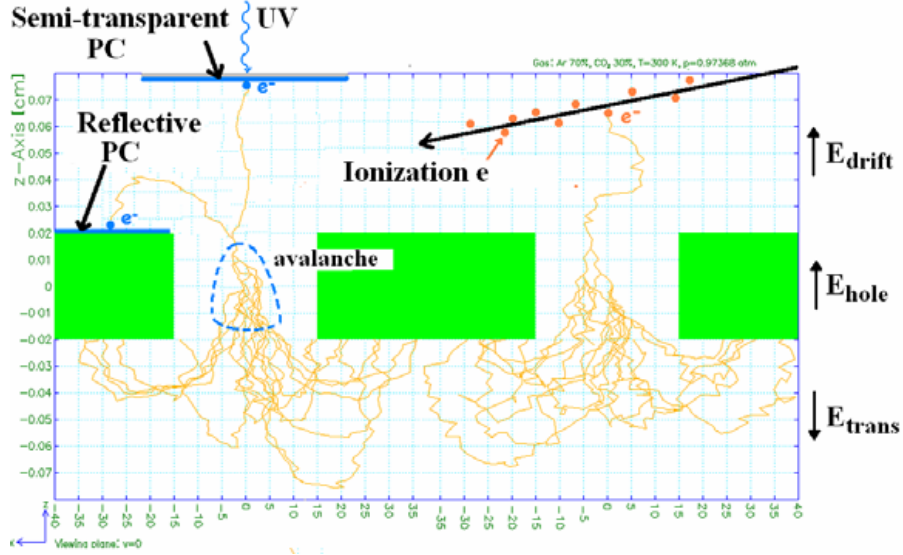


Figure 1.1.9: The operation principle of the THGEM demonstrated by the GARFIELD [18] simulation code at low THGEM gain (~ 30): electrons originating from gas ionization or from a semitransparent or reflective photocathode are focused into the holes, where they undergo avalanche multiplication. Depending on the size and direction of the transfer field E_{trans} , avalanche electrons are further transferred to a readout electrode, to a second multiplier, or are collected at the THGEM bottom electrode as shown here with a reversed E_{trans} . From ref. [19].

applications involving operating a gaseous detector in the presence of highly ionizing radiation background. One particular example is Digital Hadron Calorimetry project, where we aim detecting minimum ionizing particles at the presence of hadronic background – inducing highly ionizing recoils.

Some of the closed-hole THGEM structures investigated in this work, employ a resistive anode to protect the detector against discharges - an idea that has been attracting much attention in the MPGD community lately [29, 30, 31, 5]. The protection is two-fold: first, since the resistive layer is decoupled from the readout pads, the readout electronics is not subject to direct high instantaneous currents during a discharge; second – as in resistive plate chambers (RPCs) [5], the long clearance time of electrons from the bottom of the hole leads to a substantial reduction of the local electric field and blocks the discharge before the entire charge on the detector is depleted.

1.2 Beam tests of THGEM-based sampling elements

1.2.1 Experimental setup and methodology

To assess the potential THGEM sampling element, beam tests were conducted at the CERN SPS/H4 RD51 beam-line, with different THGEM-based detector configurations. The THGEM electrodes used in this work were $10 \times 10 \text{ cm}^2$ in size, manufactured by 0.5 mm diameter hole-drilling in 0.4 mm thick G10 plates, Cu-clad on one or two sides; the holes were arranged in a hexagonal lattice with a pitch of 1 mm; 0.1 mm wide rims were chemically etched around the holes. These parameters were chosen based on previous optimization studies [19]; in view of previous experience with neon mixtures [22, 32], the detectors were operated in Ne/CH₄(5%), where minimally ionizing particles (MIPs) in the relevant energy range deposit on the average

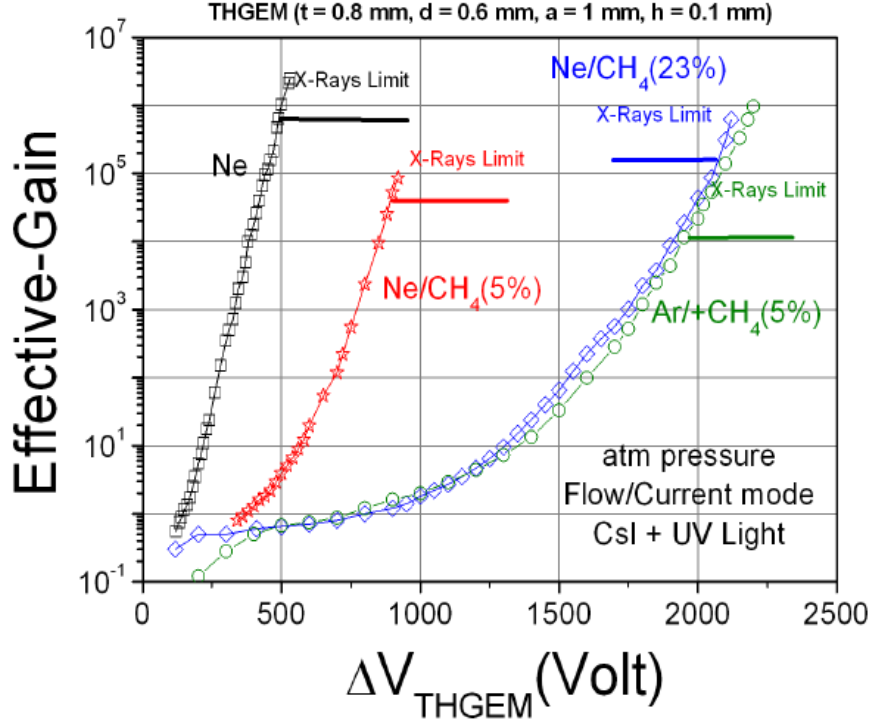


Figure 1.1.10: Single-THGEM effective-gain curves obtained with with single UV photons (CsI photocathode; $E_{drift} = 0$) in Ne, Ne/CH₄ mixtures and in Ar/CH₄(5%). The maximum effective gain reached in each gas, in the same detector, with 8 keV x-rays is also shown ($E_{drift} = 0.2$ kV/cm). THGEM geometry: $t = 0.8$ mm, $d = 0.6$ mm, $a = 1.0$ mm, $h = 0.1$ mm. From ref. [22].

a total number of ~ 60 electrons per cm along their track [33]. The experiments were performed with 150 GeV/c muons and pions.

The main detector configurations investigated comprised either a single-THGEM, (with a drift gap of 3-4 mm and an induction gap of 2 mm), or a double-THGEM (with a 3 or 10 mm drift gap, 2 mm transfer gap and 2 mm induction gap) (fig. 1.2.1). Single-THGEM operation at beam conditions was done at a gain of $1 - 2 \times 10^3$; the double-THGEM detector was operated at a total gain of $4 - 8 \times 10^3$. The respective voltage settings are provided in the results section.

The detector was operated with an external trigger, provided by the RD51 GEM/MICROMEGAS tracker telescope setup [34, 35] with its three 10×10 cm² scintillators in coincidence. The HV power supply was remotely controlled with the CAEN SY2527 controller, using A1833P and A1821N boards. The voltage and current on each channel were monitored using dedicated RD51 slow control system [36]. All inputs were connected through RC filters (a 15 M Ω resistor + 1 nF capacitor).

The core of the beam studies was performed using an array of 8×8 1 cm² Cu pads, coupled to KPix readout electronics [37]. KPix is a multi-channel system-on-chip, for self-triggered detection and processing of low-level charge signals, whose development was motivated by the SiD for the ILC. Because the intended application is for a pulsed accelerator (ILC), data acquisition proceeds for a period of up to 3 ms, followed by readout of digital data. This resulted in a limited electronics readout efficiency of $\sim 3\%$ for the test run. The version of KPix used in these tests contained 512 channels, of which only 64 were wire-bonded to the 8×8 array of pads.

Studying the possible damping of occasional spurious discharges, a preliminary experiment

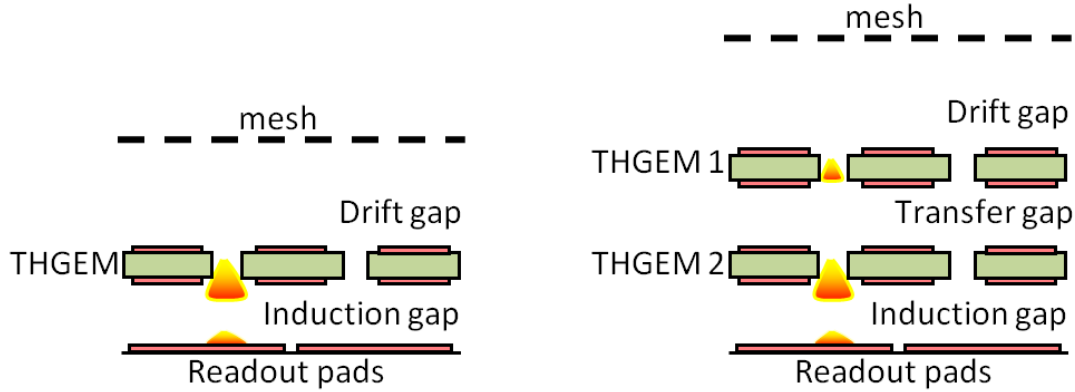


Figure 1.2.1: Single- and double-THGEM configurations. The metal readout pads collect the direct avalanche charge.

was also done in beam conditions with a resistive anode in contact with the THGEM, in a configuration named Resistive WELL, or RWELL for short – this configuration (see Fig. 1.4.1) is fully described in section 1.4 below.

All experiments described in this section were performed with Ne/CH₄(5%).

1.2.2 Beam test results

Prior to our recent investigations with KPix readout, the 10×10 cm² detector properties in different configurations were studied with discrete electronics.

Figure 1.2.2(A) shows an example of the pulse-height distribution recorded with muons in a narrow single-THGEM configuration (3 mm drift gap, 2 mm induction gap). Here, the charge signals from the central four 1 cm² pads interconnected were recorded with a single charge sensitive preamplifier/linear-amplifier/MCA. Data acquisition was triggered by the three telescope scintillators, in coincidence with a 0.5×1 cm² scintillator positioned in front of the detector’s center. The detector was operated at a gain of $\sim 1.1 \times 10^3$, with negligible discharge probability (of the order of 10^{-6} or lower). The detection efficiency (recorded events per number of triggers) as a function of THGEM voltage is shown in figure 1.2.2(B). Note that in this configuration, the total width of the detector was 5.5 mm.

Initial investigations with KPix were done with double-THGEM configurations, which allowed operation at relatively high gains with low discharge rates. Figure 1.2.3 shows examples of Landau distributions recorded with KPix in double-THGEM structures, with a broad muon beam covering the entire detector area and with a narrow pion beam of a few mm in diameter impinging on the central area. The respective local rates for muons and pions were a few Hz/cm² and a few kHz/cm². The detector was investigated with drift gaps of 3 and 10 mm; in both cases the transfer and induction gaps were 2 mm wide. The applied voltages were asymmetric, with 610 V across the first THGEM and 510 V on the second. The drift-field was 650 V/cm for the 10 mm drift gap and 200 V/cm for the 3 mm one. In this configuration and voltages, the effective gain was in the range $4\text{--}8 \times 10^3$. The pulse-height distributions were obtained by recording, for each trigger, the sum of charge over the pad which displayed the highest signal and its 4 neighbors. The data shown in fig. 1.2.3 is preliminary, in the sense that it contains empty-trigger events with particles passing outside of the detector’s active area. In this case, KPix simply stored the amplitude of the noisiest channel, shown as the noise peak in the lowest charge bins. In principle, this effect can be mitigated by discarding events whose locations in the tracker fall outside of the region overlapping the detector’s active area. This

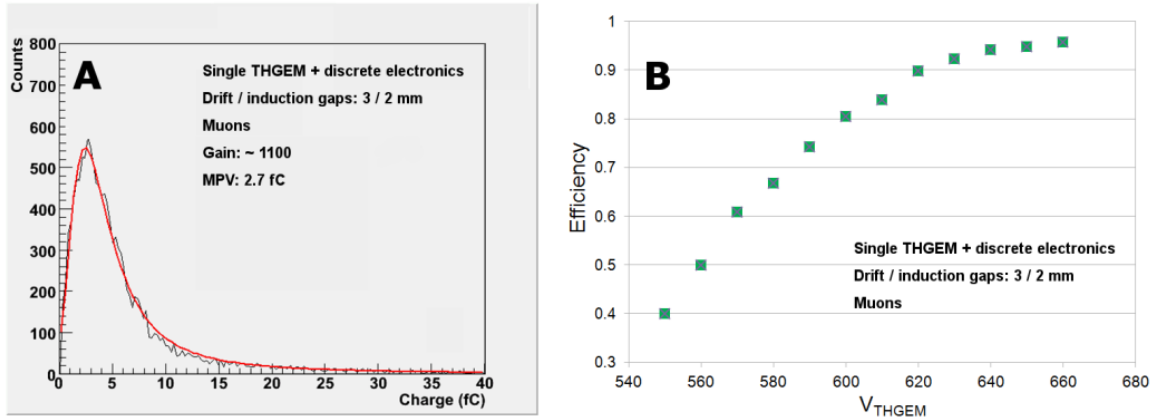


Figure 1.2.2: (A) Charge distribution of muons recorded with a $10 \times 10 \text{ cm}^2$ single-THGEM detector (3 mm drift and 2 mm induction gaps) using a charge sensitive preamplifier connected to 4 pads. $\text{Ne}/\text{CH}_4(5\%)$; gain 1.1×10^3 . The line matching the distribution is a Landau fit to the data. (B) Muon detection efficiency vs. THGEM voltage for the same configuration.

line of analysis is still in process.

All of the double-THGEM configurations displayed low discharge rates, with probabilities $< 2 \times 10^{-6}$ sparks/event - for both muons and pions (for both 3 and 10 mm drift gaps), as averaged over 7-8 hours of operation in beam per given configuration. Since in some runs there were no discharges, this value can be considered as an upper limit on the actual discharge probability for the double-THGEM structures in these operation conditions.

Further investigations were performed with a single-THGEM configuration of a 4 mm drift gap and 2 mm induction gap. To resolve the most probable value (MPV) from the empty-trigger noise, the detector was operated at a gain of $\sim 1 \times 10^3$, resulting in higher discharge probabilities: $\sim 1 \times 10^{-5}$ for muons and $\sim 1 \times 10^{-4}$ for pions. Figure 1.2.4 shows the Landau spectrum obtained in this configuration for a broad muon beam and a narrow pion beam. In both cases the THGEM voltage was 700V, the drift field was 325 V/cm and the induction field 1 kV/cm. KPiX triggers following a discharge were removed from the analysis. The empty-trigger noise was removed in this case by placing a cut at 1.5 fC and the Landau fit was forced to go through zero, yielding an MPV of 9 fC for both muons and pions.

The average pad multiplicity (average number of pixels triggered per event) was estimated for the single-THGEM runs, by counting the number of neighboring pixels with a signal above 1 fC for all events where the maximum signal (main hit) was above 1.5 fC. Multiple-pixel hits during sparks were removed from the analysis. The resulting average pad multiplicity was 1.14 ± 0.03 for muons and 1.18 ± 0.02 for pions.

Efficiency measurements with KPiX in external trigger mode require either event matching between the detector and tracker. However, since it has already been demonstrated that a single-THGEM with a 3 mm drift gap can reach 96% efficiency (fig. 1.2.2), it can be safely estimated that a similar level of efficiency can be obtained for a single-THGEM detector coupled to KPiX with the empty triggers removed, since the typical KPiX noise is $\sim 0.3 \text{ fC}$. One should recognize, however, that multiplicity and efficiency are coupled through the threshold, and hence setting a low threshold to obtain a high efficiency may lead to higher multiplicity values. To get the multiplicity level mentioned above (1.1-1.2), the threshold should be set to $\sim 1-1.5 \text{ fC}$. By calculating the area below the Landau distribution function, one can show that this would require the MPV to be at $\sim 3-5 \text{ fC}$ (detector gain of $\sim 1-2 \times 10^3$) to keep the efficiency at $\sim 95\%$ or higher.

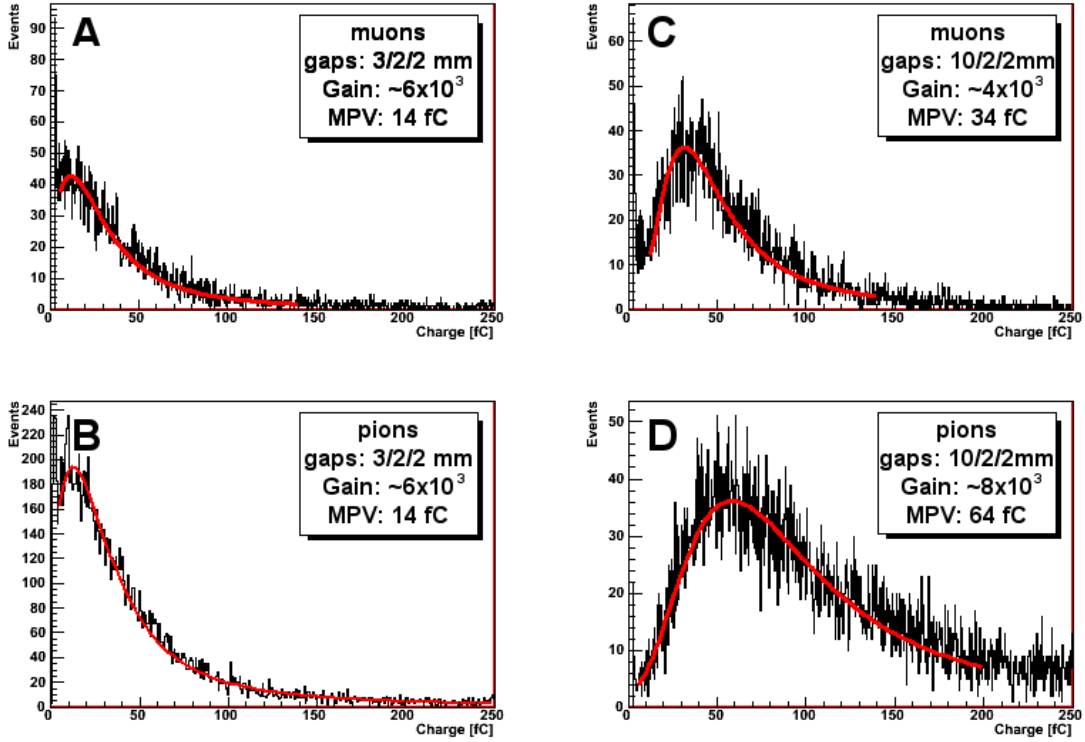


Figure 1.2.3: Landau distributions of muons and pions, recorded with KP*i*X, in two double-THGEM configurations with 3 mm (A,B) and 10 mm (C,D) drift-gap. Detector effective gains and most probable values (MPVs) are indicated in the figures. The muon rates (broad beam) were of a few Hz/cm²; that of the pions (narrow beam) were a few kHz/cm². (See text for more details).

A preliminary test was also done with the RWELL configuration in beam conditions. Figure 1.2.5 shows the Landau distribution obtained with an RWELL (see configuration in Fig. 1.4.1), with the discrete readout electronics. Unlike the regular single-THGEM structure, the WELL with resistive anode allowed raising the gain to $\sim 4 \times 10^3$ (THGEM voltage of 710 V) with no evidence of discharges under a muon beam (discharge probability $< 2 \times 10^{-6}$).

1.2.3 Conclusions

In the beam test, we showed that THGEM-based detectors could comply with the DHCAL requirements - a low pad multiplicity (1.1-1.2) with a high efficiency ($>95\%$). However the thickness and robustness of the active elements play a major role in the choice of the appropriate detector. Decreasing the active gap size, i.e. making thinnest possible efficient detector, would significantly lower the cost of a whole SiD detector mainly dictated by that of the superconductive magnet. This motivated further studies described in the following sections.

1.3 The Thick-WELL (THWELL)

1.3.1 Structure and motivation

In this section we describe the properties of the Thick-WELL structure (THWELL for short), the simplest structure studied in this work. The THWELL comprises a standard THGEM

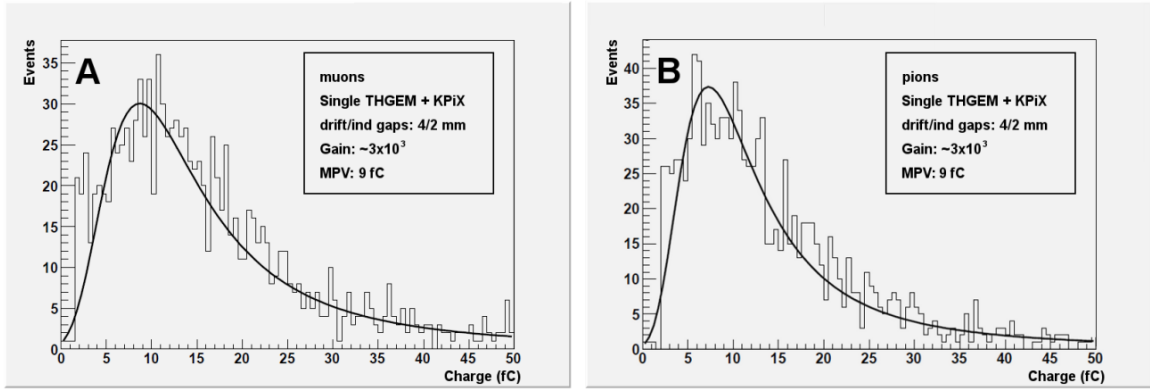


Figure 1.2.4: Landau distributions recorded with KPix, in a single-THGEM configuration with a 4 mm drift gap and 2 mm induction gap: (A) broad muon beam; (B) narrow pion beam. Empty triggers were removed by setting a cut at 1.5 fC. Discharge probabilities were $\sim 1 \times 10^{-5}$ for muons and $\sim 1 \times 10^{-4}$ for pions at detector gain of 3×10^3 . (See text for more details).

with a copper layer on its top side only (single-faced THGEM), whose bottom side is in direct contact with a readout anode, as shown in figure 1.3.1.

The basic motivation for this structure is the reduction of the total thickness of the detector due to the absence of the induction gap. However, as will be shown below, this structure has additional benefits, namely a higher gain for a given voltage (compared to the regular THGEM structure with an induction gap) and a lower discharge rate for the same gain.

1.3.2 Gain

Experimental setup Gain measurements, as well as all other measurements in this section, were performed using 3×3 cm² THGEM electrodes. Their parameters were: thickness $t = 0.4$ mm, hole spacing $a = 1$ mm, hole diameter $d = 0.5$ mm and rim size $h = 0.1$ mm (i.e., rim diameter 0.7 mm). The electrodes were prepared by drilling a hexagonal hole pattern in copper-clad G-10 plates (either single or double-faced), followed by etching to create the rims. All electrodes were first tested in air, by applying 1.5 kV across their two sides and measuring the leak current (typically of the order of 0.1 nA). For the single-faced electrodes, this was performed by placing the THGEM bottom in contact with a conductive base and applying the voltage between the THGEM top and the base.

The THGEM was mounted inside a 10 cm diameter aluminum vessel with 200 micron thick Mylar window (see fig. 1.3.2).

The drift mesh used comprised 50 micron thick stainless steel 304 wires arranged in a square pattern with 0.5 mm spacing. The detector was operated with Ne/CH₄(5%) at 1 atm flushing at a typical flow of 40 sccm. A two-stage oil bubbler was used at the outlet of the chamber.

The detector was irradiated using an x-ray generator (XTF5011 - Oxford Instruments) having a Cu anode, operated at 20 kV, producing 8-keV x-rays on top a Bremsstrahlung background. A second Cu foil was used as a filter to attenuate the Bremsstrahlung component. The beam was collimated using a 0.5 mm aperture at the end of a 20 cm long tube. Figure 1.3.3 shows a comparison between the spectra measured with and w/o the second Cu foil, with the THWELL detector operated in the above conditions, using the amplification chain and multichannel analyzer described below.

The detector electrodes were biased using one or more CAEN N471A power supply units, through low pass filters ($R=20M\Omega$ $C=10nF$). The DC current from the detector anode was measured using a Keithley 610CR electrometer as a function of the applied high voltage. The

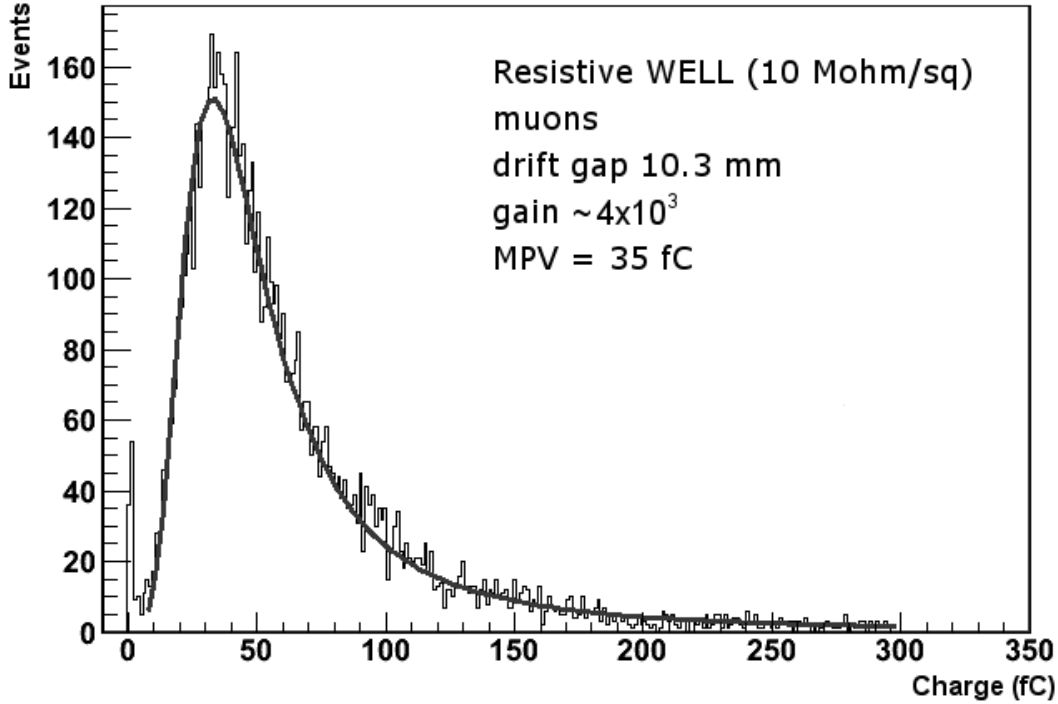


Figure 1.2.5: Landau distribution recorded with the RWELL configuration. THGEM voltage was 710 V. No discharges were observed during the measurement (discharge probability $< 2 \times 10^{-6}$).

electrometer was connected to the anode through a 20 M Ω resistor. The x-ray flux was set such that the current drawn from the detector was smaller than 10 nA to limit the voltage drop on the resistor ($\Delta V = IR < 10 \cdot 10^{-9} \times 2 \cdot 10^6 = 10mV$) and thus not affect the voltage difference across the THWELL or induction gap.

Gain measurements consisted of two complimentary steps. The first step comprised measuring the anode current as a function of the voltage across the THGEM for a fixed x-ray flux, keeping the drift field fixed at 0.5 kV/cm (for the induction gap configuration, the induction field was kept constant at 0.5kV/cm or 1.0 kV/cm). This allowed scanning the entire range of THGEM voltages (e.g., 0-750 V). The second step comprised measuring the effective gain in pulse mode for a high THGEM voltage (typically 700-750 V) with a calibrated amplification chain. This was done in order to normalize the full gain curve measured in the DC current mode. Pulses were measured with a charge sensitive preamplifier (ORTEC 124), followed by shaping amplifier (ORTEC 572A) and further recorded by a multi-channel analyzer (MCA, Amptek MCA8000A). A protection circuit comprising two diodes connected back to back in parallel with a 10k Ω resistor was used between the anode and preamplifier. The amplification chain was calibrated using a 10 pF capacitor, applying a square wave voltage signal from a pulse generator, to inject a known charge to the preamplifier and record the MCA response (i.e., give the relation between MCA channel and injected charge).

The effective gain was calculated in the pulse-mode measurements by dividing the centroid value of the Gaussian-like peak recorded on the MCA by the primary charge (the total charge deposited in the gas following the absorption of an x-ray photon):

$$G = Q_{MCA}/Q_p \quad (1.3.1)$$

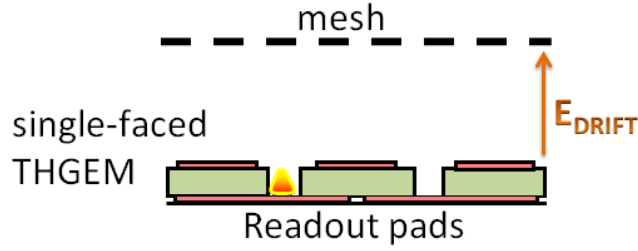


Figure 1.3.1: Schematic drawing of the THWELL structure (including the THGEM and drift electrode). The THGEM bottom is in direct contact with the anode.

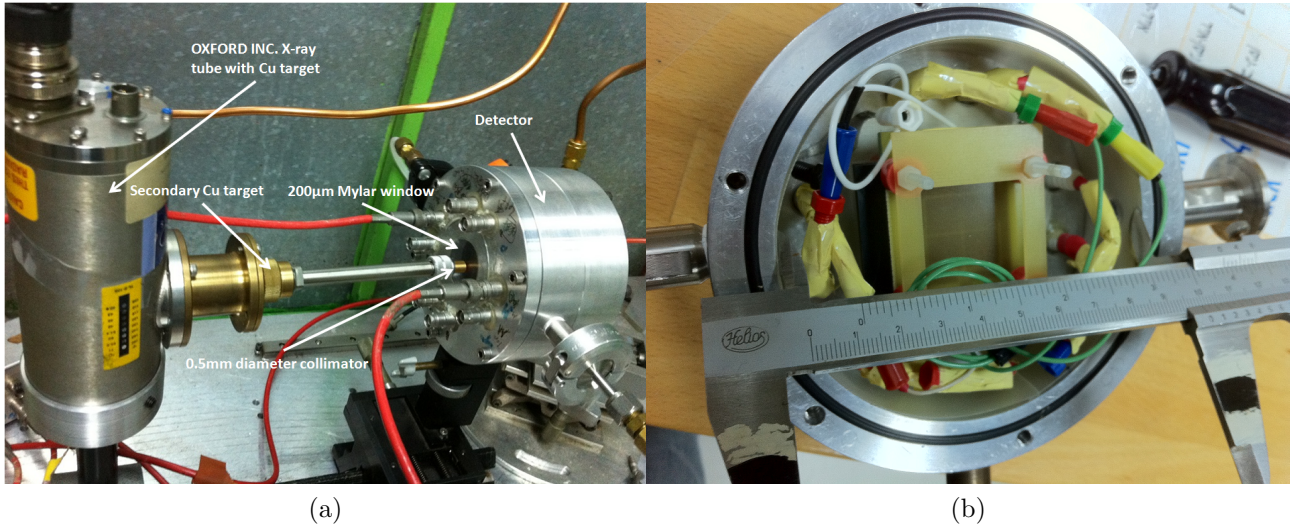


Figure 1.3.2: Experimental setup: (a) side view of the chamber, x-ray generator, Cu targets and collimator; (b) inside view of the detector.

where:

$$Q_p = q_e n_p = q_e \frac{E_{x-ray}}{W} \quad (1.3.2)$$

Here $q_e = 1.6 \cdot 10^{-19}$ is electron charge, n_p is the number of primary electrons, E_{x-ray} is the x-ray energy and W is the average energy required to produce a single electron-ion pair for the gas mixture (' W value'). For 8 keV electrons and Ne/CH₄(5%) with $W = 35.6eV$ [33], $Q_p \approx 0.036fC$.

Results Figure 1.3.4 shows the gain curves measured for the THWELL and induction-gap configurations, for an induction gap of 2.3 mm and induction fields of 0.5 and 1.0 kV/cm. The curves end at a THGEM voltage where the spark rate was of the order of a several sparks per minute.

Note that even for the higher induction field ($E_{ind}=1kV/cm$), the THWELL reaches a higher gain compared to the induction gap configuration at the same voltage.

Analysis The different properties (gain, in particular) of the THWELL and induction-gap configurations stem from the different shapes of the corresponding electric fields. The fields of both structures were calculated using MAXWELL3D v11 [38] and are shown in figure 1.3.5. The plot depicts the field strength along the central axis of the structure (z -axis). While the maximum of the field strength in the induction-gap configuration is at the center of the hole,

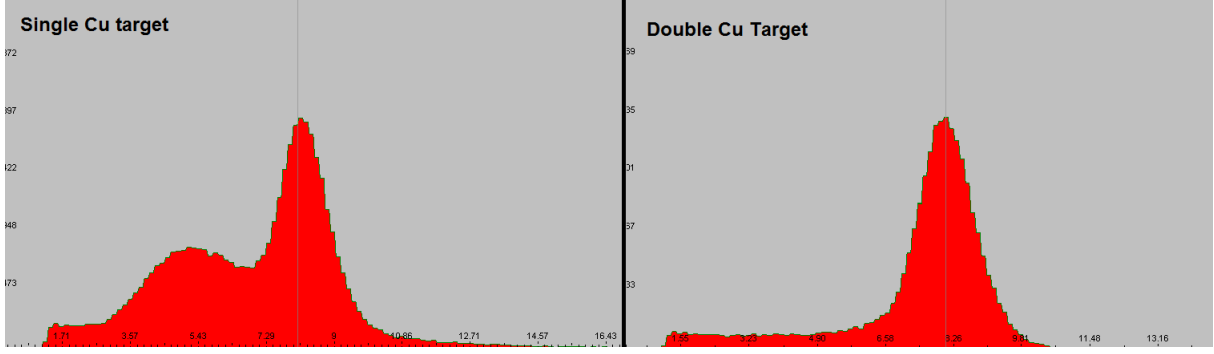


Figure 1.3.3: X-ray tube spectra measured with the THWELL detector with and w/o Cu filter

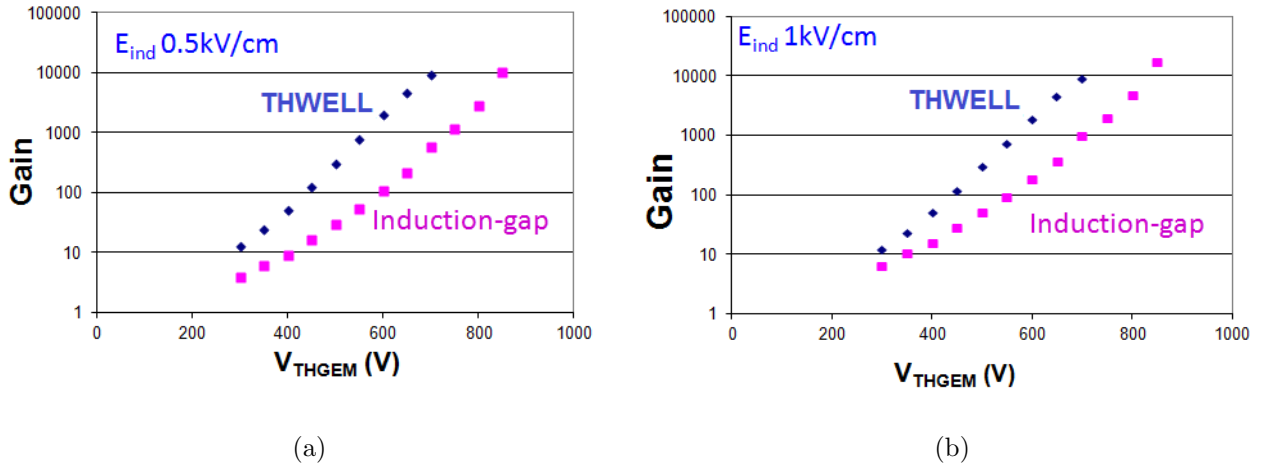


Figure 1.3.4: Gain curves for the THWELL and induction-gap configuration, measured with 8 keV x-rays. The induction gap was 2.3mm, and the induction field was either 0.5 or 1kV/cm. The detector parameters were $t=0.4$, $d=0.5$, $a=1.0$ and $h=0.1$ mm. Gas: Ne/CH₄(5%), flow mode. The drift gap was 1cm with 0.5 kV/cm drift field

the field continuously increases towards the anode in the THWELL. Thus, in the THWELL the last generations of the multiplication avalanche are subject to a higher field than in the induction-gap structure. This results, as was shown in figure 1.3.4, in a higher gain for a given THGEM voltage in the THWELL configuration.

The higher field in the THWELL compared to the induction gap configuration is expected to produce a higher gain for same voltage. A rough theoretical estimate for this effect can be made as follows. The multiplication factor for an avalanche developing along the z axis between two points is given by (eq. 24 in [33]):

$$Gain = \exp \left[\int \alpha(z) dz \right] \quad (1.3.3)$$

where $\alpha(z)$ is the first Townsend coefficient defined as the inverse mean free path for ionization (λ):

$$\alpha = \frac{1}{\lambda} \quad (1.3.4)$$

The first Townsend coefficient is a transport parameter used to describe the charge growth in a detector operating in avalanche mode. This coefficient represents the number of electrons created per unit of length by a primary electron, along the electric field direction and depends

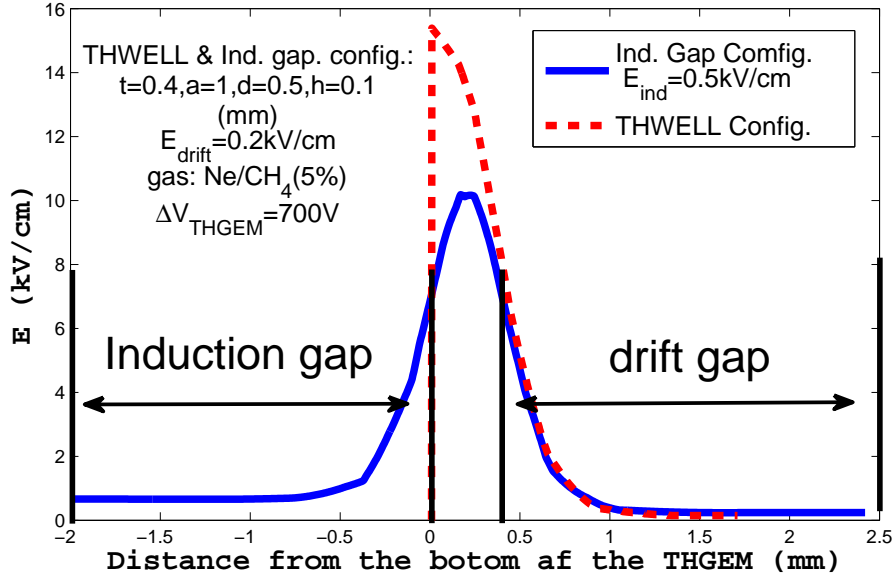


Figure 1.3.5: Comparison of the electric field inside the THGEM holes along the central axis in the induction-gap and THWELL configurations, as calculated using MAXWELL3D.

on the gas composition and on the strength of the electric field. For a uniform electric field (e.g. in parallel plate detectors), the multiplication is given by:

$$n(z) = n_0 e^{\alpha(E)d} \quad (1.3.5)$$

where d is the width of the detector.

Townsend coefficient for Ne/CH₄(5%) mixture vs. the electric field strength are shown in fig. 1.3.6.

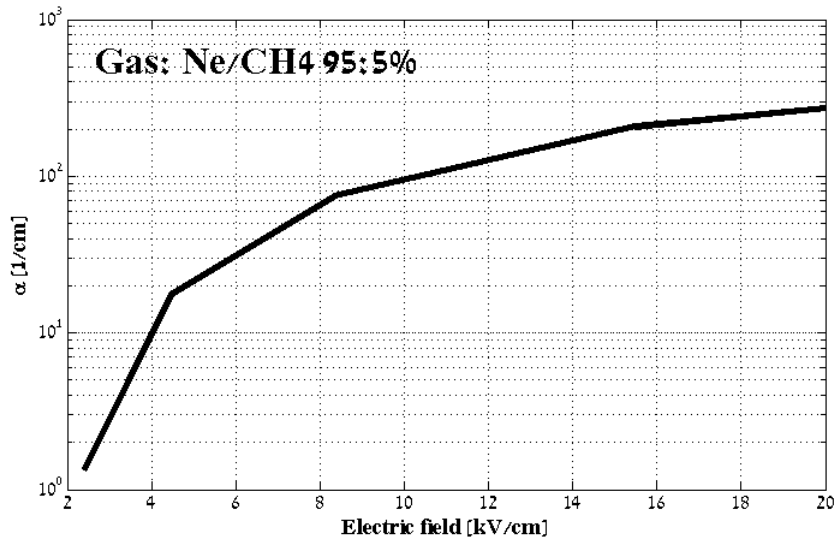


Figure 1.3.6: Townsend coefficient calculated using Magboltz 7 [39] for Neon/CH₄ 95:5% gas mixture

Using field strength calculated for THWELL and induction gap configurations (Figure 1.3.5), and the first Townsend coefficient (Figure 1.3.6) we can compare multiplication for both configurations. The numerical calculation for $t = 0.4$ mm, induction gap of 2mm and

$\Delta V_{THGEM} = 700$ gives factor ≈ 8 in the measured gain. The simulated gain from equation 1.3.3 differs from the effective gain of the detector, shown in figure 1.3.4 where measured gain ratio was ≈ 10 . The effective gain is a the product of the collection efficiency of primary electrons, the multiplication factor inside the hole and the fraction of avalanche electrons reaching the anode (when the signal is read inductively behind a resistive layer, the effective gain also includes the transparency to the induced charge of the resistive layer). The first Townsend coefficient obtained from Magboltz [39] simulation also does not include possible Penning transfers³. Note, however, that in the structures studied in this section the collection efficiency is essentially 1 and for an induction field of 1 kV/cm the fraction of avalanche electrons reaching the anode is $>85\%$.

1.3.3 Pulse shape

The THWELL differs from the induction gap configuration not only in its field distribution and gain, but also in the pulse shape measured on the anode. The pulse shape is governed by the current induced on the anode by the moving charges of the avalanche both electrons and ions. The induced current on the anode for a moving point charge is given by the Ramo's theorem [40]:

$$i(t) = q\mathbf{E}_w \cdot \mathbf{v} \quad (1.3.6)$$

where q is the charge, \mathbf{v} is the velocity and \mathbf{E}_w is the 'weighting field', calculated by applying unit potential to the selected electrode (here, the anode), with all other electrodes at zero potential and all charges removed. When there are both electrons and ions present with some arbitrary charge density distributions $\rho_{el}(r, t)$ and $\rho_{ion}(r, t)$, the induced current is given by:

$$i(t) = \int \rho_{el}(\mathbf{r}, t)\mathbf{E}_w(\mathbf{r}) \cdot \mathbf{v}_{el}(\mathbf{r})d\mathbf{r} + \int \rho_{ion}(\mathbf{r}, t)\mathbf{E}_w(\mathbf{r}) \cdot \mathbf{v}_{ion}(\mathbf{r})d\mathbf{r} \quad (1.3.7)$$

where the drift velocities depend on the position through the field. In the THWELL configuration the contribution of the ions to the induced signal on the anode is much larger than in the induction gap configuration, primarily because the ions are moving in a region with a 15-fold larger weighting field, as shown in figure 1.3.7.

(Note that the ion drift velocity is also somewhat larger in the THWELL hole, particularly near its bottom). The larger ion contribution is shown experimentally in figure 1.3.8, which compares the preamplifier (ORTEC 124) pulse shapes measured on the anode for the two configurations.

The main difference between the pulse shapes is that the signal peak in the THWELL configuration is delayed by $\sim 0.6\mu\text{sec}$ compared to the induction gap configuration. The delay of the peak is of the order of the ion drift time inside the hole. The ion drift time can be roughly estimated using the mobility of Ne ions in the Ne-CH4 mixture. The mobility μ is defined in [41] as the proportionality factor between the ion's drift velocity v_D in a gas and the electric field strength E divided by the pressure p :

$$\mu := \frac{v_D}{E/p} \left[\frac{\text{cm}^2}{\text{V}\cdot\text{sec}} \cdot \text{Torr} \right] \quad (1.3.8)$$

The mobility of neon ions in pure neon at 1 atm is $4.1 \frac{\text{cm}^2}{\text{V}\cdot\text{sec}}$ [42], the mobility of CH4 ions in pure CH4 at 1 atm is $2.26 \frac{\text{cm}^2}{\text{V}\cdot\text{sec}}$ [33]. For a given (constant) mobility, the drift time of Ne ions

³Penning effect – when the excited noble gas (e.g. neon with excited state above 16eV) can ionize quencher (e.g. CH4 with ionization potential of 12.65eV)

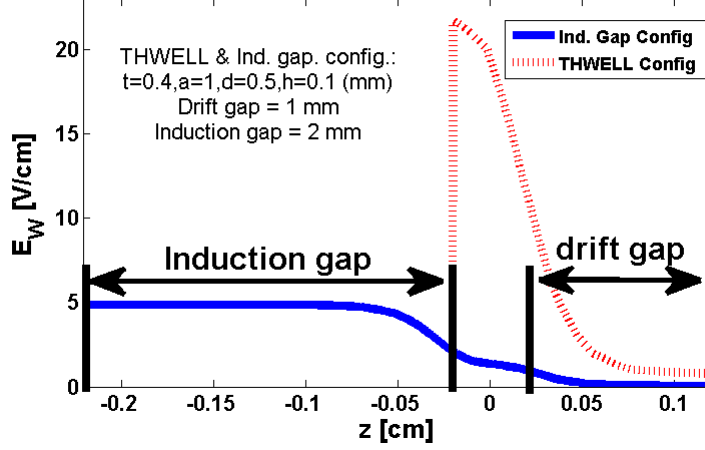


Figure 1.3.7: The weighting field (E_w) in the THWELL and induction-gap configurations (induction gap of 2mm). The weighting field at the center of the hole is 15 fold larger in the THWELL (calculated using MAXWELL3D [38]).

created at height a above the anode through the hole is given by:

$$\tau = \frac{1}{\mu} \int_a^t \frac{dx}{E(x)} \quad (1.3.9)$$

A plot of the ions drift time to the top THGEM face, vs z ionization point ($z=-0.2$ is the anode) is shown in figure 1.3.9. The drift time of the ions in the hole is approximately estimated to be:

$$\langle \tau_{DRIFT} \rangle = \frac{\int \tau(z) \frac{dM(z')}{dz'} \Big|_{z'=z} dz}{\int e^{\alpha(z)} dz} = 0.7 \mu\text{sec} \quad (1.3.10)$$

where $M(z)$ is the multiplication (or a gain - eq. 1.3.3) factor for electron arriving from the top (t) to z , and given by:

$$M(z) = \exp \left[\int_z^t \alpha(z') dz' \right] \quad (1.3.11)$$

The calculations are consistent with the measured time in figure 1.3.8.

1.3.4 Study of discharges in the THWELL and induction-gap configurations

A direct discharge to the readout anode may cause irreversible damage to the electronics. Thus a potential disadvantage of the THWELL is that, unlike the case where an induction gap separates the THGEM from the readout plane (with discharge current shared between electrodes), all of the charge released during a spark reaches the anode. In order to gain quantitative understanding of this phenomenon, the rate and magnitude of discharges in the THWELL configuration were studied and compared to the induction-gap case. As part of the study, the partition of charge between the THGEM bottom and anode in the induction-gap configuration was also investigated. Discharges were recorded by reading the current provided by the CAEN N471A power supply (PS), following a spark using the I_{MON} terminal. The I_{MON} signal was recorded using a National Instruments data acquisition card (NI USB-6008). Figure 1.3.10 shows an example of such a current pulse.

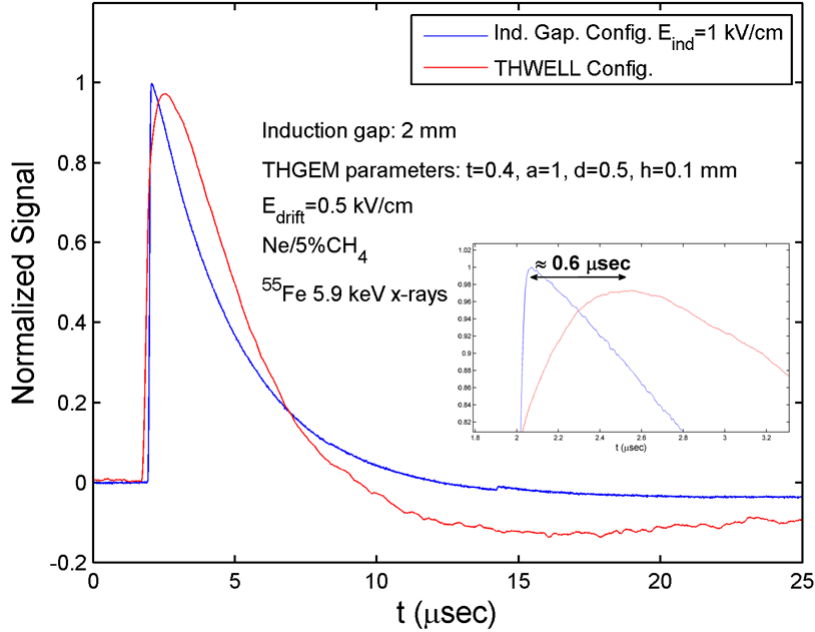


Figure 1.3.8: Signal shapes from the THWELL and induction-gap configurations measured with a charge sensitive preamplifier.

Note that the relatively long timescale (~ 1 sec) of these pulses reflects the response of the power supply to the discharge, rather than the dynamics of the spark itself. The detector was irradiated using the OXFORD x - ray tube with double Cu targets. Operating in the proportional mode a constant current was measured from the I_{MON} terminal. The constant current is given by:

$$I_0 = n_p \cdot G \cdot f \cdot q_e \quad (1.3.12)$$

where n_p is the number of primary electrons, G is the effective gain of the detector and f is the rate of x-ray absorption in the drift gap.

Once a discharge between two electrodes occurs, the electrodes are discharged and charged back by the PS to reach their set voltage. The total amount of the charge in the spark can be calculated by integrating over this current, subtracting the constant current measured in proportional mode:

$$Q_{spark} = \int_{t_1}^{t_2} (I(t) - I_0) dt \quad (1.3.13)$$

Note that the total charge is composed of the charge stored on the THGEM itself, and on the coaxial cable connecting the power supply and the detector electrode (which acts here as a cylindrical capacitor). The cables have a capacitance of 50-100 pF/m. Most of the length of the cable was decoupled from the detector with a 20M Ω resistor, but still a short segment (of ~ 50 cm) was connected to the detector adding parasite capacitance to the system. Figure 1.3.11 shows the discharge probability (number of discharges divided by number of x-ray absorption events) for the THWELL and induction gap configuration, as a function of the detector effective gain. The induction gap was 2.3mm and the induction field 0.5kV/cm.

The measurements were carried out over 20-30 hours. As is evident in the figure, the discharge probability at a given gain is significantly lower for the THWELL configuration. The typical number of discharges measured at a given voltage was 4-10 spark per hour. When a discharge occurs in the THWELL, all of the charge goes to the anode. With a total capacitance of ~ 150 pF (THGEM + cable), this gives ~ 100 nC at a THGEM voltage of 700 V. For the

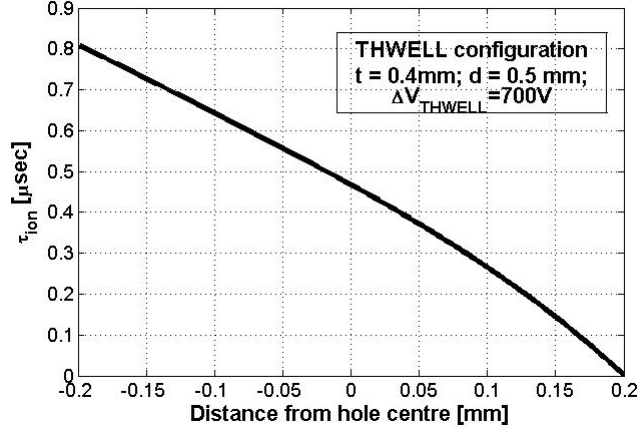


Figure 1.3.9: Ion drift time vs ionization point (z)

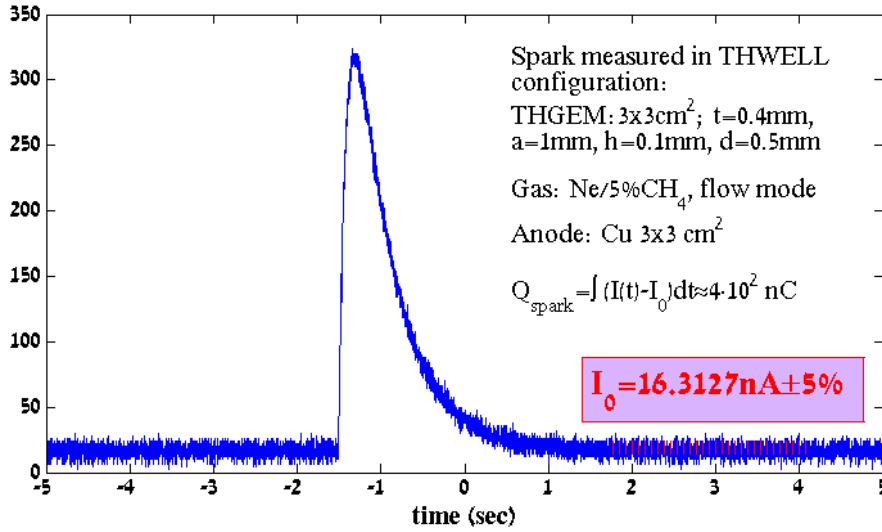


Figure 1.3.10: Current pulse from I_{MON} of the power supply during a spark, recorded from the top of the THGEM electrode.

induction gap configuration, however, only part of the spark charge reaches the anode, with the remaining charge ending on the THGEM bottom.

The fraction of spark charge reaching the anode for the induction gap case was calculated by measuring the spark charge on the anode Q_A and on THGEM bottom Q_B using the I_{MON} terminal on the respective high voltage channels:

$$f_{anode}(spark) = \frac{Q_A}{Q_A + Q_B} \quad (1.3.14)$$

This was compared to the fraction of the signal reaching the anode in proportional mode:

$$f_{anode}(signal) = \frac{I_A^0}{I_A^0 + I_B^0} \quad (1.3.15)$$

where I_A^0 and I_B^0 are the DC currents measured on the anode and THGEM bottom respectively in proportional mode.

Table 1.1 summarizes the measurements of the discharge magnitude (spark charge) and fraction of spark and signal charge reaching the anode for varying values of the induction field (for an induction gap of 2.3 mm), in comparison to the THWELL. Interestingly, for a an

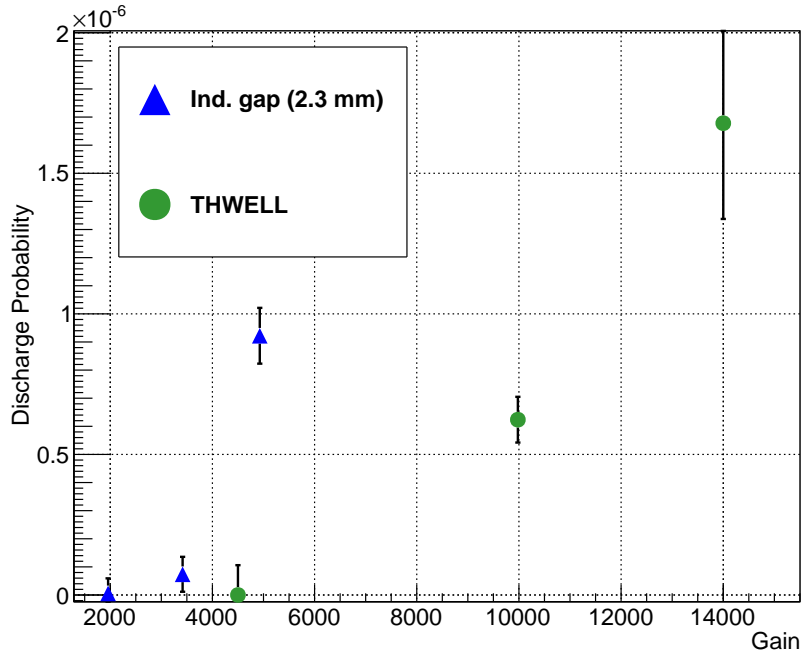


Figure 1.3.11: Discharge probability vs gain for the THWELL and regular THGEM with 2.3 mm induction gap. The measurements were done with 0.5mm diameter collimated 8 keV x-ray beam, at flux of 10kHz/mm²

induction field of 1 kV/cm, only 1% of the spark charge reaches the anode, while, in the same conditions the anode collects >85% of the charge of a normal signal.

Configuration	Spark Charge (nC)	Fraction of spark on the anode	Fraction of signal on the anode
THWELL	$1.5 \cdot 10^2$	100%	100%
Ind. gap 0.5kV/cm	$2.0 \cdot 10^2$	< 1%	Not measured
Ind. gap 1kV/cm	$2.0 \cdot 10^2$	< 1%	>85%
Ind. gap 1.5kV/cm	$2.0 \cdot 10^2$	25%	>95%
Ind. gap 2kV/cm	$2.5 \cdot 10^2$	50%	>99%

Table 1.1: Spark charge and spark and signal fraction at the anode measured with the THWELL and THGEM with induction gap configurations, at a gain of 10⁴, Gas: Ne/CH4(5%).

1.3.5 Discussion

The THWELL offers several advantages over the conventional THGEM with an induction gap: a thinner detector configuration and a lower discharge probability for a given gain, probably as a consequence of the different field distribution at the hole edge. On the other hand, the absence of an induction gap may be problematic with sensitive readout electronics, as the entire spark charge of occasional (more rare) discharges goes directly to the readout circuitry. To circumvent this problem, one may consider adding some spark-protection mechanism, either to the detector structure itself, or to the readout electronics, or to both. One such possibility, which will be discussed in the following sections, is the use of a resistive anode for spark quenching.

1.4 Well-THGEM with resistive anode (RWELL)

1.4.1 Motivation

A possible solution investigated here for discharge quenching in THWELL configuration is to close the THGEM hole with a resistive layer on top of an insulating substrate, with the conductive readout pads underneath. In this scheme the pads pick up the signal inductively, rather than directly. Thus, if a spark occurs its charge does not flow directly to the readout electronics. This configuration was tested in a beam, as discussed in Chapter 1.2 above (Fig. 1.2.5).

The use of a resistive layer has a second advantage: it allows a dramatic reduction in the discharge magnitude by holding the charge in the region of the hole for a certain time. In contrast to a conductive anode, where the relaxation time (i.e., the typical time for the conduction electrons to rearrange) is of order of attoseconds ($\tau \approx \frac{\epsilon_0}{\sigma}$ where $\sigma_{cu} = 6 \cdot 10^7 \Omega^{-1} m^{-1}$), on the resistive surface the diffusion time of the electrons out of the hole bottom is of the order of ≈ 10 ns [43].

Once a discharge occurs in the hole, electrons accumulate on the resistive layer. The presence of the charge switches off the electric field in a limited area around the point where the discharge occurred [5]. This quenches the magnitude of the discharge blocking additional charge transfer between the THGEM top and hole bottom before the entire electrode is depleted.

1.4.2 Geometry and preparation

The resistive layers used in this work were produced by spraying a mixture of graphite particles and epoxy binder on 200 microns thick G-10 insulating sheets [44]. The graphite concentration determined the surface resistivity of the layer, typically ranging from ~ 100 k Ω/\square to ~ 10 M Ω/\square . The G-10 sheet with its resistive coating was mounted on top of the readout pads, immediately below and in direct contact with the bottom of the single-faced THGEM, forming the resistive THWELL, or RWELL for short (figure 1.4.1). A copper terminal on the side of the coated G-10 sheet was used to connect the resistive layer to ground.

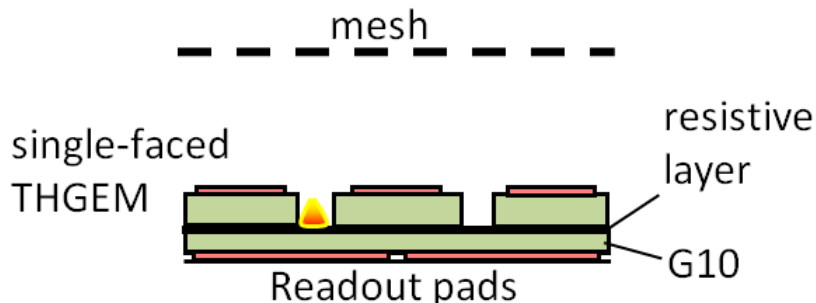


Figure 1.4.1: Resistive WELL (RWELL) configuration. The single-faced THGEM is set on top of a resistive layer deposited on a thin G10 sheet (here 0.2 mm thick), laid on top of the readout pads. The pads pick up an induced signal through the resistive film and the thin G10 foil, rather than directly collecting the avalanche charge.

1.4.3 Gain and pulse measurements

The gain curve of the RWELL configuration was measured and compared to THWELL structure, using the same procedure described in section 1.3.2. Note that the signal (DC current or single pulses) was recorded from the copper pads behind the coated G-10 sheet and not from the resistive layer itself. Gain measurements were taken for a resistive layer of $10 \text{ M}\Omega/\square$. Since the transparency (signal transmission) of resistive layers is close to 1 for surface resistivities larger than $\sim 1 \text{ M}\Omega/\square$ [45], the gain curve was expected to be the same for the $10 \text{ M}\Omega/\square$ RWELL and THWELL. This was indeed verified experimentally, as shown in figure 1.4.2.

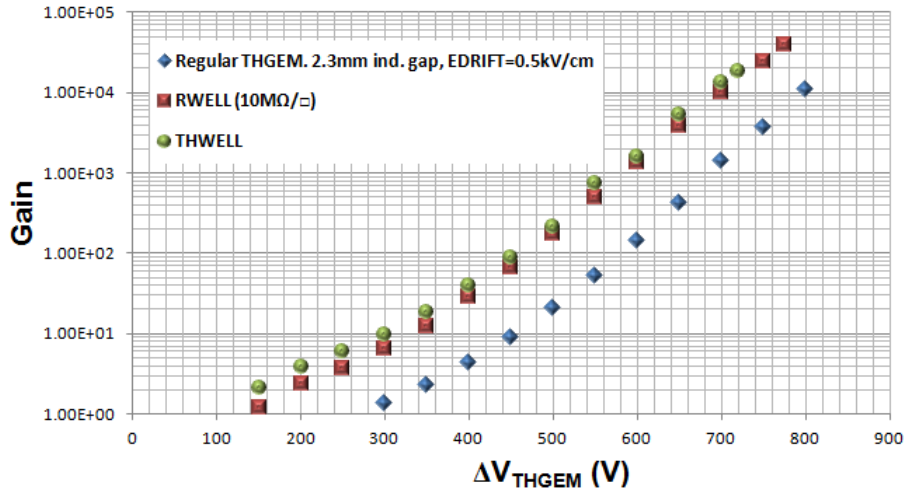


Figure 1.4.2: Gain curves for THWELL, $10 \text{ M}\Omega/\square$ resistive-WELL (RWELL) and regular THGEM with 2.3mm induction gap. In all cases the electrode parameters were: thickness 0.4mm, hole diameter 0.5mm, hole spacing 1 mm, rim size 0.1 mm. The gains were measured in Ne/5%CH4 with 8 keV X-rays.

In addition, there was no significant difference between the pulse shape of signals recorded with the charge-sensitive preamplifier from the THWELL and $10 \text{ M}\Omega/\square$ RWELL – figure 1.4.3.

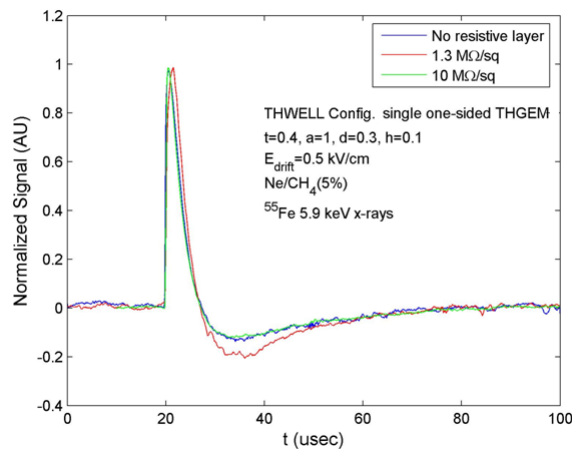


Figure 1.4.3: Pulse shapes for the THWELL, $1.3 \text{ M}\Omega/\square$ and $10 \text{ M}\Omega/\square$ RWELLs. The pulses were measured in Ne/CH4(5%) with 8 keV x-rays with a charge sensitive preamplifier

1.4.4 Discharges with a resistive anode

The discharge magnitude and probabilities were measured for the $10 \text{ M}\Omega/\square$ RWELL, and compared to that of the THWELL using the same method as in sec. 1.3.4. The average spark charge was found to be ≈ 15 fold lower than for the THWELL. The discharge probability was also found to be significantly lower for the RWELL, as shown in figure 1.4.4. While the reduction in discharge magnitude was expected (based on the arguments given in section 1.4.1), the reduced discharge probability was unexpected and yet to be understood.

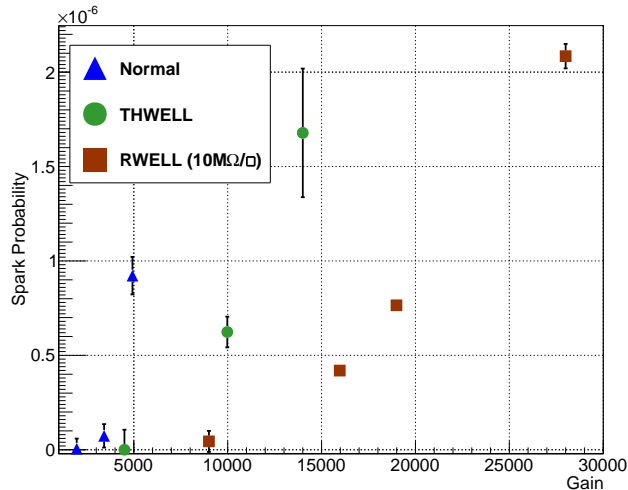


Figure 1.4.4: Discharge probability for the THWELL, $10 \text{ M}\Omega/\square$ RWELL and regular THGEM with 2.3 mm induction gap. The measurements was done with 0.5mm diameter collimated 8 keV x-ray beam, at flux of $10\text{kHz}/\text{mm}^2$

1.4.5 Gain vs. Rate

The delayed clearance of avalanche electrons from the hole bottom could, in principle, affect the gain of the RWELL structure at high rates, as observed typically in RPC detectors [46]. To investigate this question, the gain dependence on the rate of radiation was measured using the Oxford x-ray generator for the $10 \text{ M}\Omega/\square$ RWELL. The results are shown in figure 1.4.5. The gain drop observed ($\sim 50\%$ at $1\text{MHz}/\text{mm}^2$) is similar to that of previous measurements made with regular THGEM structures [47], suggesting that the main contribution to the loss of gain at high rates is the clearance time of the avalanche ions from the hole, which is $\approx 1\mu\text{sec}$ (see sec. 1.3.3), and not the electron spread on the surface of the resistive layer (with the characteristic time of $\lesssim 1 \mu\text{sec}$).

1.4.6 Charge propagation

Electrons moving on the surface of the resistive layer induce signals on the readout pads underneath. We studied this effect experimentally by recording the induced signals on the activated pad and on the neighboring ones, of $1 \times 1 \text{ cm}^2$, with accompanying simulation work to further understand the observed signal shapes. The simulation was based on a theory given in [48], whose main points are summarized below.

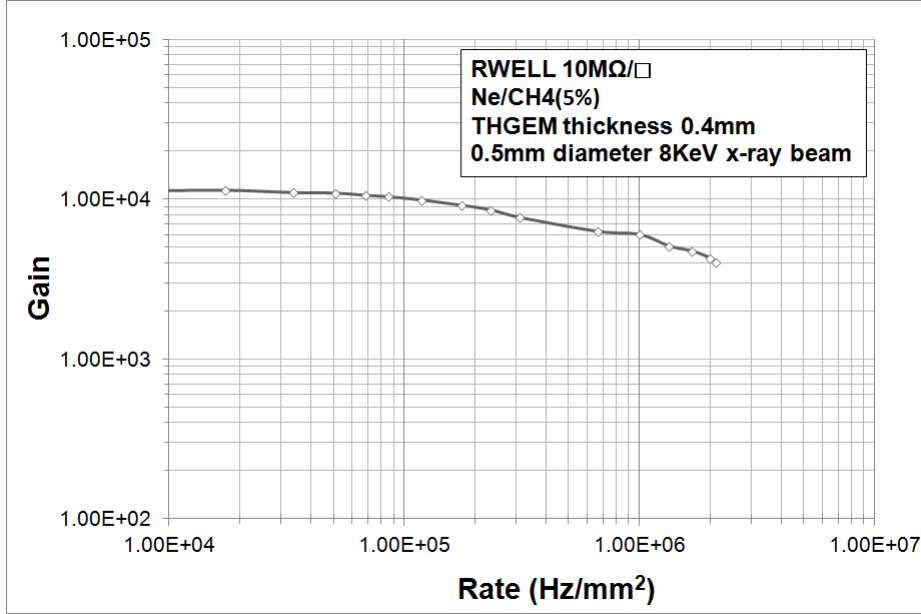


Figure 1.4.5: Rate dependence of the gain in the 10 MΩ/□ RWELL.

Charge dispersion phenomena The spatial spread of the charge on the resistive layer is governed by the diffusion equation:

$$\frac{\partial \rho(r, t)}{\partial t} = \frac{1}{RC} \Delta \rho(r, t) \quad (1.4.1)$$

where Δ is the Laplace operator, $\rho(r, t)$ is the charge density function, R is the surface resistivity of the layer and C is the capacitance determined by the spacing between the anode and readout planes. Here we will denote $\tau = RC$ as the characteristic diffusion time constant of the detector.

In the case where the initial charge distribution can be approximated by delta function, i.e. $\rho(r, 0) = \delta(r)$ the solution is a Gaussian:

$$\rho(r, t) = \frac{1}{2(t/\tau)} e^{-r^2/4(t/\tau)} \quad (1.4.2)$$

The realistic initial charge profile is not a delta function, and may be better approximated by a Gaussian distribution of width ω and total charge Q . In this case, the charge density will be obtained by convolving eq. 1.4.2 with the initial Gaussian:

$$\rho(r, t) = \frac{Q}{2\pi\sigma^2(t)} e^{-r^2/2\sigma^2(t)} \quad (1.4.3)$$

where $\sigma(t) = \sqrt{2(t/\tau) + \omega^2}$.

The induced charge on a rectangular pad below the resistive layer can be calculated by integrating the charge density function over the pad area:

$$S_{pad}(t) = \frac{Q}{4} \left[\operatorname{erf}\left(\frac{x_{high} - x_0}{2\sigma(t)}\right) - \operatorname{erf}\left(\frac{x_{low} - x_0}{2\sigma(t)}\right) \right] \left[\operatorname{erf}\left(\frac{y_{high} - y_0}{2\sigma(t)}\right) - \operatorname{erf}\left(\frac{y_{low} - y_0}{2\sigma(t)}\right) \right] \quad (1.4.4)$$

where x_0, y_0 is the position of the avalanche, $x_{high}, y_{high}, x_{low}, y_{low}$ are the pad boundaries and Q is the initial charge after multiplication.

Note that the induced charge equals the total charge on the resistive layer above the pad area. Note also that equation 1.4.4 is valid regardless of the avalanche position relative to the

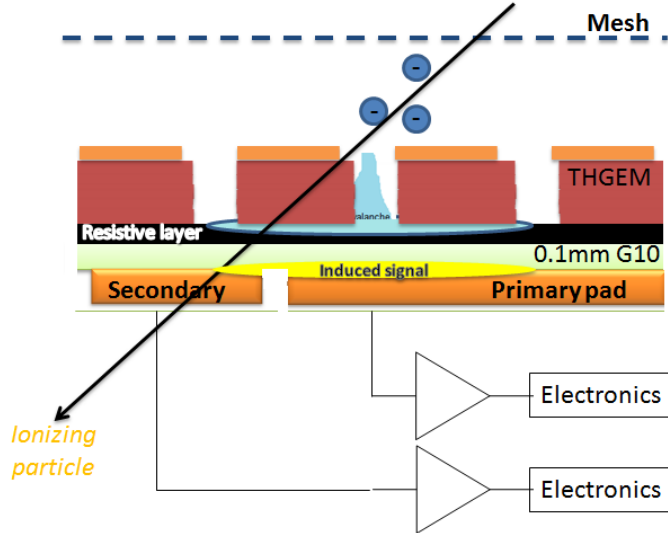


Figure 1.4.6: Schematic of charge dispersion in RWELL cell designed for charge dispersion studies

pad boundaries. If the x_0, y_0 is inside the pad boundaries, $S_{pad}(t)$ will be a monotonically decreasing function. Otherwise, $S_{pad}(t)$ will be initially zero, reach a maximum at some time t_m and will then decrease back to zero. Assume we are irradiating one pad ('primary') (see fig. 1.4.6) and measure the induced signal on its neighbor. Assume further that the avalanche (whose total charge is Q) occurs on the line connecting the pad centers (the pads are identical squares of side s) at a distance d from the inter-pad boundary. The induced charges on both pads is given by:

$$S_{primary}(t) = \frac{Q}{4} \operatorname{erf} \left(\frac{s/2}{\sqrt{2}\sigma(t)} \right) \left(\operatorname{erf} \left(\frac{d+s}{\sqrt{2}\sigma(t)} \right) + \operatorname{erf} \left(\frac{d}{\sqrt{2}\sigma(t)} \right) \right) \quad (1.4.5)$$

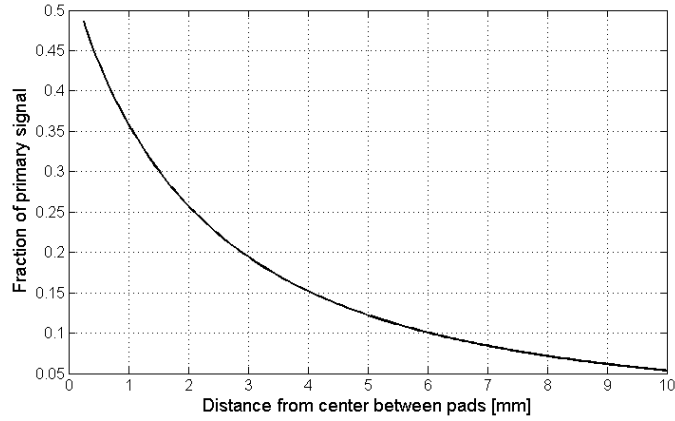
$$S_{neighbour}(t) = \frac{Q}{2} \operatorname{erf} \left(\frac{s/2}{\sqrt{2}\sigma(t)} \right) \left(\operatorname{erf} \left(\frac{d+s}{\sqrt{2}\sigma(t)} \right) - \operatorname{erf} \left(\frac{d}{\sqrt{2}\sigma(t)} \right) \right) \quad (1.4.6)$$

In the experimental measurements of signal propagation described below, two parameters were studied: the time at which $S_{neighbour}$ is maximum, t_m , and the ratio of amplitudes $S_{neighbour}(t_m)/S_{primary}(0)$ ⁴. Figure 1.4.7 shows the simulation results regarding these two parameters as a function of the avalanche distance d from the inter-pad boundary for adjacent $1 \times 1 \text{ cm}^2$ pads with $\omega=0.5 \text{ mm}$ (i.e., equal to the THGEM hole diameter). Note that these curves depend only weakly on ω (results not shown).

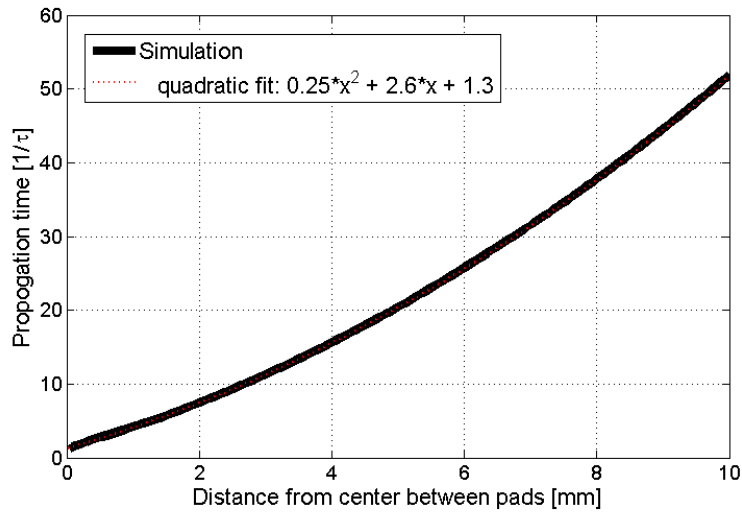
The simulation shows that the amplitude of the signal on the neighbor pad will be as high as $\approx 10\%$ of that on the primary pad when the avalanche occurs above the primary pad's center (assuming ideal electronics). The maximum of the signal will be reached with a delay of $20\tau_{sec}$. For example $1\text{M}\Omega/\square$ surface resistivity with $C=0.1\text{pF}$, the time delay = $2\mu\text{sec}$.

Signal propagation was measured experimentally in the RWELL structure for different values of surface resistivity. The setup of the detector is shown on Fig. 1.4.8. The detector was operated, as before, with $\text{Ne}/\text{CH}_4(5\%)$ at 1 atm. The drift gap was chosen to be 3 mm, in order to avoid alignment systematics. The parameters of the single-faced THGEM were, as before, $t=0.4 \text{ mm}$, $a=1\text{mm}$, $h=0.1 \text{ mm}$ and $d=0.5 \text{ mm}$. The gain of the detector was set to 10^4 ,

⁴In the actual experiment the measured signal on the primary pad has an initial rise reflecting the signal induced by electron movement in the gas before reaching the anode. The measured signal is also affected by the response function of the preamplifier. Both effects are not simulated here.



(a)



(b)

Figure 1.4.7: Simulation of the charge dispersion: (a) Fraction of a signal magnitude measured on the neighbor pad with ideal readout electronics (whose signal is always proportional to the induced charge), for pads of $1 \times 1 \text{ cm}^2$ and infinite resistive layer; (b) The time when the signal is maximal on the neighbor pad, given in units of τ , vs the distance of the avalanche from the center between the pads.

and the drift field to 0.5 kV/cm . Two neighboring 1 cm^2 copper pads were used. The signal from each pad was read by an amplification chain comprising an ORTEC 142A charge-sensitive preamplifier and an OTREC 572A linear shaping amplifier. The amplifiers gain was adjusted to provide the same average amplitude for both pads (when irradiated under the same conditions). The preamplifiers input was protected with two diodes connected back to back in parallel with a $100 \text{ k}\Omega$ resistor, as described in section 1.3.2. The output signal of the linear amplifiers was connected to a 4-channel Tektronix digitizing oscilloscope or an MCA. A collimated 0.5 mm diameter 8 keV x-ray beam, produced by the Oxford generator, was used to irradiate one of the pads (here denoted the 'primary') and the signal was recorded from both the primary pad and its neighbor ('secondary'). By triggering on the primary pad, we measured both signals from the primary and secondary pads. The measured signals are shown on Fig. 1.4.9. The secondary pad signal has two features:

- Initial negative component due to capacitive coupling between two pads: once a signal

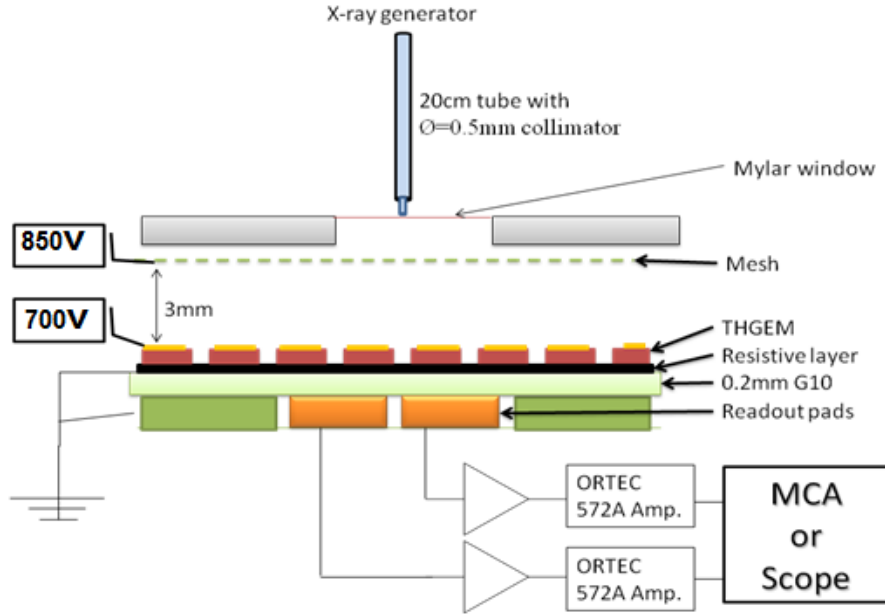
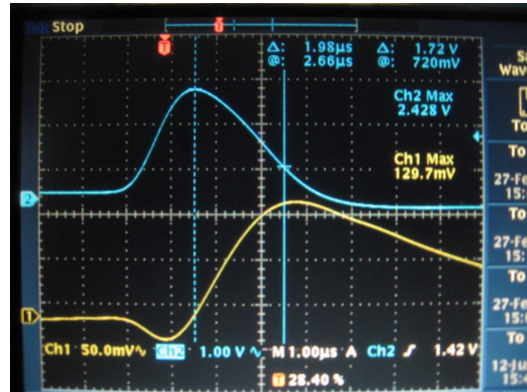


Figure 1.4.8: Experimental setup for charge dispersion measurements.

Figure 1.4.9: Measured signals from the two neighboring pads, with the primary pad irradiated at its center, 5mm away from the inter-pad boundary. The signals shown are averages over 512 pulses. The horizontal scale is $1\mu\text{s}/\text{div}$, Blue - signal from primary pad; Yellow - signal from secondary pad. Resistive layer of $5\text{M}\Omega/\square$.



appears on the primary pad, an induced signal with opposite polarity appears on the secondary pad.

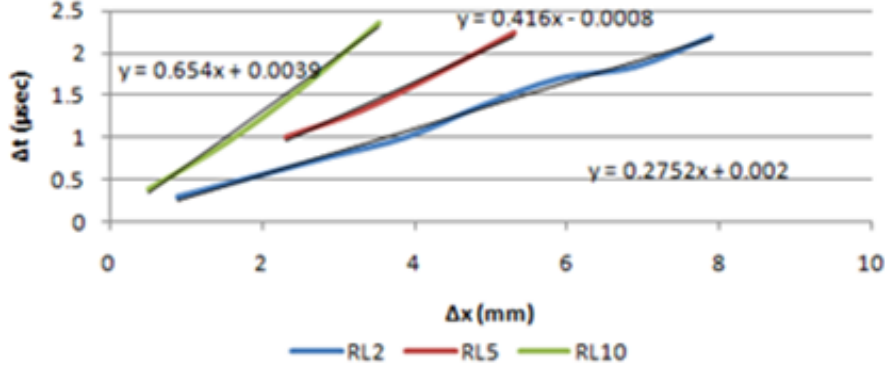
- Positive component due to charge diffusion: while the charge diffuses on the resistive layer it induces a signal first on the primary pad and then on the secondary pads.

The peak of the secondary pad pulse is delayed relative to that of the primary pad. The duration of this delay Δt depends both on the distance of the beam from the inter-pad boundary Δx and on the surface resistivity of the layer, as shown in figure 1.4.10a. The propagation velocity of the signal can be defined as the ratio $\Delta x/\Delta t$ - the inverse of the slope of Δt as a function of Δx . This velocity is shown as a function of the surface resistivity in figure 1.4.10b.

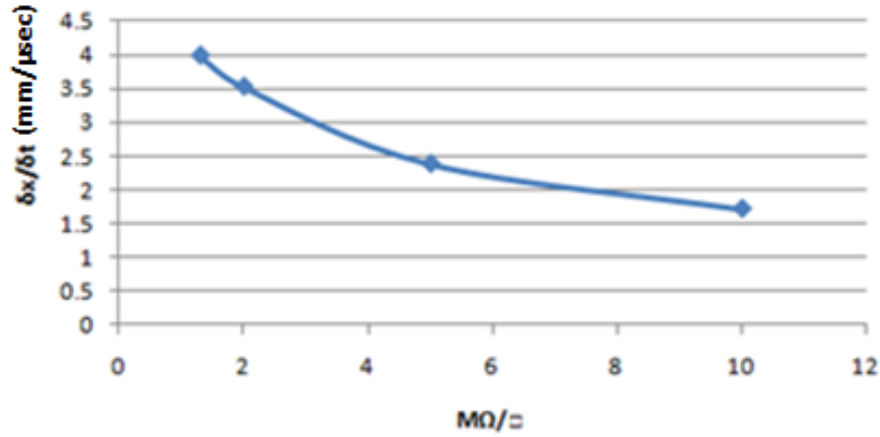
An estimate for the propagation velocity was derived numerically as shown in figure 1.4.7b. For given resistance, velocity of charge and signal propagation fit $t/\tau \approx (x/a)^2$ (a quadratic fit in figure 1.4.7b yields $a=0.5\text{ mm}$) we can express the detector effective capacitance by:

$$C[\text{pF}] = a^2 / (2 \cdot v[\text{mm}/\mu\text{sec}] \cdot d[\text{mm}] \cdot R[\text{M}\Omega/\square]) \quad (1.4.7)$$

For measured velocities in figure 1.4.10b the effective capacitance is $\approx 0.1\text{ pF}$



(a)



(b)

Figure 1.4.10: Signal propagation: (a) Time delay between the maxima of the signals on the primary and secondary pads Δt as a function of beam distance from inter-pad boundary Δx . (b) Signal propagation velocity (the inverse slope of 1.4.10a).

1.4.7 Cross-talk measurements

The application of our detector as sampling elements for DHCAL, requires good understanding of the cross-talk between pads. The readout philosophy relying on counting pads fired above a given threshold requires the lowest possible pad multiplicity (average number of pads picking up a signal per event), which ideally should be as close as possible to 1. At the same time the electronics threshold be kept low, to assure the highest detection efficiency of pad hits.

The diffusive spread of electrons on the resistive layer in the RWELL can result in a high pad multiplicity (or cross-talk), with a delay that increases with the distance from the actual position of the event.

The cross talk between the pads in the RWELL was studied using the same setup employed to measure the signal propagation (Fig. 1.4.8). By irradiating the primary pad and triggering on its signal, we measured the ratio between the amplitude of the signal appearing on the secondary pad and that on the primary one, as a function of the beam distance from the inter-pad boundary:

$$f(x) = \frac{S_{Secondary}(x)}{S_{Primary}(x)} \quad (1.4.8)$$

For example in the oscilloscope image shown in figure 1.4.9, for a resistive layer of $5M\Omega/\square$ with the beam at the pad center, we have $S_{Primary}(5mm) = 2.428V$ and $S_{Secondary}(5mm) = 0.1297V$,

giving $f(5\text{mm}) = 0.053$ which is $>5\%$ of a primary signal. Thus in this case for a gain of 10^4 , primary charge of $n_P = 50$ electrons (typical MIP-induced charge in a $\sim 10\text{mm}$ drift gap in our gas mixture), the signal produced on the secondary pad will be $\sim 4\text{fC}$. Whether this signal will be (falsely) counted as an event, depends on the threshold setting in the actual detector.

Figure 1.4.11 shows a comparison between the cross talk (secondary/primary amplitude ratio) as a function of the beam distance from the inter-pad boundary, measured for the $10M\Omega/\square$ RWELL and THWELL. In the latter, the cross talk between neighboring pads results mainly from events occurring close to the inter-pad boundary, when the primary electrons drift to holes on both sides. As in the above example, for the $10M\Omega/\square$ RWELL the cross talk is larger than 5% for events occurring up to about 5 mm from the boundary. Without using additional information, such as measurement of the delayed appearance of the maximum of the pulse, this will likely result in prohibitively large values of pad multiplicity.

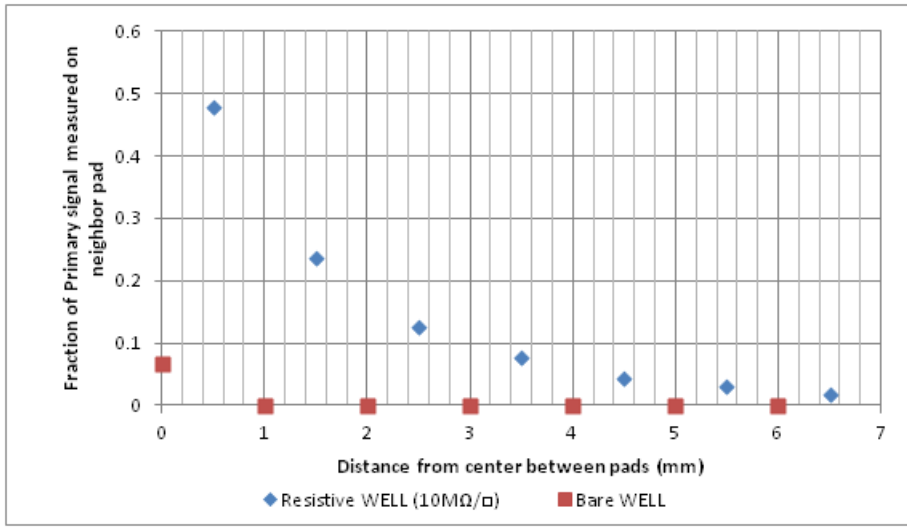


Figure 1.4.11: Neighbor pad signal amplitude as a function of the beam distance from the boundary between two adjacent pads, for a THWELL and RWELL of $10M\Omega/\square$. The beam (0.5mm diameter 8 keV x-ray) was scanned across a line connecting the centers of two neighboring pads and the average signal amplitudes were recorded from both pads. The amplitudes are shown normalized by the value of the primary pad signal as it defined in Eq.1.4.8.

The cross-talk can be calculated numerically from equation 1.4.5. The numerical simulation is shown in Fig. 1.4.7a. The Cross talk seems to be higher using simulation with ideal electronics while in the experiment the cross talk is lower (10% of the signal measured at the distance of 2.7mm while the numerical simulation gives the same fraction at the distance of $\approx 6\text{mm}$).

1.4.8 Discussion

While achieving spark quenching, and decoupling the direct charge from the readout electronics, the pad multiplicity is sacrificed in the RWELL: the cross talk measured with the resistive layer is leading to high multiplicity between the pads. This is not an issue in applications aiming for position measurement by center-of-gravity computation of the induced charge, e.g. on anode strips [14]. Also, as noted above, the different rise times and delayed maxima can serve, in principle, for identifying the primary pad and discarding the neighbors. However, for applications such as the ILC SiD DHCAL the high multiplicity in the RWELL could pose some problem. In the next section we will present and discuss a possible solution.

1.5 Segmented-GRWELL

1.5.1 Motivation

In order to avoid charge propagation across the resistive surface of the RWELL structure, charge drain channels may be added on, or directly underneath this surface (and in electrical contact with it). Such channels, namely a square grid of thin conductive lines along the pad edges, can block electrons from diffusing across pad boundaries, thus preventing the considerable cross-talk observed in the RWELL. As in the RWELL, discharges occurring in the regions between the grid lines are effectively quenched

1.5.2 Configuration

The G-10 sheet serving as the substrate on which the resistive layer is deposited was prepared (prior to deposition) with grid of $200\ \mu\text{m}$ wide Cu lines, 1 cm apart, matching the boundaries between readout pads located behind the sheet. The resistive layer was then sprayed on top, covering both the grid lines and exposed G-10 areas between them. The G-10 sheet used in the study was $200\ \mu\text{m}$ thick and the surface resistivity was $10\ \text{M}\Omega/\square$.

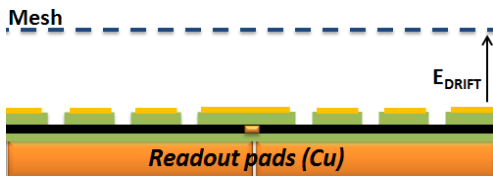


Figure 1.5.1: Segmented-GRWELL

This resistive-anode structure was initially coupled to a regular single-faced THGEM in WELL configuration with an hexagonal lattice of holes covering its entire active area. The resulting structure was named the gridded-RWELL, or GRWELL (fig. 1.5.1). However, two problems were observed in this configuration: (1) discharges occurring in holes directly above the grid lines were not quenched, and (2) avalanches occurring

in holes directly above or close to these channels induced a faint signal on the readout pads, because the lower local transparency near the drain channels. To solve these problems, the gridded resistive anode was subsequently investigated with a segmented-THGEM electrode having a square lattice of holes covering only the pads area, with 1 mm wide copper bands (with no holes) above the underlying resistive-anode grid lines. The purpose of the bands was to prevent avalanche formation above the grid. The combined structure of gridded resistive anode and segmented THGEM the segmented-GRWELL is shown in figure 1.5.2.

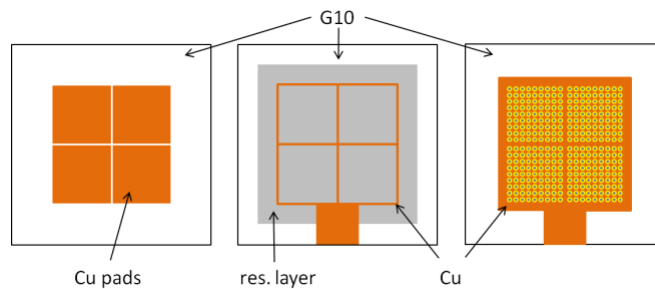


Figure 1.5.2: A segmented-GRWELL layout: Left the Cu pad array (connections not shown). Middle - the gridded resistive anode: the resistive layer is deposited on top of a grid of copper lines printed on a thin G10 sheet. The grid lines, matching the pads boundaries, rapidly drain avalanche electrons reaching the resistive layer, to reduce their diffusive spread to neighboring pads. Right the segmented single-faced THGEM, with a square-hole pattern; the hole-less zones between the active THGEM ones, matching the grid lines of the resistive anode, prevent avalanche formation in their vicinity (see text).

1.5.3 Segmented-GRWELL electron collection efficiency

High drift fields, and large hole spacing can lead to loss of primary electrons on the top of the THGEM due defocussing effects (i.e., the electrons created in the drift gap may land on the copper surface rather than being focused into the holes). For the segmented-GRWELL this can lead to loss of detection efficiency for events occurring above the hole-less bands. This effect was studied for varying widths of the hole-less bands and for varying drift fields, using the GARFIELD9 program [18].

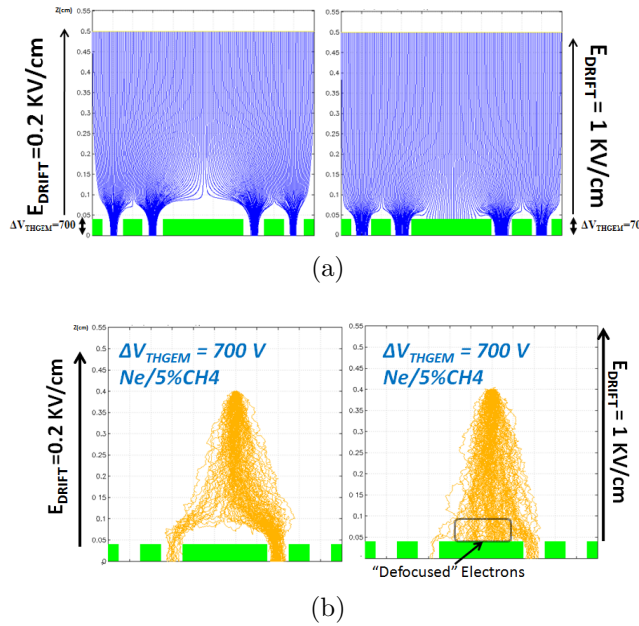


Figure 1.5.3: Field lines and drift of the electrons for $E_{DRIFT}=0.2,1\text{kV/cm}$, simulated using GARFIELD 9 with Magboltz 7 [18, 39], for the segmented-GRWELL configuration with $t=0.4, a=1, h=0.1, d=0.5$ and $s=2\text{mm}$: (a) Drift lines; (b) Simulated electron drift, for primary electrons above the band, 0.25 to the right of its center

Figure 1.5.3a shows the drift lines for a segmented-THGEM with 2 mm wide bands (with the band width, s , defined as the distance between the edges of holes on the opposing sides of the band). The drift lines⁵ were generated by creating electrons in regular intervals 5 mm above the anode, and tracking their trajectories for zero transverse diffusion. The calculation was performed for drift fields of 0.2 and 1 kV/cm. Figure 1.5.3b shows the actual trajectories of electrons starting 4 mm above the anode 0.25 mm to the right of the band center (this time with transverse diffusion). As is evident the figure, using a drift field of 1 kV/cm would result in a significant charge loss, whereas for 0.2 kV/cm essentially all of the primary electrons (for the particular starting point chosen) are focused into the holes.

The collection efficiency for primary electrons created above the active areas of the segmented-GRWELL, is essentially 1. To study the collection efficiency of electrons starting above the band and its dependence on the drift field, drift gap

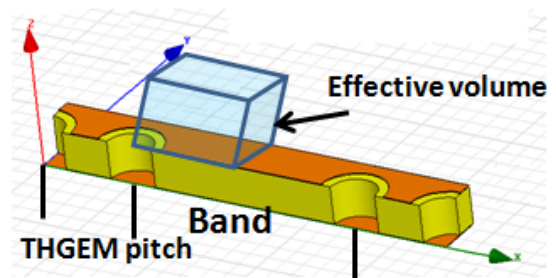
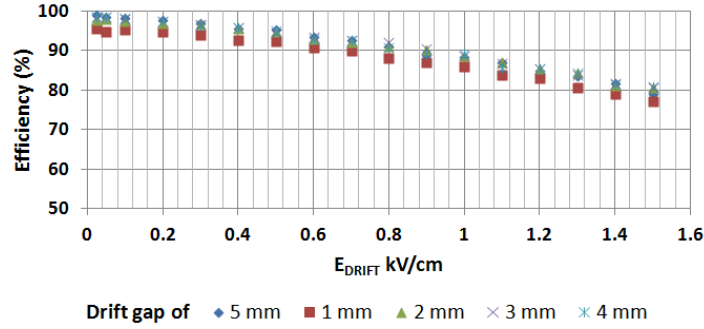


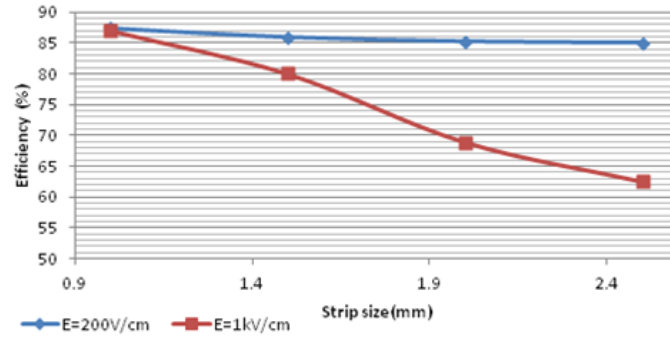
Figure 1.5.4: Effective volume above the band: Within this volume, the electrons was uniformly distributed.

⁵For zero transverse diffusion the drift lines coincide with the field lines

and band width, a series of GARFIELD simulations were performed. First, we simulated the electron collection efficiency for various drift gaps and drift fields. 5000 electrons were generated in an effective volume above the band (see figure 1.5.4), with $s=1\text{mm}$. The resulting average collection efficiency curves are shown in figure 1.5.5a. We found that at a field of 0.2kV/cm and a drift gap of 5mm , the collection efficiency of electrons generated in the effective volume is $> 97\%$. In addition, we also simulated the collection efficiency for different band width for drift fields of 0.2 and 1 kV/cm (see Fig. 1.5.5b). In this simulation the electrons were uniformly distributed along the line above the center of the band.



(a) Average collection efficiency for various drift gaps simulated as a function of the drift field, for $s=a=1\text{mm}$.



(b) Collection efficiency for $E_{DRIFT}=0.2$ and 1kV/cm simulated as a function of the drift field for electrons. The electrons uniformly distributed along the line of 5mm from the center of the strip.

Figure 1.5.5: Collection efficiency Simulation in the segmented-GRWELL as function of drift gap and drift field

We can conclude that in order to operate the detector with a high efficiency, low drift fields (of order of 0.2 kV/cm) are necessary. From figure 1.5.5b we can also conclude that for this field the collection efficiency is only weakly dependent on the band width. Note that it is not desirable to further reduce the drift field, when the drift gap is $1\text{-}2\text{cm}$, as this will result in a steep increase of the transverse diffusion of primary electrons. The plot of diffusion coefficients for $\text{Ne/CH}_4(5\%)$ mixture is shown in figure 1.5.6.

1.5.4 Transparency measurements

The presence of copper grid lines below the resistive layer, was shown in preliminary experiments to result in some loss of induced signal transparency (through the resistive anode) when using a regular single-faced THGEM with an hexagonal hole pattern. This effect was also investigated for the segmented-GRWELL, for a band width of 0.68mm and 1.24mm strips. The transparency

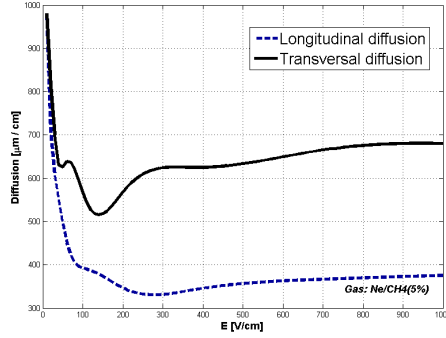


Figure 1.5.6: Diffusion coefficients for Ne/CH₄(5%) mixture

was defined as:

$$T = \frac{S_{Anode}(x)/S_{TOP}(x)}{S_{Anode}(center)/S_{TOP}(center)} \quad (1.5.1)$$

where S is the signal amplitude measured from the THGEM top/anode, normalized to the ratio measured at the center of the pad (where the transparency is 100%). The results of the measurement, performed, again, by scanning the beam across a line between the pad centers, are shown in figure 1.5.7. As shown in the figure, there is still non negligible loss of transparency up to 2 mm away from the pad boundary. It could affect the detection efficiency.

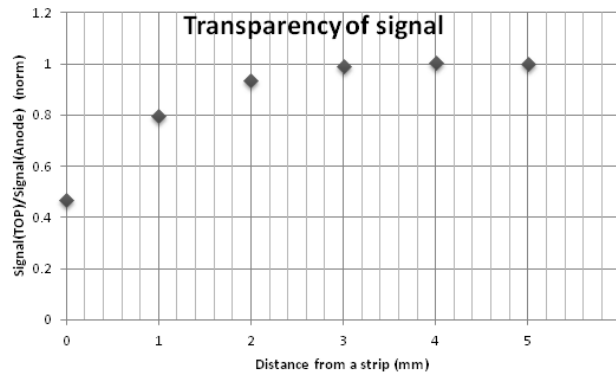


Figure 1.5.7: Transparency measurement: Primary pad signal amplitude as a function of the beam distance from the boundary between two adjacent pads, for segmented GRWELL. The beam (0.5 mm diameter 8 keV x-ray) was scanned across a line connecting the centers of two neighboring pads and the average signal amplitudes were recorded from both pads.

1.6 Summary, conclusion and discussion

In this work we have studied the properties of various WELL-type THGEM configurations, aiming at the thinnest possible sampling-element design with a low discharge probability, to meet the requirements of the SiD DHCAL.

The simplest structure, THWELL, showed superior properties compared to the normal THGEM/induction gap configuration (besides being significantly thinner), namely a 10-fold higher gain at the same voltage and 10-fold lower discharge probability (at an effective gain of ~ 5000). The detection efficiency and average pad multiplicity for the THWELL, while not yet measured directly in a beam test, should be similar to that of the normal THGEM/induction gap configuration, namely $>95\%$ efficiency and ~ 1.2 multiplicity.

A potential disadvantage of the THWELL, however, is that when a discharge occurs, its entire charge flows directly to the readout electronics with possible harmful consequences. This led us to consider the RWELL, where a continuous resistive layer, with a surface resistivity of $\sim 10 \text{ M}\Omega/\square$, deposited on top a thin insulating sheet is placed in front of the readout pads, forming the WELL bottom electrode. The resistive layer has three advantages: first, it protects the sensitive readout electronics from direct discharge currents; second, it reduces the amount of charge flowing during a discharge by a large factor (~ 15 in this work), and third, it further reduces the discharge probability compared to the THWELL. In a preliminary beam test with 150 GeV/c muons, the RWELL, operated at a gain of ~ 4000 , displayed stable operation with a very low discharge probability ($< 2 \times 10^{-6}$) one order of magnitude less than that of a normal THGEM/induction gap detector operated in the same beam conditions at a gain of ~ 3000 .

The disadvantage of the RWELL, however, is that unless special signal processing algorithms are employed, a single avalanche results in multiple pad triggering because of the diffusive spread of electrons across the resistive surface. To solve the problem of high pad multiplicity, the continuous resistive layer was modified to incorporate a square grid of thin copper lines, matching the pad boundaries, immediately underneath it. The resulting structure, GRWELL, displayed negligible cross-talk between adjacent pads, but suffered from unquenched sparks in holes directly above the grid lines, as well as from reduced transparency of the induced signal for avalanches occurring close to the grid. To mitigate this the hole structure of the THGEM was modified, leaving copper bands with no holes above the grid. This structure, the segmented-GRWELL, forces the avalanches to occur away from the grid lines, thus regaining the spark-quenching capability of the RWELL and reducing the effect of transparency loss. A quantitative analysis of the detection efficiency and pad multiplicity of the segmented-GRWELL, which takes into consideration possible inefficiencies of electron collection and the reduced induced signal amplitude near the copper strips is underway. The actual performance of this structure will be tested in beam conditions in the near future.

The total thickness of an active sampling element based on the segmented-GRWELL detector with a drift gap of 4mm, is less than 5mm excluding the readout electronics. This can potentially reduce the total radius of the SiD DHCAL, thus significantly reducing the cost of the superconducting coil.

One should note that the discharge probability of the detector, when operated in the highly ionizing environment of the SiD DHCAL, may be higher (at a given effective gain) than that measured with 8 keV x-rays in the lab or with MIP test beams. This may require operation at lower effective gains, which may in turn compromise the MIP detection efficiency, unless a corresponding reduction in electronic noise in the readout system can be achieved.

Another point to consider that the discharge magnitude scales with the detector area (due to increase of the detector capacitance). This can be handled by segmenting the conductive surfaces of the detector to smaller units with reduced capacitance. Segmentation can be done at various levels, e.g. by dividing the area of the detector to a few smaller rectangles (with a typical size of a few cm^2), by dividing the area to strips of interconnected holes (with neighboring strips connected to each other through large resistors), or ultimately by separating individual holes from one another using resistive links. The latter option is shown schematically in figure 1.6.1.

This scheme is similar to the THCOBRA geometry [49], but here the holes are interconnected through a resistive link rather than copper. When a discharge occurs inside a particular hole, its two sides are momentarily interconnected by a plasma filament; the total charge passing through this filament will depend on the resistance of the links to the neighboring holes. This resistance should be such that the RC time corresponding to the link and the capacitance of the conducting rim surrounding a hole would be longer than the lifetime of the plasma filament during a discharge. Preliminary studies regarding the duration of discharges are underway, as

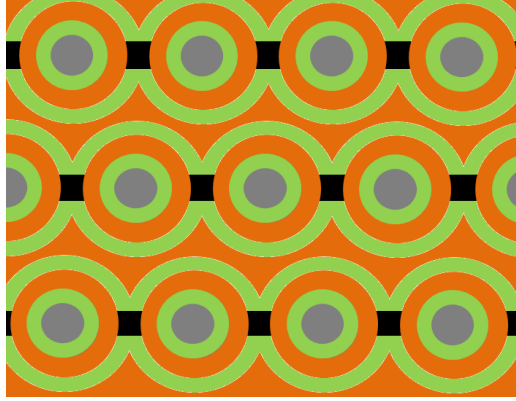


Figure 1.6.1: Semi-resistive THCOBRA detector, similar to the COBRA geometry [49] but with resistive links connecting the holes.

well as initial calculations regarding the detector scheme shown in figure 1.6.1.

To conclude, this work demonstrates the potential of Well-type THGEM detector structures, in particular those incorporating a resistive anode, as thin, stable and efficient sampling elements for calorimetry applications. These structures can be further improved to make the effect of occasional discharges negligible, thus forming a promising direction of novel detector development for various high energy physics experiments in general, and in the SiD DHCAL project in particular.

Part II

Data Analysis

Mass reconstruction technique in di-tau resonances for Higgs searches with ATLAS detector

2.1 Introduction

The Standard Model (SM) of particle physics is a successful theory that describes the strong, electromagnetic and weak interactions of matter on the subatomic level. Its predictions have stood up over the years to the test of precise experimental measurements. The theory remains to this day as a strong predictive force, though some questions have been left unanswered.

The Large-Electron-Positron Collider (LEP) that was in operation from 1989 to 2000 broke the electroweak scale at the end of 2000 by colliding leptons at the center of mass energy of 209 GeV. The Tevatron accelerator, which was in operation from 1983 to 2011, collided protons with anti-protons at the center of mass energy of 1.96 TeV. Neither experiments were able to generate a sufficient number of Higgs bosons to be observed. Today, using the Large Hadron Collider (LHC), we have reached the point where we observe collisions at energies well above the electroweak scale, with a high collision rate. The LHC accelerating protons with a center of mass energy of 7 TeV have a significantly higher prospective production rate of the elusive Higgs boson.

In the course of 2011, the LHC delivered an integrated luminosity of 5.61fb^{-1} , which should generate ~ 100 thousand hypothetical Higgs bosons at a mass of 125 GeV [50]. According to the SM, the Higgs boson lifetime typically varies in range, between 10^{-27} - 10^{-21} sec., and for a Higgs boson of mass 125 GeV, its lifetime is predicted to be $\tau < 10^{-21}$ sec. Since Higgs decays almost instantaneously, it might be observed only through its decay products. The Higgs boson's width and the decay channels branching ratios (BR) are shown in figure 2.1.1.

The search for the Higgs boson with the ATLAS experiment is performed by searching for it through five of its decay modes: $b\bar{b}$, $\gamma\gamma$, $\tau\bar{\tau}$, WW and ZZ. In December 2011, both ATLAS and CMS experiments succeeded in narrowing down the allowed mass range for the Higgs considerably. Only the range of approximately 115-130 GeV was permitted for a light Higgs, with a 95% confidence level (CL). In addition, they reported (independently) that their data hints at a possible deviation from a background-only expectation, for few sensitive channels¹ around a mass of 125 GeV [51, 52]. In order to discover the Higgs boson, it is not enough to observe a deviation from a background-only hypothesis, but rather, one must measure the different branching ratios and compare them to the SM expectation. Therefore, it is important to observe the Higgs signal in the $b\bar{b}$ and $\tau\bar{\tau}$ channels as well.

¹ATLAS and CMS Collaborations showed an excess in $\gamma\gamma$, and $ZZ \rightarrow 4\ell$ Higgs decay channels.

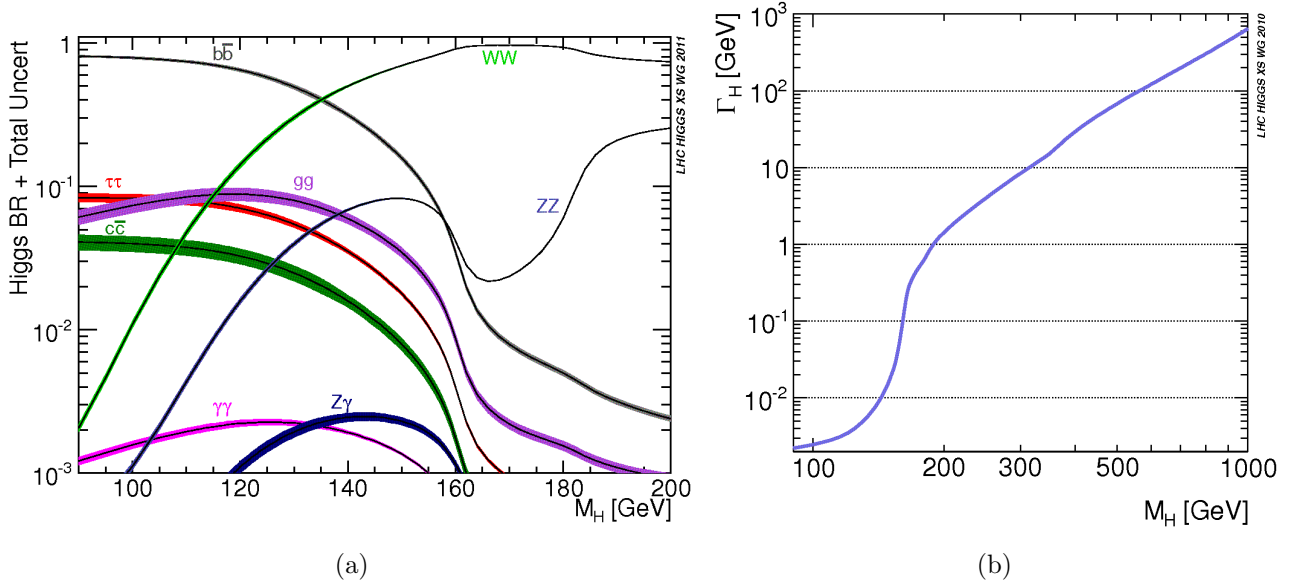


Figure 2.1.1: Higgs decay: (a) Higgs Branching Ratios for various decay channels; (b) Higgs total width as a function of Higgs mass [50]

With its current available sensitivity, using the ATLAS detector, $H \rightarrow \tau\tau$ channel is able to exclude a cross section of ~ 3 times the Standard Model theoretical prediction for Higgs boson of 125 GeV mass with 95% CL [53]. Each τ lepton has two decay modes - hadronic and leptonic. Thus the $H \rightarrow \tau\tau$ decay channel has 3 sub-channels: had-had, had-lep and lep-lep.

The $H \rightarrow \tau_{lep}\tau_{lep}$ channel in the 2011 analysis excluded $\sim 5 \times$ the Standard Model theoretical prediction for Higgs boson of 125 GeV mass with 95% CL. The dominant irreducible background for the $H \rightarrow \tau\tau$ channel is $Z \rightarrow \tau\tau$. Due to the presence of unmeasured particles (2-4 elusive neutrinos) the precise resonance measurement and separation of the higgs from $Z \rightarrow \tau\tau$ background is the major challenge. The goodness of the resonance mass reconstruction is essential to have sufficient sensitivity to be able to observe the Higgs boson in this decay mode.

In the present work, we aim to improve the sensitivity of $H \rightarrow \tau\tau$ decay channel, by improving the existed mass reconstruction method.

This chapter contains the following discussion: In section 2.2, the experimental apparatus of the LHC accelerator and the ATLAS detector are introduced. In section 2.3, the theoretical background related to Standard model is presented, emphasizes the Electroweak symmetry breaking caused by the Higgs mechanism. In section 2.4, the Higgs decay channel, where the Higgs boson decays to two tau leptons, which decay to one electron and one muon is presented as analyzed by the ATLAS $H \rightarrow \tau_{lep}\tau_{lep}$ working group. In section 2.5, the available mass reconstruction techniques are presented, including the Missing Mass Calculator (MMC) [54]. In section 2.6, the MMC reconstruction technique is discussed, emphasizing our contribution: while implementing this algorithm, we encountered few limitations. In this section we describe the limitation of the presented technique and suggest a new way of implementation. One of the limitations is the low performance speed, ~ 20 sec. per event, for $H \rightarrow \tau_{lep}\tau_{lep}$ which led to not using MMC in this particular channel. By introducing our Modified MMC, we succeed to increase its performance speed to be $\lesssim 1$ sec/event and also manage to overcome its limitation by presenting it in a pure analytical manner - the Modified MMC. In section 2.7 we showing the improved performance of the MMC algorithm with respect to the existed mass estimators in this particular decay channel.

2.2 Experiment

The Large Hadron Collider (LHC) [55] is the worlds newest and most powerful tool for Particle Physics research. LHC sits in a circular tunnel spanning 27 km at the CERN² near Geneva. The tunnel is buried 50 to 175 m underground, and straddles the Swiss and French borders on the outskirts of Geneva.

The concept of the LHC has been discussed since the beginning of the 1980s [56], yet only in March 2010 did the LHC finally accelerate the protons to 3.5 TeV energy, initiating collisions at $\sqrt{s} = 7$ TeV.

To keep the proton beam in a circular trajectory, the beams are confined using strong superconducting magnets producing magnetic fields of 8.33 Tesla (at 7 TeV). The protons are extracted from hydrogen gas and first accelerated up to 50MeV in a linear accelerator LINAC2. Protons are transferred to the Proton Synchrotron Booster (PSB), where they are separated into bunches by the radio frequency cavities which accelerate them to 1.4 GeV. The protons from the Booster enter into the Proton Synchrotron (PS). Here they are accelerated to 25 GeV before passing into the Super Proton Synchrotron (SPS), which accelerates the proton beams to up to 450 GeV. The final acceleration is done by injecting them to the LHC ring, where they reach the energy of 3.5 TeV per beam

LHC was designed to provide proton beams of 1.1×10^{11} protons per bunch, with 2808 bunches and bunch spacing of 25 ns producing instantaneous luminosity³ of $\mathcal{L} = 1 \times 10^{34} \text{cm}^{-2} \text{s}^{-1}$ which is 20 times more than the maximal intensity delivered by the Tevatron. For the majority of the data collected in 2010, the LHC was run with 368 filled bunches per beam, with 75 ns bunch spacing and $\mathcal{L} = 2 \times 10^{32} \text{cm}^{-2} \text{s}^{-1}$. In 2011, most of the data was collected with 50 ns bunch spacing, with 1380 filled bunches with 1.5×10^{11} protons per bunch producing instantaneous luminosity of $\mathcal{L} = 3.6 \times 10^{33} \text{cm}^{-2} \text{s}^{-1}$.

The delivered data (or total integrated luminosity) is expressed in units of inverse cross section, so the total number of events can be calculated from:

$$N_{events} = \sigma \times \mathcal{L} \quad (2.2.1)$$

where σ is the process cross section, \mathcal{L} is the integrated luminosity defined by $\mathcal{L} = \int \mathcal{L} dt$. The collisions at 7 TeV in 2011 delivered 5.61 fb^{-1} to both ATLAS and CMS experiments. The amount of data as a function of time is shown in Fig. 2.2.1. The LHC is designed with four separate collision points for the four detectors built at these points. One of these detectors is A Toroidal LHC Apparatus, or ATLAS.

2.2.1 ATLAS detector

The ATLAS (A Toroidal LHC Apparatus) detector [57] is a multi-purpose particle physics detector, designed to detect particles and measure their properties. A sketch of the detector is shown in Figure 2.2.2, where one can see its main parts.

The main parts of the detector are the Inner detector, which is designed to measure tracks of charged particles; The Electromagnetic calorimeter (ECAL) which is responsible for measuring the energy of electrons and photons whereas hadrons deposit most of their energy in the Hadronic calorimeter (HCAL); and the Muon spectrometer (MS) which designed to measure the momenta of muons with high precision.

²European Organization for Nuclear Research: www.cern.ch

³Luminosity: is proportionality factor which is relate the differential rate to differential cross section: $\frac{dR}{d\Omega} = \mathcal{L} \frac{d\sigma}{d\Omega}$

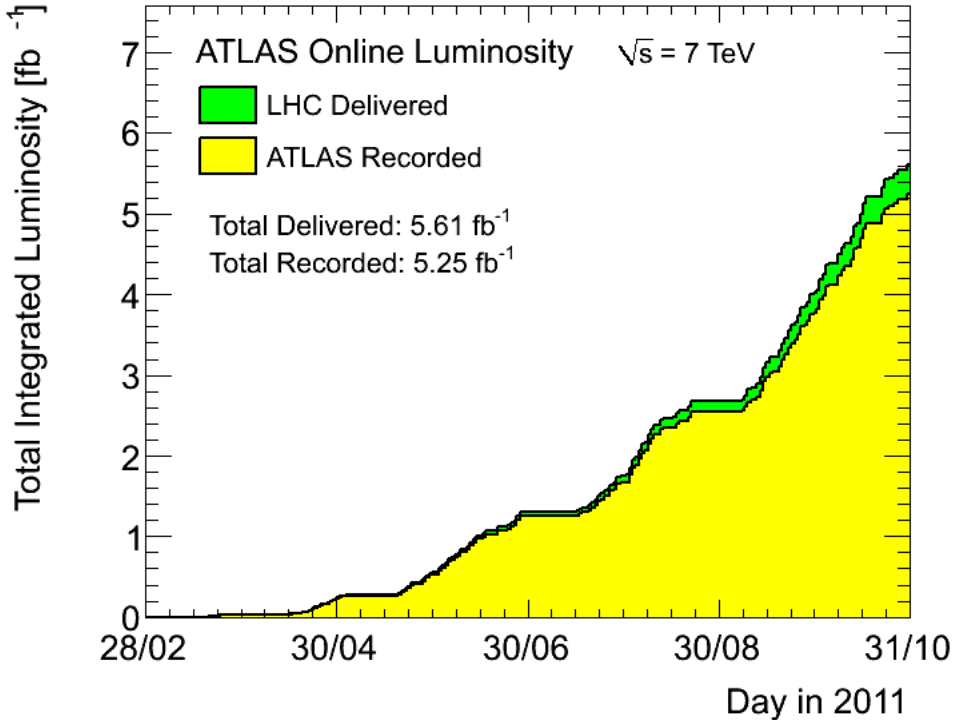


Figure 2.2.1: LHC integrated luminosity

The Inner detector The cylindrical inner detector, which has a length of 7 m and a diameter of 2.3 m is the innermost part of the ATLAS detector, covering pseudorapidity⁴ up to $|\eta| \leq 2.5$. The entire tracker is contained within a 2T solenoidal magnet. Since the magnetic field is directed along the beam axis, the paths of charged particle bend according to their transverse momentum. It is able to reconstruct tracks of above a p_T threshold of 100 MeV. The Inner detector consist of three independent and complementary subsystems. These are, from the innermost layer out:

- The pixel detector - a high granularity silicon detector. The pixel detector consists of 3 layers in the barrel region and 5 disks in both end-cap regions. The detector part closest to the interaction point is the B-layer at a radius of ≈ 5 cm. Precise measurements of the tracks at this region allows for the measurement of impact parameters, and therefore for the reconstruction of secondary vertices.
- The semiconductor tracker (SCT) - a precision silicon microstrip detector. Although the SCT has the same underlying technology as the pixel detector, it is designed to be optimized to the decreased track density at larger radii.
- Transition radiation tracker (TRT) - The TRT is a drift tube system with a Xenon gas-mixture⁵. Transition radiation photons that are produced when ultra-relativistic charged particles cross a boundary between materials with different dielectric constants are absorbed by the Xenon gas and yield a typically larger signal than a charged particle. By supporting two different thresholds, the readout electronic can distinguish between both signals. Therefore, it contributes to the track reconstruction as well as to the electron identification.

⁴Pseudorapidity is a spatial coordinate describing the angle of a particle relative to the beam axis. It is defined as $\eta = -\ln \left[\tan \frac{\theta}{2} \right]$.

⁵Xe(70%)CO₂(27%)O₂(3%)

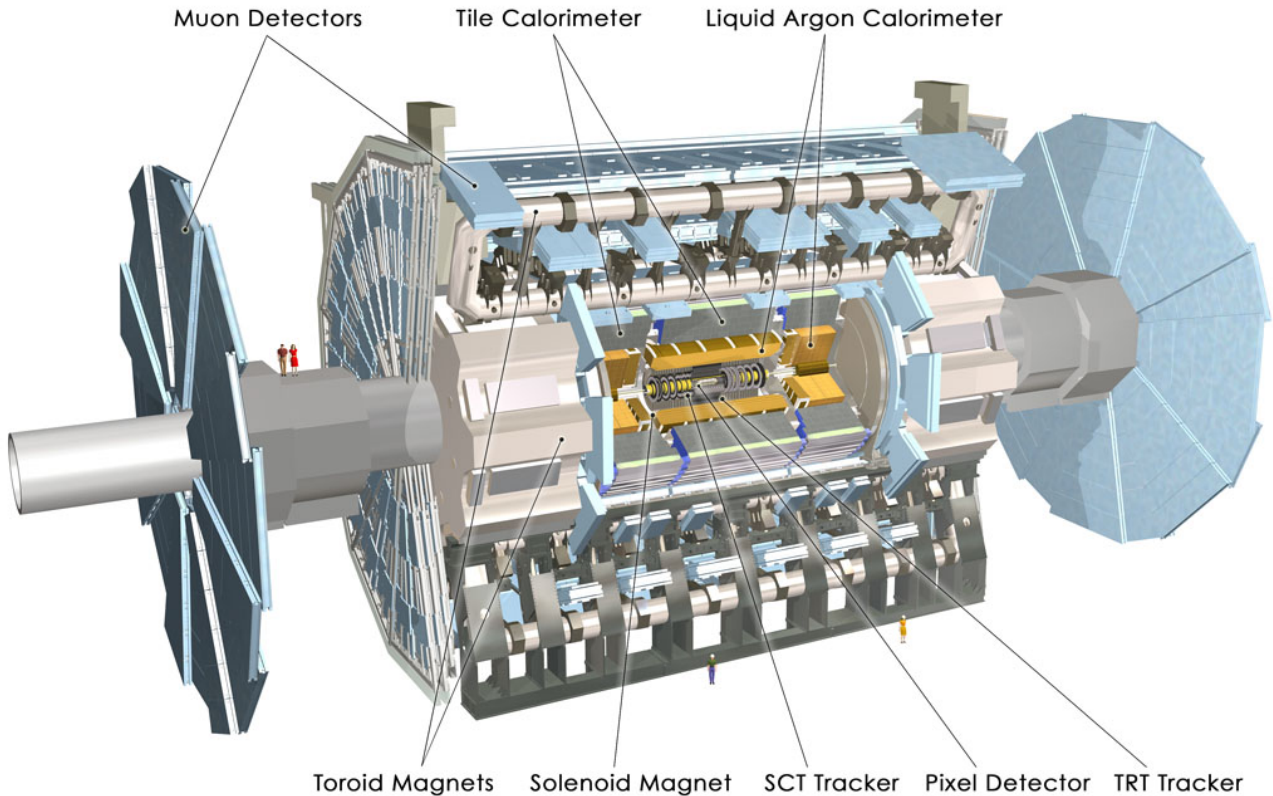


Figure 2.2.2: The ATLAS detector [57]. The dimensions of the detector are 25 m in height and 46 m in length. The overall weight of the detector is approximately 7000 tonnes.

The Calorimeters The calorimeters are designed to provide an accurate energy measurement of electrons, photons and jets (hadrons). There are two types of calorimeters:

- The Electromagnetic calorimeter (ECAL) - an accordion shaped sampling geometry with lead as an absorber and liquid argon as a sensitive component that is used to detect electromagnetically interacting particles.
- The Hadronic calorimeter (HCAL) - detects high energy hadrons. The hadron calorimeter absorbs energy from particles that pass through the EM calorimeter, but do interact via the strong force. In the region $\eta < 1.7$, which comprises the barrel and extended barrel components, a sampling concept with steel as absorber and scintillating tiles as active medium is used. The hadronic end-cap (HEC) and the forward calorimeter (FCAL), covering the range of $1.5 < \eta < 3.2$ and $3.1 < \eta < 4.9$ respectively, suffer from a much higher radiation flux. Therefore, the intrinsically radiation hard liquid argon (LAr) technology is employed. An important aspect in the design of the hadronic calorimetry is a sufficiently large thickness (10 interaction length λ) to minimize the punch-through of high energetic particles into the muon system.

The Muon spectrometer Whereas electrons, photons and hadrons are absorbed by the calorimetry system, muons with a $p_T > 3$ GeV can penetrate the detector and reach the muon spectrometer. A large magnetic system is used (with an average magnetic field strength of 0.6 Tesla) in order to measure the momentum of the muons with high accuracy.

2.3 Standard model of particle physics

2.3.1 Overview

The Standard Model describes particle interactions as a result of local gauge symmetries [58]. It incorporates three of the four known fundamental forces: the electromagnetic force, the strong force and the weak force⁶. The Standard Model gauge theory is based on the symmetry group

$$G_{SM} = SU(3)_c \otimes SU(2)_L \otimes U(1)_Y \quad (2.3.1)$$

Gluons, the gauge bosons of quantum chromodynamics $SU(3)_c$, mediate the strong interactions at the fundamental level. The $SU(2)_L \otimes U(1)_Y$ part is called the *ElectroWeak theory* (EW), and is spontaneously broken (we will review the EW theory below). Gauge bosons are outlined in Table 2.1.

Table 2.1: Gauge bosons in the Standard Model [59]

boson	mass	electric charge	symmetry group
g	0 eV (theoretical value)	0	$SU(3)_c$
γ	$< 10^{-18}$ eV	0	$SU(2)_L \otimes U(1)_Y$
Z	91.1876 GeV	0	$SU(2)_L \otimes U(1)_Y$
W^\pm	80.399 GeV	± 1	$SU(2)_L \otimes U(1)_Y$

The particles in the Standard Model can be categorized according to their spin: There are *fermions* with half-integer spin, and *bosons* with integer spin. Fermions are further divided into *leptons* which do not interact via the strong force and *quarks* which undergo strong interactions. Furthermore, the fermions come in three different generations which behave identically under the symmetry transformation explained below and differs only in the masses of the contained particles.

There are always two different pairs of leptons and quarks per generation which yields in total 12 fermions as shown in Table 2.2.

Table 2.2: Fermionic particle content of the Standard Model [59]

type	first generation		second generation		third generation	
	flavor	mass	flavor	mass	flavor	mass
leptons	ν_e	< 2 eV	ν_μ	< 2 eV	ν_τ	< 2 eV
	e	511 keV	μ	105.658 MeV	τ	1776.82 MeV
quarks	u	1.7-3.1 MeV	c	1.29 GeV	t	172.9 GeV
	d	4.1-5.7 MeV	s	100 MeV	b	4.19 GeV

In the next sections the electroweak (EW) sector of the SM and the Higgs mechanism are discussed in more detail.

2.3.2 Electroweak Gauge Theory

In Standard model the electroweak interactions is based on gauge group $SU(2)_L \times U(1)_Y$, with gauge bosons W_μ^i , $i = 1, 2, 3$, and B_μ for the $SU(2)_L$ and $U(1)_Y$ respectively, and the

⁶Gravity is too weak at the scales with which particle physics is concerned and is not incorporated in the Standard Model.

corresponding gauge coupling constants g and g' . The EW Lagrangian is shown in eq. 2.3.2.

$$\mathcal{L}_{EW} = \sum_i i\bar{\psi}_i \gamma^\mu D_\mu \psi_i \quad (2.3.2)$$

where the covariant derivative for this particular symmetry group is given as:

$$D_\mu = \partial_\mu + ig'YB_\mu + ig\frac{1}{2}\vec{\tau}_L \cdot \vec{W}_\mu \quad (2.3.3)$$

with $\vec{\tau}$ are the *Pauli matrices* - generators of the $SU(2)_L$ group and Y is the *weak hypercharge* - the generator of the $U(1)_Y$ group.

The particles within the EW theory are required to be massless. Unfortunately, this contradicts the experimental observation that shows the the fermions and gauge bosons posses a mass. Therefore, a mechanism is needed to describe massive fields and introduce mass terms in a way that is compatible with the requirement of local gauge invariance.

2.3.3 Higgs mechanism and the EW symmetry braking

The Higgs⁷ mechanism [60] postulates an additional isospin doublet Φ of a complex scalar fields with the potential:

$$V(\Phi) = -\mu^2\Phi^\dagger\Phi + \lambda(\Phi^\dagger\Phi)^2 \quad \text{where } \mu^2, \lambda > 0 \quad (2.3.4)$$

Then The Lagrangian for the Higgs sector is given by:

$$\mathcal{L}_{Higgs} = (D^\mu\Phi)^\dagger(D_\mu\Phi) - V(\Phi) \quad (2.3.5)$$

which is invariant under $SU(2)_L \times U(1)_Y$ transformations. Higgs doublet has the form:

$$\Phi = \begin{pmatrix} \phi^+ \\ \phi^0 \end{pmatrix} \quad (2.3.6)$$

For $\mu^2 > 0$, the potential $V(\Phi)$ has infinite degenerate minima corresponding to

$$\Phi^\dagger\Phi = -\frac{\mu^2}{2\lambda} = \frac{v^2}{2} \quad (2.3.7)$$

One can choose a particular direction for the minimum of Φ . Since no positive charged permanent background field is observed, the ground state must take the form:

$$\Phi_0 = \langle 0|\Phi|0\rangle = \begin{pmatrix} 0 \\ \frac{v}{\sqrt{2}} \end{pmatrix} \quad (2.3.8)$$

The vacuum has zero eigenvalue for the electric charge operator $Q\Phi_0 = 0$ and is, therefore invariant under the $U(1)_{EM}$.

$U(1)_{EM}$ remains unbroken, and in this broken phase, we customarily choose Φ to be represented by :

$$\Phi = \begin{pmatrix} 0 \\ \frac{v+h(x)}{\sqrt{2}} \end{pmatrix} \quad (2.3.9)$$

where $h(x)$ is the massive spin 0 field which is called *Higgs boson*.

In equation 2.3.5 the covariant derivative for Higgs field in it ground state is given by:

$$(D^\mu\Phi)^\dagger(D_\mu\Phi) = \left| \frac{1}{2} \begin{pmatrix} gW_3^\mu + g'B^\mu & g(W_1^\mu - iW_2^\mu) \\ g(W_1^\mu - iW_2^\mu) & -gW_3^\mu + g'B^\mu \end{pmatrix} \begin{pmatrix} 0 \\ \frac{v+h}{\sqrt{2}} \end{pmatrix} \right|^2 \quad (2.3.10)$$

⁷Named after Peter W. Higgs

defining the new fields:

$$\begin{aligned} W_{\pm}^{\mu} &= \frac{1}{\sqrt{2}}(W_1^{\mu} \mp iW_2^{\mu}) \\ \tan \theta_W &= \frac{g'}{g} \\ \begin{pmatrix} Z^{\mu} \\ A^{\mu} \end{pmatrix} &= \begin{pmatrix} \cos \theta_W & \sin \theta_W \\ -\sin \theta_W & \cos \theta_W \end{pmatrix} \begin{pmatrix} B^{\mu} \\ W_3^{\mu} \end{pmatrix} \end{aligned} \quad (2.3.11)$$

equation 2.3.10 yields:

$$(D^{\mu}\Phi)^{\dagger}(D_{\mu}\Phi) = \frac{g^2v^2}{4} \left[W_+^{\mu}W_{-\mu} + \frac{1}{\cos^2\theta_W} Z^{\mu}Z_{\mu} \right] \left(1 + \frac{h}{v} \right)^2 + \frac{1}{2}(\partial^{\mu}h)(\partial_{\mu}h) \quad (2.3.12)$$

from which one can identify the gauge boson masses

$$\begin{aligned} M_W^2 &= \frac{1}{4}g^2v^2 \\ M_Z^2 &= \frac{1}{4}(g^2 + g'^2)v^2 = \frac{g^2v^2}{4\cos^2\theta_W} \\ M_A^2 &= 0 \end{aligned} \quad (2.3.13)$$

Expanding the term for the Higgs potential, the mass of the Higgs boson at tree level is found to be

$$M_H = \sqrt{2\lambda}v \quad (2.3.14)$$

After spontaneous symmetry breaking the Lagrangian for the fermion fields, ψ_i , is:

$$\begin{aligned} \mathcal{L}_F &= \sum_i \bar{\psi}_i \left(i\gamma^{\mu}\partial - m_i - \frac{gm_iH}{2M_W} \right) \psi_i \\ &- \frac{g}{2\sqrt{2}} \sum_i \bar{\Psi}_i \gamma^{\mu} (1 - \gamma^5) (T^+ W_{\mu}^+ + T^- W_{\mu}^-) \Psi_i \\ &- e \sum_i q_i \bar{\psi}_i \gamma^{\mu} \psi_i A_{\mu} \\ &- \frac{g}{2\cos\theta_W} \sum_i \bar{\psi}_i \gamma^{\mu} (g_V^i - g_A^i \gamma^5) \psi_i Z_{\mu} \end{aligned} \quad (2.3.15)$$

where $e = g \sin \theta_W$ which is the positron electric charge. T^+ and T^- are the weak isospin raising and lowering operators. The vector and axial-vector couplings are

$$g_V^i = t_{3L}(i) - 2q_i \sin^2 \theta_W \quad (2.3.16)$$

$$g_A^i = t_{3L}(i) \quad (2.3.17)$$

where $t_{3L}(i)$ is the weak isospin of fermion i ($+1/2$ for u_i and ν_i ; $-1/2$ for d_i and e_i) and q_i is the charge of ψ_i in units of e .

The vacuum expectation value (VEV) constrained to $v = \frac{\mu}{\sqrt{\lambda}} = (\sqrt{2}G_F)^{-1/2} \approx 246$ GeV, where $G_F = 1.167 \times 10^{-5} GeV^{-2}$ is the fermi constant. The fact that the ground state does not exhibit the full symmetry of the Lagrangian in 2.3.5 is called *Spontaneous Symmetry Breaking (SSB)*.

2.3.4 Fermion mass

The fermion mass terms cannot be added by hand in the Standard Model Lagrangian. These mass terms of the form $-m\bar{\phi}\phi$ would not be local gauge invariant. However, by using the Higgs field that we introduced before, we can construct a Yukawa interaction term that does remain gauge invariant under local $SU(2)_L \times U(1)_Y$ transformations. The corresponding part for the i^{th} fermion generation is⁸:

$$\mathcal{L}_{Yukawa} = \lambda_{e_i} \bar{L}^i \Psi e_R^i + \lambda_{d_i} \bar{Q}^i \Psi d_R^i + \lambda_{u_i} \bar{Q}^i \Psi^C u_R^i + \text{h.c.} \quad (2.3.18)$$

⁸ $\Psi^C = i\sigma^2\Psi$

The fermion masses are given by $M_f = \lambda_f \frac{v}{\sqrt{2}}$ and the coupling to Higgs field is proportional to fermion masses:

$$g_{Hff} = \frac{m_f}{v} \quad (2.3.19)$$

2.4 Higgs $\rightarrow \tau\tau \rightarrow e\mu + 4\nu$ decay channel analysis

2.4.1 Higgs production

At the LHC, the Higgs boson can be mainly produced through the following four main mechanisms: gluon fusion through a heavy quark triangular loop (ggH), vector boson fusion (VBF), associated production with vector bosons W or Z (VH), and production in association with a top-quark pair. The production diagrams are shown in Figure 2.4.1, and the production cross

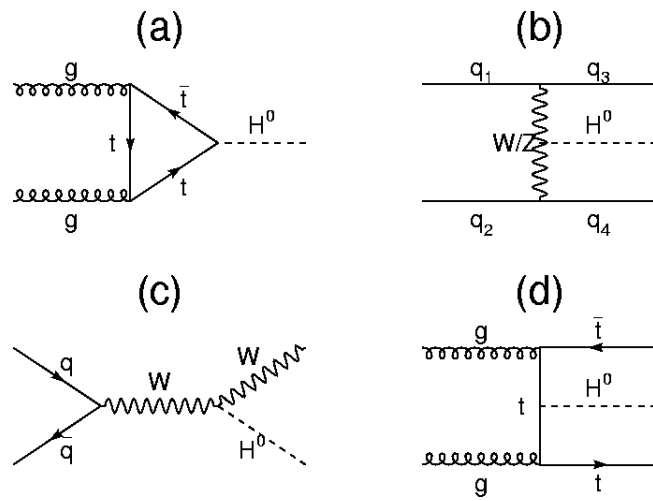


Figure 2.4.1: Higgs production at hadron colliders: (a) Gluon fusion through a heavy quark triangular loop, (b) Vector boson fusion, (c) Associative production with W, (d) Production in association with a top-quark pair.

section are shown in Figure 2.4.2.

The decay of the neutral Higgs bosons into a pair of τ leptons is a promising channel for the SM Higgs boson searches at the LHC [61, 62, 63]. This is because it has a discriminating

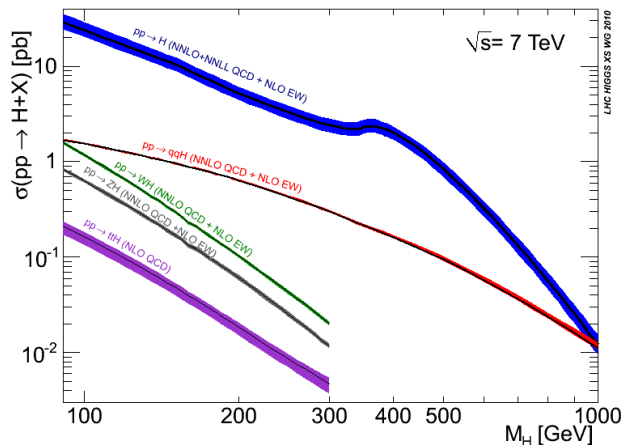


Figure 2.4.2: Standard Model Higgs boson production cross sections [50].

features over the background that compensate its low branching ratio of 7% in the Higgs boson mass range of 110-140 GeV,

The sensitivity is enhanced by the requirement that the Higgs boson be produced in association with jets. This can occur at the associative production with a vector boson (Higgsstrahlung), from the gluon fusion associated with initial radiation and at the leading order in the Vector Boson Fusion (VBF) process. The selected events are divided into four exclusive categories depending on the jet multiplicity of the event and the jet kinematics.

2.4.2 Background

The main background to the Higgs boson signal is the largely irreducible $Z/\gamma^* \rightarrow \tau\tau$ process. It is particularly important for low Higgs boson masses where the signal falls on the tail of the Z mass peak in the $\tau\tau$ mass distribution.

W+jets production provides a source of background due to its relatively large cross-section and the combination of a charged lepton and missing transverse energy from the leptonic decay of the W boson in the final state. Hadronic jets accompanying the W boson can be misidentified as an electron or a semi-leptonic decay in the cascade, and can give off a signature similar to that of an isolated lepton.

The electroweak production of pairs of vector bosons (WW, WZ, ZZ) can lead to final states with two or more charged leptons from the leptonic decays of the W and Z bosons.

Due to the decays of the two top-quarks ($t\bar{t} \rightarrow W^+bW^-\bar{b}$), this process can lead to final states with two leptons and missing transverse energy, when the W bosons decay leptonically.

The production of single top-quarks via t or s-channel production or in association with a W boson contributes to the background if one W boson decays leptonically and one of the leptons is either due to a misidentified hadronic jet or, for Wt production, comes from the decay of the second W boson.

The cross-sections for the above processes are summarized in Table 2.3.

Table 2.3: Cross-sections for various background channels. Relevant branching ratios (BR) are taken into account, as written in the table. From ref. [64]

Process	$\sigma \times \text{BR}$ (pb)
$Z/\gamma^* \rightarrow ll + \text{jets}$ ($l = e, \mu$ or τ)	15×10^3
$W \rightarrow l\nu + \text{jets}$ ($l = e, \mu$ or τ)	31.5×10^3
$WW, WZ, ZZ(66\text{GeV} < M_Z < 116\text{GeV})$	44.9, 18.0, 5.6
$t\bar{t}$	167
Single top quark t,s and Wt -channels	64.6, 4.6, 15.7
SM $gg \rightarrow H(\rightarrow \tau\tau)$, $m_H = 120$ GeV	1.18
SM VBF $H(\rightarrow \tau\tau)$, $m_H = 120$ GeV	9.0×10^{-2}
SM $WH(\rightarrow \tau\tau)$, $m_H = 120$ GeV	4.7×10^{-2}
SM $ZH(\rightarrow \tau\tau)$, $m_H = 120$ GeV	2.6×10^{-2}

2.4.3 Object reconstruction

The topology of the final states in this analysis requires the reconstruction of electrons, muons, jets and missing transverse energy, E_T^{miss} .

Electrons: The electron candidates are formed from an energy deposit in the ECAL and linked to a track measured in the inner detector. They are selected if they have a transverse energy $E_T > 15\text{GeV}$, lie within $|\eta| < 2.47$, but are outside of the transition region between the barrel and end-cap calorimeters ($1.37 < |\eta| < 1.52$) and meet quality requirements based on the expected shower shape [65].

Muons: Muon candidates are formed from a track measured in the inner detector and linked to a track in the muon spectrometer [66]. The muons used in this analysis are required to have $p_T > 10\text{GeV}$ and to lie within $|\eta| < 2.5$. Additionally, the difference between the z position of the point of closest approach of the muon inner detector track to the beam-line and the z coordinate of the primary vertex⁹ is required to be less than 1 cm. This requirement reduces the contamination due to cosmics and beam-induced backgrounds. Finally, inner detector track quality criteria are applied in order to achieve a precise measurement of the muon momentum and reduce the misidentification rate.

Both electrons and muons are required to be isolated: the additional transverse energy in the ECAL and HCAL in a cone of radius $\Delta R = \sqrt{(\Delta\eta)^2 + (\Delta\phi)^2} = 0.2$ around the electron (muon) direction must be less than 8% (4%) of the electron transverse energy (muon transverse momentum). The sum of the transverse momenta of all tracks located within a cone of radius $\Delta R = 0.4$ around the electron (muon) direction and with p_T above 1 GeV must be less than 6% of the electron transverse energy (muon transverse momentum).

Jets: Jets are reconstructed using the anti- k_t algorithm [67] with a distance parameter $R = 0.4$, taking as input three-dimensional clusters in the calorimeters. Reconstructed jets with $E_T > 20\text{GeV}$ and within $|\eta| < 4.5$ are selected. Events are discarded if a jet is identified as out-of-time activity or calorimeter noise.

Missing transverse energy: The E_T^{miss} reconstruction is based on the cluster weighting calibration scheme used in the jet definition and described in [68] and it relies on energy deposits in the calorimeter in the region $|\eta| < 4.5$ and on reconstructed muons.

Overlap removal: When candidates fulfilling the above criteria overlap with each other geometrically (within $\Delta R < 0.2$), only one of them is selected. The overlap is resolved by selecting muon, electron and jet candidates in descending order of priority.

2.4.4 Event selection

Preselection The following event selection requirements using the physics objects defined in Section 2.4.3. Signal events are selected by requiring exactly two isolated and oppositely charged one electron and one muon. Single lepton and di-lepton triggers are used to preselect the data. The single muon trigger requires the p_T to exceed 18 GeV; for the single electron trigger the E_T threshold varies from 20 to 22 GeV depending on the LHC instantaneous luminosity; the $e\mu$ trigger requires $E_T > 10$ GeV for the electron and $p_T > 6$ GeV for the muon. Additionally, $E_T > 22$ GeV is required if the electron satisfies the single electron trigger. The ET requirement is increased to 24 GeV when the trigger threshold is 22 GeV. If a muon is associated with the single muon trigger object, it is required to have $p_T > 20$ GeV. The di-lepton invariant mass is required to be in the range of $30\text{ GeV} < m_{\ell\ell} < 100\text{ GeV}$.

⁹The primary vertex is defined as the vertex with the largest $\sum p_T$ of the associated tracks.

Analysis categories The selected event samples are split into several categories according to the number of reconstructed jets in the event: 2-jet VBF, 2-jet VH, 1-jet and 0 jet. For these categories additional selection requirements are applied as well.

The first two categories require the presence of 2 jets and the cuts are optimized for the VBF process [61, 62] in one case and VH and $gg \rightarrow H$ in the other case. The 1-jet category requires the presence of at least one high- E_T jet and the main production mechanism is the $gg \rightarrow H$ plus high p_T parton [63]. The 0-jet category uses an inclusive selection to collect the signal event topologies not selected by the other categories. All categories are defined in such a way that events cannot belong to more than one of them.

In the 0 jet category, in order to suppress the $t\bar{t}$ background, it is required that the di-lepton azimuthal opening angle be $\Delta\phi > 2.5$ rad. and $H_T^{lep} = p_T(lep1) + p_T(lep2) + E_T^{miss} < 120 GeV$, where $p_T(lep1)$ and $p_T(lep2)$ are the transverse momenta of the leptons.

In the categories with jets, the presence of a hadronic jet with a transverse energy $E_T > 40$ GeV is required. In addition, $E_T^{miss} > 20 GeV$ is also required.

The collinear approximation [69], which is derived in sec. 2.5.3, is used to reconstruct the kinematics of the $\tau\tau$ system in the categories with jets. It is required that $0.1 < x_1, x_2 < 1.0$, where x_i are defined in eq. 2.5.6. It is additionally required that $0.5 \text{ rad} < \Delta\phi < 2.5 \text{ rad}$ to suppress $Z/\gamma^* \rightarrow ee, \mu\mu$ backgrounds, and that no b-jets with $E_T > 25$ GeV are found in the event to suppress the top backgrounds.

For the 2-jet categories, an additional jet with $E_T > 25$ GeV is required. For the 2-jet VBF category, a pseudorapidity difference between the selected jets of $|\eta| > 3.0$ and a di-jet invariant mass of $m_{jj} > 350 GeV$ are required to reject the $t\bar{t}$ background. Finally, the event is rejected if any additional jet with $E_T > 25$ GeV and $|\eta| < 2.4$ is found in the pseudorapidity range between the two leading jets. For the 2-jet VH category, the requirement on the jets pseudorapidity separation and the di-jet invariant mass are instead: $\Delta\eta_{jj} < 2.0$ and $50 \text{ GeV} < m_{jj} < 120 \text{ GeV}$.

Only events failing the cuts for the 2-jet categories are considered in the 1-jet category. In addition, it is required that the invariant mass of the two τ leptons and the leading jet fulfill $m_{\tau\tau j} > 225 GeV$, where the τ momenta are taken from the collinear approximation.

2.5 Mass reconstruction algorithms in $H \rightarrow \tau\tau$ searches

2.5.1 Visible mass

The visible mass is defined as the invariant mass of the visible tau lepton decay products:

$$M_{vis} = |P_{vis1} + P_{vis2}| \quad (2.5.1)$$

where P_{vis} is the visible tau decay products 4-momenta. The advantage of this simple definition is that it allows a precise reconstruction of both lepton four-vectors (see for example Fig.2.5.4a). However, the visible mass provides no direct link to the invariant mass of the resonance as the contributions of the neutrino momenta are ignored.

2.5.2 Effective mass

From the missing energy measurement we can have the x and y components of the neutrinos 4-momenta. The missing energy is defined by $\cancel{E}_{T_i} = -\sum_j E_{T_i}^j$ for $i \in \{x, y\}$. The effective mass incorporates information from the \cancel{E}_T measurement. It is defined as:

$$M_{eff} = \sqrt{\left(P_{vis1} + P_{vis2} + P_{\cancel{E}_T}\right)^2} \quad (2.5.2)$$

where $P_{\cancel{E}_T} = (\cancel{E}_T, \cancel{E}_{T,X}, \cancel{E}_{T,Y}, 0)$.

Effective mass produce somehow better separation than the visible mass. However, it can only provide an approximation since the \cancel{E}_T measurement contains only the transverse neutrino momenta. Hence it neglects the invariant mass of the 4 neutrino system, which might have a large mass - of order of the visible mass. This problem is particularly prominent in the low-mass $H \rightarrow \tau\tau$ search, where the signal cannot be separated from the much larger and very broad $Z \rightarrow \tau\tau$ background. Distributions of the Effective and Visible mass variables are shown in Figure 2.5.1.

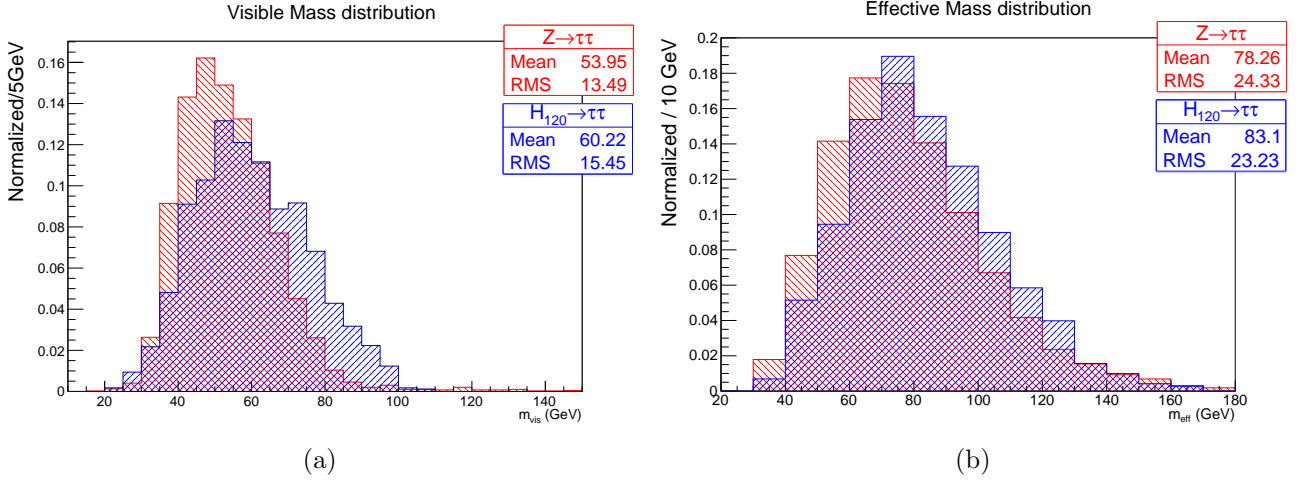


Figure 2.5.1: Normalized Distribution for 120 GeV SM Higgs mass and Z mass (which is the dominant background). The events are based on preselection cuts: (a) Visible and (b) Effective mass.

2.5.3 Collinear approximation

The collinear approximation first proposed in ref. [69] to reconstruct invariant mass in $\tau\tau$ decays of a Higgs boson when produced in association with an energetic jet. The tau leptons that are created are highly boosted (for higgs of 125GeV the tau leptons have $\gamma_\tau \approx 35$), thus we can assume that the decay direction of the invisible and visible τ -decay products is collinear ($\vec{p}_{miss} \parallel \vec{p}_{vis}$). Once we know the angles of the invisible decay products we can calculate the invisible momenta from the missing energy:

$$\begin{aligned} \cancel{E}_{TX} &= |p_{miss1}| \sin \theta_{vis1} \cos \varphi_{vis1} + |p_{miss2}| \sin \theta_{vis2} \cos \varphi_{vis2} \\ \cancel{E}_{TY} &= |p_{miss1}| \sin \theta_{vis1} \sin \varphi_{vis1} + |p_{miss2}| \sin \theta_{vis2} \sin \varphi_{vis2} \end{aligned} \quad (2.5.3)$$

or

$$\begin{aligned} |p_{miss1}| &= \frac{\cancel{E}_{TX} \sin \varphi_{vis2} - \cancel{E}_{TY} \cos \varphi_{vis2}}{\sin \theta_{vis1} \sin(\varphi_{vis2} - \varphi_{vis1})} \\ |p_{miss2}| &= \frac{\cancel{E}_{TX} \sin \varphi_{vis1} - \cancel{E}_{TY} \cos \varphi_{vis1}}{\sin \theta_{vis2} \sin(\varphi_{vis1} - \varphi_{vis2})} \end{aligned} \quad (2.5.4)$$

where θ_{vis_i} and φ_{vis_i} is the polar and azimuthal angles of the visible products of each τ decay.

Within the collinear approximation one can introduce the fractions $x_{1,2}$ of the tau lepton momenta carried by the visible τ -decay products:

$$\vec{p}_{vis,i} = x_i \vec{p}_{\tau,i} \quad (2.5.5)$$

where

$$x_i = \frac{|p_{vis,i}|}{|p_{vis,i}| + |p_{miss,i}|} \quad (2.5.6)$$

now neglecting the τ mass and using the collinear approximation, the invariant mass of the $\tau\tau$ system can be written as:

$$M_{col} = \frac{M_{vis}}{\sqrt{x_1 x_2}} \quad (2.5.7)$$

where M_{vis} is the visible mass (Eq. 2.5.1).

Despite offering the great advantage of fully reconstructed $\tau\tau$ mass instead of a partial mass, the collinear approximation still has significant shortcomings. The collinear mass gives reasonable mass resolution only for a small fraction of events where the $\tau\tau$ system is boosted in the transverse plane (i.e. in association with a large E_T jet). Otherwise, the visible τ decay products produced back-to-back in the plane transverse to the beam line; the solution of equations 2.5.3 becomes degenerate and diverge at $|\varphi_{vis_2} - \varphi_{vis_1}| \rightarrow \pi$ ($M_{col} \propto \frac{1}{\sin(\varphi_{vis_2} - \varphi_{vis_1})}$), when the missing energy is not collinear with the tau visible decay products ($\tan \phi_{vis} \neq \left| \frac{E_Y}{E_X} \right|$), and the collinear method fails.

Moreover the systematic sensitivity to missing energy measurement is much larger for back to back events:

$$\frac{\partial M_{Coll}}{\partial E_\xi} = \frac{1}{2} M_{Coll} \cdot \left(\frac{\partial}{\partial E_\xi} \log \prod_{i=1}^2 (|p_{vis,i}| + |p_{miss,i}|) \right) \propto \frac{1}{\sin(\varphi_{vis_2} - \varphi_{vis_1})} \quad (2.5.8)$$

The divergence at the limit of $|\varphi_{vis_2} - \varphi_{vis_1}| \rightarrow \pi$ indicates high sensitivity to the mis-measurements of missing energy. An example of the different ranges of $\Delta\phi$ is shown in figure 2.5.2.

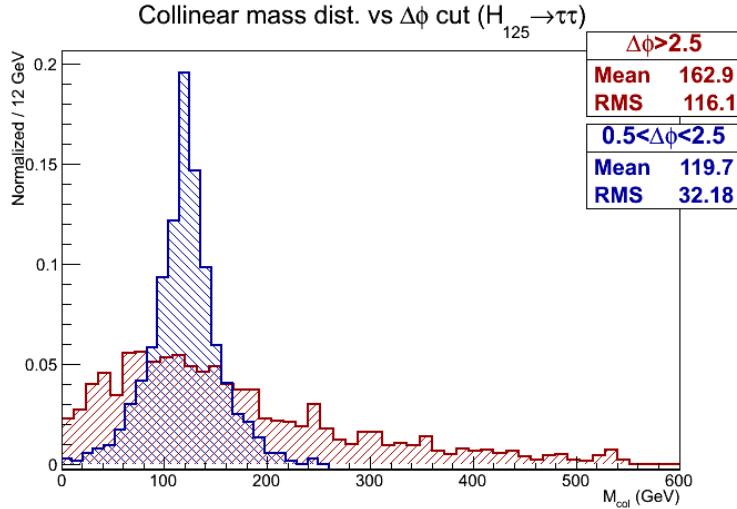


Figure 2.5.2: Collinear mass distribution for ggH 125 GeV Higgs boson mass reconstruction with $\Delta\phi > 2.5$ and $0.5 > \Delta\phi < 2.5$ using preselection cuts.

For $\Delta\phi > 2.5$ the collinear approximation is not valid, and we have a high spread of reconstructed mass.

2.5.4 MMC algorithm

The Missing Mass calculator (MMC) was suggested by A. Pranko et.al [54] (in the present work we will call it as the *old algorithm*) as a tool of mass reconstruction in di-tau resonances. The MMC algorithm's main propose is to provide an accurate mass reconstruction, and do not suffer from the limitation of the collinear approximation as described in the previous section (2.5.3). The major improvement offered by the algorithm is its high reconstruction efficiency. The collinear cut in multijet analysis cuts on $\approx 55\%$ of the VBF signal. In addition it has a better mass reconstruction. The mass reconstruction is also important when we want to separate the Higgs signal from the background.

Ideal detector resolution: For an ideal detector resolution (meaning that all physical quantities are measured with perfect precision), di-tau 4-vector contains 16 variables: 2 leptons 4-vectors ($P_{vis1,2}$) and 2 missing vectors ($P_{miss1,2}$). Each missing vector consists of 2 neutrinos in the leptonic τ decay channel and one neutrino in hadronic τ decay. Although the neutrinos remain unmeasured, one can still extract a part of the unmeasured quantities. By assuming that the neutrinos come from the resonance decay, the missing energy - \cancel{E}_T can be expressed in terms of invisible momenta:

$$\begin{aligned}\cancel{E}_{Tx} &= P_{X,miss1} + P_{X,miss2} \\ &= P_{miss1} \sin \theta_{miss1} \cos \varphi_{miss1} + P_{miss2} \sin \theta_{miss2} \cos \varphi_{miss2} \\ \cancel{E}_{Ty} &= P_{Y,miss1} + P_{Y,miss2} \\ &= P_{miss1} \sin \theta_{miss1} \sin \varphi_{miss1} + P_{miss2} \sin \theta_{miss2} \sin \varphi_{miss2}\end{aligned}\tag{2.5.9}$$

where \cancel{E}_{Tx} and \cancel{E}_{Ty} are the x- and y-components of the $\vec{\cancel{E}}_T$ vector, $P_{miss1,2}, \theta_{miss1,2}$ and $\varphi_{miss1,2}$ are the momenta, polar and azimuthal angles of the di- ν system.

Additional known parameter are the τ mass. Thus, two additional constraints can be used:

$$\begin{aligned}M_{\tau_1} &= m_{vis1}^2 + m_{miss1}^2 + 2E_{vis1}E_{miss1} - 2\vec{P}_{vis1} \cdot \vec{P}_{miss1} \\ M_{\tau_2} &= m_{vis2}^2 + m_{miss2}^2 + 2E_{vis2}E_{miss2} - 2\vec{P}_{vis2} \cdot \vec{P}_{miss2}\end{aligned}\tag{2.5.10}$$

where m , E and \vec{P} is the mass, energy and momenta respectively, *vis* and *miss* indexes indicate the visible and invisible ("missing") τ decay products¹⁰.

For hadronic τ decay we have still 2 unknown variables while for leptonic τ decay we have 4, therefore the available information is insufficient for finding the exact solution. However, not all solutions are equally likely, and additional knowledge of τ decay kinematics can be used to distinguish more likely solutions from less likely ones. From τ decay kinematics, one can extract distribution of the $\Delta R = \sqrt{(\eta_{miss} - \eta_{vis})^2 + (\varphi_{miss} - \varphi_{vis})^2}$. This distribution is obtained from the Monte Carlo (MC) simulation, and is parametrized with a linear combination of Gaussian and Landau functions as a function of τ momenta. An example of such fit is shown in figure 2.5.3. The \mathbf{p}_τ -dependence of the mean, width and relative normalization of the Gaussian and Landau is parametrized as $a_0/(p_\tau + a_1 p_\tau^2) + a_2 + a_3 p_\tau + a_4 p_\tau^2$ (where a_i are the coefficients of the parametrization).

This additional knowledge of the decay kinematics defines probability density functions for the additional parameters ($\mathcal{P}(\Delta R_1, \mathbf{p}_{\tau,1}) \times \mathcal{P}(\Delta R_2, \mathbf{p}_{\tau,2})$). In pure leptonic tau decay, with 2 more unknowns, additional probability density functions may be derived as a function of di-neutrino mass (m_{miss}). This yields a 4-dimensional probability density function: $\prod_{i=1,2} \mathcal{P}(\Delta R_i, \mathbf{p}_{\tau,i}) \times \mathcal{P}(m_{miss,i})$.

¹⁰For hadronic τ decays $m_{miss} = 0$ as there is only one neutrino involved, while for leptonic τ decays di-neutrino system has non-zero mass

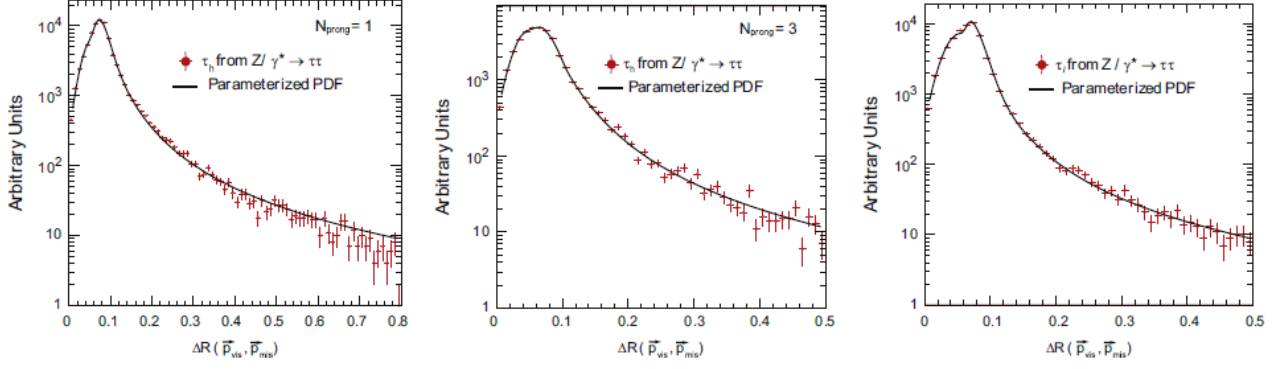


Figure 2.5.3: An example of the probability distribution functions $\mathcal{P}(\Delta R, \mathbf{p}_\tau)$ for a particular value of the original τ lepton momentum \mathbf{p}_τ . These functions are used in the calculation of the global event probability for three cases: 1-prong (left plot), 3-prong (middle plot), and leptonic decays (right plot) of τ leptons. From ref. [54].

For the lep-lep channel, the old algorithm creates 4-dimensional grid $[\varphi_{miss_1}, \varphi_{miss_2}, m_{miss_1}, m_{miss_2}]$. For each grid point the solution for the unknown parameters can be obtained. From Eq.2.5.9 one obtains:

$$P_{T,miss_1} = \frac{\cancel{E}_{TX} \sin(\varphi_{miss_2}) - \cancel{E}_{TY} \cos(\varphi_{miss_2})}{\sin(\varphi_{miss_2} - \varphi_{miss_1})} \quad (2.5.11)$$

$$P_{T,miss_2} = \frac{\cancel{E}_{TX} \sin(\varphi_{miss_1}) - \cancel{E}_{TY} \cos(\varphi_{miss_1})}{\sin(\varphi_{miss_1} - \varphi_{miss_2})}$$

and from eq.2.5.10, one obtains:

$$P_{Z,miss_i}^\pm = \frac{\alpha_i \cdot P_{Z,vis_i} \pm E_{vis_i} \sqrt{\alpha_i^2 - (E_{vis_i}^2 - P_{Z,vis_i}^2)(P_{T,miss_i}^2 + m_{miss_i}^2)}}{E_{vis_i}^2 - P_{Z,vis_i}^2} \quad i \in \{1, 2\} \quad (2.5.12)$$

where $\alpha_i = \frac{1}{2}(M_\tau^2 - m_{miss_i}^2 - m_{vis_i}^2) + \vec{\mathbf{P}}_{T,vis_i} \cdot \vec{\mathbf{P}}_{T,miss_i}$

Now using the 4-vectors for both di-neutrino systems, mass of the resonance can be calculated from $M_{\tau\tau} = \sqrt{(\mathbf{P}_{vis_1} + \mathbf{P}_{vis_2} + \mathbf{P}_{miss_1} + \mathbf{P}_{miss_2})^2}$.

For each grid point ΔR , m_{miss} and \mathbf{p}_τ can be calculated, and the estimated mass will be weighted by the global event probability which is defined by:

$$\mathcal{P}_{event} = \prod_{i=1}^2 \mathcal{P}(\Delta R_i, \mathbf{p}_{\tau_i}) \times \mathcal{P}(m_{miss,i}) \quad (2.5.13)$$

For all grid point $M_{\tau\tau}$ distribution is produced, and the position of the maximum of the $M_{\tau\tau}$ distribution is used as the final estimator of $M_{\tau\tau}$ for a given event.

Realistic Detector Resolution While the 4-vector of the leptons are reconstructed with a good resolution (Fig. 2.5.4a), The missing energy, \cancel{E}_T , is badly reconstructed due to the low energy resolution in the Underlying Events (UE) and in high pileup environment. Missing energy resolution is shown in Fig.2.5.4b.

One can expect the effect of finite \cancel{E}_T resolution to degrade the algorithm performance. To mitigate these effects, the implementation of the MMC technique in a realistic experimental environment has to be adjusted to allow for possible mis-measurements in \cancel{E}_T . It is achieved

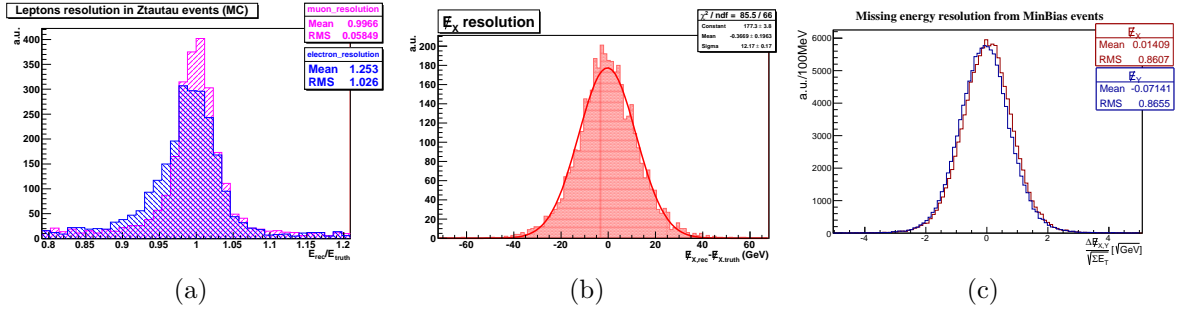


Figure 2.5.4: (a) Reconstruction resolution of the leptons and (b) \cancel{E}_X deviation from the true value - using Pythia $Z \rightarrow \tau\tau$ MC simulation, with preselection cuts; (c) Minimum bias event missing energy measurement resolution as function of ΣE_T taken from data.

by increasing the dimensionality of the parameter space in which the scanning is performed, to include the two components of the \cancel{E}_T resolution (for \cancel{E}_{T_x} and \cancel{E}_{T_y}). In this case, the event probability, \mathcal{P}_{event} , has to be augmented with the corresponding resolution:

$$\mathcal{P}_{event} = \mathcal{P}(\Delta R_1, \mathbf{p}_{\tau_1}) \times \mathcal{P}(\Delta R_2, \mathbf{p}_{\tau_2}) \times \mathcal{P}(\Delta \cancel{E}_{T_x}) \times \mathcal{P}(\Delta \cancel{E}_{T_y}) \quad (2.5.14)$$

where the probability functions $\mathcal{P}(\Delta \cancel{E}_{T_{x,y}})$ are defined as:

$$\mathcal{P}(\Delta \cancel{E}_{T_{x,y}}) = \frac{1}{\sqrt{2\pi\sigma^2}} e^{-\frac{(\Delta \cancel{E}_{T_{x,y}})^2}{2\sigma^2}} \quad (2.5.15)$$

where σ is the $\cancel{E}_{T_{x,y}}$ resolution ¹¹.

2.6 Modified MMC algorithm

In this section we will review the limitations of the old algorithm and suggest a modification which can provide better results.

2.6.1 Limitation of the old MMC algorithm

MMC technique offers better mass reconstruction for Higgs searches in the $H \rightarrow \tau\tau$ channels. However, in our study of the old algorithm, we have found a few weak points in its implementation.

Variable space In the presented old algorithm the probability space is based on ΔR distribution weighting functions. Already, the paper [54] pointed out that: “the 3-dimensional angle between the decay products might be a more natural choice”¹². Indeed the presented variable (ΔR) is not boost invariant in the sense that the distribution of the tau decay products is guided by its rest frame variables (θ, ϕ), and implies that ΔR variable will give different probability for different detector regions.

To show it we consider un-polarized τ decay. Here, the angle between the emitted lepton and the τ boost direction (denoted by $\cos\theta^*$, see Fig. 2.6.1) is distributed uniformly, i.e $\cos(\theta^*) \sim U(-1, 1)$.

¹¹In Ref. [54] the proposed resolution was $\sigma = 5\text{GeV}$, while in real analysis the resolution is $\approx 12\text{GeV}$ (see Fig. 2.5.4b)

¹²footnote 3

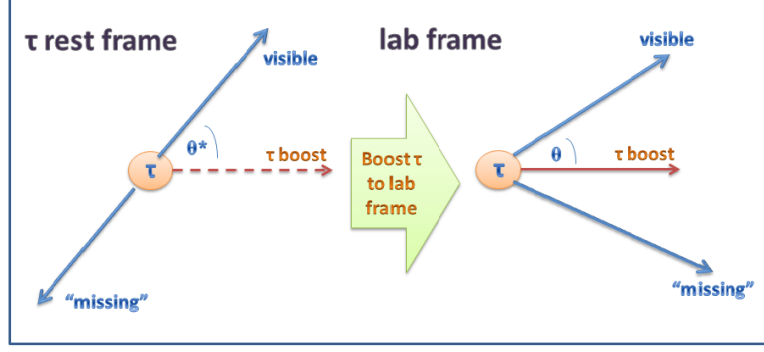


Figure 2.6.1: Tau lepton decay kinematics viewed in its rest frame and as measured in the lab frame, θ^* is the 3-dimensional angle between the τ boost direction and the visible decay product $\left(\cos(\theta^*) = \frac{\vec{\beta} \cdot \vec{\mathbf{P}}_{vis}}{|\vec{\beta}| |\vec{\mathbf{P}}_{vis}|}\right)$.

In single hadronic τ decays ($\tau^\pm \rightarrow h^\pm \nu_\tau$), where $m_{miss} = 0$ and $m_{vis} = 0$ (good approximation where the π^\pm mass is $\approx 140 \text{ MeV}/c^2$ [59]), the 3-dimensional angle in the lab frame (θ) can be related to the angle in the τ rest frame (θ^*) using the Lorentz Transformation:

$$\cos(\theta^*) = \frac{(1 + \cos(\theta)) - e^{2r} (1 - \cos(\theta))}{(1 + \cos(\theta)) + e^{2r} (1 - \cos(\theta))} \quad (2.6.1)$$

where r is the rapidity¹³ of the τ lepton. The probability function of the decay angle in the lab frame for a given \mathbf{p}_τ is:

$$\mathcal{P}(\theta|\mathbf{p}_\tau) = \mathcal{P}(\cos(\theta^*)) \left. \frac{\partial \cos \theta^*}{\partial \theta} \right|_{\mathbf{p}_\tau} = \frac{2e^{2r(|\mathbf{p}_\tau|)} \sin \theta}{(1 + \cos \theta + e^{2r(|\mathbf{p}_\tau|)} (1 - \cos \theta))^2} \quad (2.6.2)$$

The distribution of the angle in the lab frame is shown in Fig. 2.6.2.

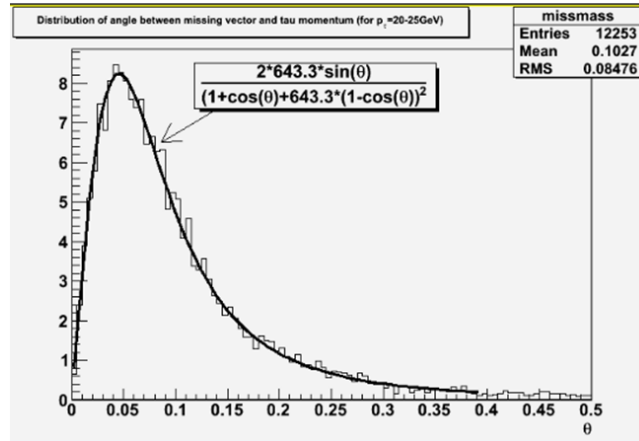


Figure 2.6.2: Distribution of $\mathcal{P}(\theta)$ using Eq. 2.6.2 for un-polarized hadronic 1-prong tau decay, with $20 \text{ GeV} < |\mathbf{p}_\tau| < 25 \text{ GeV}$ using $e^{2r} = 643.3$ at $|\mathbf{p}_\tau| = 22.5 \text{ GeV}$; simulated with Pythia where the τ decay products were given at true detector level.

Here, as an example, we show a perfect fit between MC simulation and an analytical function. This shows that the rest frame decay angle dictates the decay kinematics, and knowledge

¹³rapidity is defined by $r = \tanh^{-1} \beta = \frac{1}{2} \log \left[\frac{E+|\mathbf{p}|}{E-|\mathbf{p}|} \right]$. In case of massless particles when $E \rightarrow |\mathbf{p}|$: $r \rightarrow \eta$

of its probability distribution function will provide pure analytical expression for the decay probabilities.

In addition, we can conclude, that the probability function of $\mathcal{P}(\Delta R|\mathbf{p}_\tau)$ is not boost invariant. Fig. 2.6.3 is an example of this; the distribution is not the same for the center and forward regions.

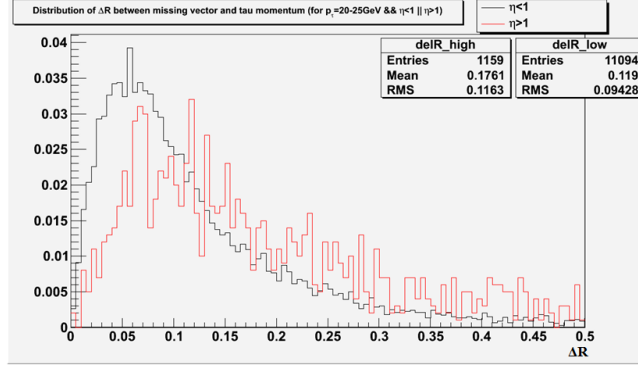


Figure 2.6.3: Distribution of ΔR for $20\text{GeV} < \mathbf{p}_\tau < 25\text{GeV}$ in the forward ($\eta > 1$) and central ($\eta < 1$) regions.

This gap in the MMC algorithm was presented in the ATLAS internal meeting [70], and led the authors of the algorithm to use the 3D angle rather than the ΔR variable.

Probability space The algorithm performs the scan in $[\Delta\phi, m_{miss}]$ phasespace, where $\Delta\phi = \phi_{vis} - \phi_{miss}$, while the probability distributions are derived in $[\Delta\theta_{3D}, m_{miss}]$ phasespace, where $\Delta\theta_{3D}$ is 3-dimensional angle between tau boost and the visible decay product in the lab frame. This lead to misinterpretation of the probability space. Once the scan space and the probability space are not the same, additional reweighing function is needed:

$$\mathcal{P}(\Delta\phi, m_{miss}) \equiv \mathcal{P}(\Delta\theta_{3D}, m_{miss}) \mathcal{J}(\Delta\theta_{3D}, m_{miss}) \quad (2.6.3)$$

where the reweighing function is the Jacobian defined by

$$\mathcal{J}^{-1}(\Delta\theta_{3D}, m_{miss}) = \left| \frac{\partial(\Delta\phi, m_{miss})}{\partial(\Delta\theta_{3D}, m_{miss})} \right| \quad (2.6.4)$$

MC dependence The old MMC algorithm uses a MC distribution of the scan variables for the weighting function. The distribution of angles in the lab frame is strongly dependent on the production mechanism and the relative boost of the system. The detector performance, and the beam parameters vary during the analysis (e.g. bunch spacing, center of mass energy of the beam or lepton triggers and reconstruction techniques), which may have a systematic effect on the variables distributions. This requires “on-line” tuning of the variables distributions.

2.6.2 Modified MMC algorithm

In order to have a better algorithm performance, an analytical-probability-based method was suggested. The main advantage, is that the current method relies on the theory, rather than on the MC distribution.

Probability distribution function τ leptons are spin- $\frac{1}{2}$ fermions that decay via the weak force (W-boson). In the τ rest frame its decay parameters can be calculated from the matrix elements¹⁴:

$$\mathcal{P}(\cos\theta^*, m_{miss}) = \frac{1}{\Gamma} \frac{\Gamma(\tau \rightarrow l\nu_l\bar{\nu}_\tau)}{d\cos\theta^* dm_{miss}} = \frac{1}{2M_\tau} \int \prod_{i=1,2,l} \frac{d^3p_i}{(2\pi)^3 2E_i} |\mathcal{M}|^2 (2\pi)^4 \delta^4(p_\tau - p_l - p_1 - p_2) \quad (2.6.5)$$

where p_τ , p_l , p_1 and p_2 are the tau, lepton, ν_τ and $\bar{\nu}_l$ 4-momenta respectively, and \mathcal{M} is the relevant matrix element given by:

$$|\mathcal{M}|^2 = 64G_F^2 m_\tau k_2^0 (p_1 \cdot p_l) (1 - \hat{p}_2 \cdot \hat{s}) \quad (2.6.6)$$

here \hat{p}_2 and \hat{s} are the unit vectors along the 3-momentum of the ν_l and the spin of the tau, respectively. In the τ rest frame the momenta (P^*), and the energy of its decay products (E_{vis}^* and E_{miss}^*), from two body decay, are given by:

$$\begin{aligned} P^* &= \frac{\sqrt{(M_\tau^2 - m_{vis}^2 - m_{miss}^2)^2 - 4m_{vis}^2 m_{miss}^2}}{2M_\tau} \\ E_{vis}^* &= \frac{M_\tau^2 + m_{vis}^2 - m_{miss}^2}{2M_\tau} \\ E_{miss}^* &= \frac{M_\tau^2 - m_{vis}^2 + m_{miss}^2}{2M_\tau} \end{aligned} \quad (2.6.7)$$

Integrating equation 2.6.5 with respect to the unmeasured momentum, one can express the probability in terms of the tau rest frame parameters in a limit of $m_{vis} \rightarrow 0$:

$$P(\cos\theta^*, x) = 2x(1-x^2)^2(1+2x^2) + \mathbf{P}_\tau \cos(\theta^*) 2x(1-x^2)^2(1-2x^2) \quad (2.6.8)$$

where \mathbf{P}_τ is the tau helicity in the Higgs/Z rest frame and $x = \frac{m_{miss}}{M_\tau}$. Single tau leptons are created un-polarized (by choosing a single tau lepton its polarization can be $\mathbf{P}_\tau = \pm 1$)¹⁵; thus it is uniformly distributed over $\cos\theta^*$. The single tau distribution is shown in Fig. 2.6.4 for the Z/ γ^* and Higgs decays.

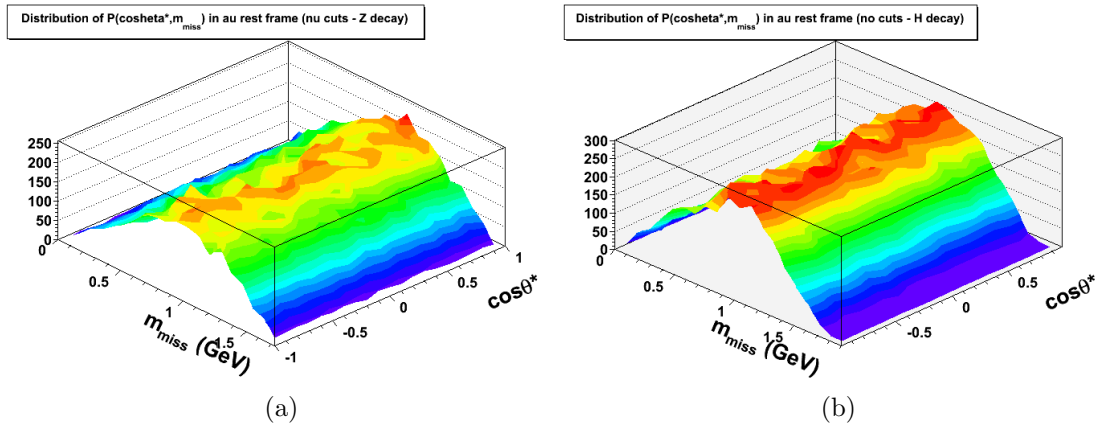


Figure 2.6.4: Single tau decay: $\mathcal{P}(\cos\theta, m_{miss})$ distribution for (a) $Z \rightarrow \tau\tau$ decay; (b) $Higgs \rightarrow \tau\tau$ decay. No selection cuts are applied

¹⁴Special thanks to K. Blum for helping with the matrix element calculations.

¹⁵Although single tau decay un-polarized spin dependence can be observed through spin-correlation, in current analysis spin correlation were neglected .

Phasespace definition A proper choice of the scanned phasespace will force one to use the correct Jacobian transformation. The usage of Jacobian matrix might have a systematic effect on the algorithm performance. While the scan over the whole phasespace is performed numerically, the analytical calculation might be inappropriate. For example, if one considers the traditional scan $[\Delta\phi, m_{miss}]$, then the Jacobian matrix will be defined by:

$$\mathcal{J}(\Delta\phi, m_{miss}) = \left| \frac{\partial \cos \theta^*}{\partial \Delta\phi} \right| \quad (2.6.9)$$

The specific Jacobian have a singular point when two solutions for P_Z (equation 2.5.12) converge into a single solution. Similar solutions in the massless limit refers to $\Delta\theta$, and $-\Delta\theta$ grid points, and the singularity occurs at $\Delta\theta \rightarrow 0$. This lead to an additional complexity regarding the phasespace calculation. In order to avoid this complexity we define the scan phasespace to be the probability phasespace.

Phasespace solution In defining the probability space to be the scan space, we need to obtain the di-tau resonance mass for each $[\cos \theta^*, m_{miss}]$ grid point. The boost of the tau lepton and the decay angle in its rest frame is related through the visible decay product energy:

$$E_l = \gamma_\tau (E_l^* + \beta_\tau P^* \cos \theta_{\tau,lep}^*) \quad (2.6.10)$$

where the rest frame parameters the same as those defined in equation 2.6.7.

Once both di-neutrino missing energy and the momentum magnitude are both calculated, the rest of the parameters can be obtained from the missing energy constraint (eq. 2.5.9), and from the constraint on the τ mass (eq. 2.5.10). By manipulating the equations, we obtain a quartic equation for $P_{Z,miss}$. The quartic equation is solved analytically using Ferrari method which was first proposed by Lodovico Ferrari in 1540¹⁶ [72]. From multiple solutions, due to numerical limitations, we use only the one which gives the most precise values from substituting back in equations 2.5.9 and 2.5.10. The di- τ resonance mass then is given by:

$$M_{MMC} = \max_m \int \mathcal{P}(\vec{x}, \vec{m}_{miss}) \delta(m - M_{grid}(\vec{x}, \vec{m}_{miss})) d\vec{x} d\vec{m}_{miss} \quad (2.6.11)$$

where

$$\begin{aligned} M_{grid}^2(x_i, m_{miss,i}) = & \left(\sum_{i=1}^2 E_{vis,i} + E_{miss,i}(x_i, m_{miss,i}) \right)^2 \\ & - \left| \sum_{i=1}^2 \vec{P}_{T,vis,i} + \vec{E}_T \right|^2 \\ & - \left(\sum_{i=1}^2 P_{Z,vis,i} + P_{Z,miss,i}(x_i, m_{miss,i}) \right)^2 \end{aligned} \quad (2.6.12)$$

and

$$x_i = \cos \theta_i^* \text{ for } i \in \{1, 2\} \quad (2.6.13)$$

¹⁶It is reported that even earlier, in 1486, Spanish mathematician Paolo Valmes claim to have solved the quartic equation but he was sentenced by Inquisitor General Tomás de Torquemada to be burned at the stake because “it was the will of God that such a solution be inaccessible to human understanding” [71].

2.6.3 MMC Systematics study

Effects of kinematic cuts It seems that we can use un-polarized tau decay kinematics, but once we apply a p_T cut on the measured leptons (i.e. $p_{T,lep} > 20$ GeV), the decay angle, $\cos\theta^*$, is no longer distributed uniformly. By choosing events where the lepton transverse momentum is restricted to be high, the distribution $\mathcal{P}(\cos\theta^*)$ changes such that the lepton is preferably emitted in the direction of tau propagation. The angular distribution is shown in figure 2.6.5 vs various p_T cuts.

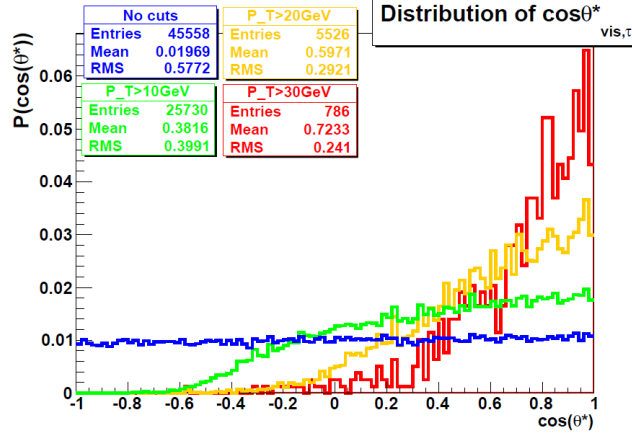


Figure 2.6.5: Distributions of $\cos\theta^*$ distribution vs lepton p_T cut.

For the first approximation, we used polarized tau distribution, which has a similar shape for accepted events¹⁷. It should be pointed out that the shape structure is not due to the specific spin decay, but rather, is guided only by the leptonic cuts.

Effect of unmeasured \cancel{E}_T The missing energy resolution is expressed as $\sigma(\cancel{E}_T)$. For a good approximation it scales as:

$$\sigma(\cancel{E}_T) = noise + \alpha \sqrt{\sum E_T} \quad (2.6.14)$$

where *noise* is commonly set to zero¹⁸, and $\sum E_T$ is the scalar sum over the transverse energy. An example of the missing energy resolution is shown in Fig. 2.5.4b for $H \rightarrow \tau\tau \rightarrow leplep$ channel and in Fig. 2.5.4c for minimum bias events as measured from 2011 data. The high range of uncertainty dramatically increases the available phase space and the reconstructed mass is widely spread. A comparison between the reconstructed mass with ideal and real missing energy resolution is shown in Fig. 2.6.6. A scan over a high range of missing energy produces a shift to lower masses. The missing energy resolution increases the phase space scan size. The higher weights are correlated with lower reconstructed mass values. The energy of the emitted lepton can be expressed in terms of tau rest frame parameters (2.6.7), tau boost β_τ and the decay angle ($\cos\theta^*$) shown in equation 2.6.10. In the massless limit one can write:

$$\beta_\tau = \frac{\sqrt{1 - (y \sin\theta^*)^2} - y^2 \cos\theta^*}{1 + (y \cos\theta^*)^2} = 1 - \frac{y^2}{2}(1 + \cos\theta^*)^2 + \mathcal{O}(y^4) \quad (2.6.15)$$

¹⁷More precise attitude should involve calculation of matrix elements in the lab frame or propagate the lepton p_T cut to probability phase-space

¹⁸It being observed that for $H \rightarrow \tau\tau \rightarrow leplep$ decay channel it differs from zero - future study is needed.

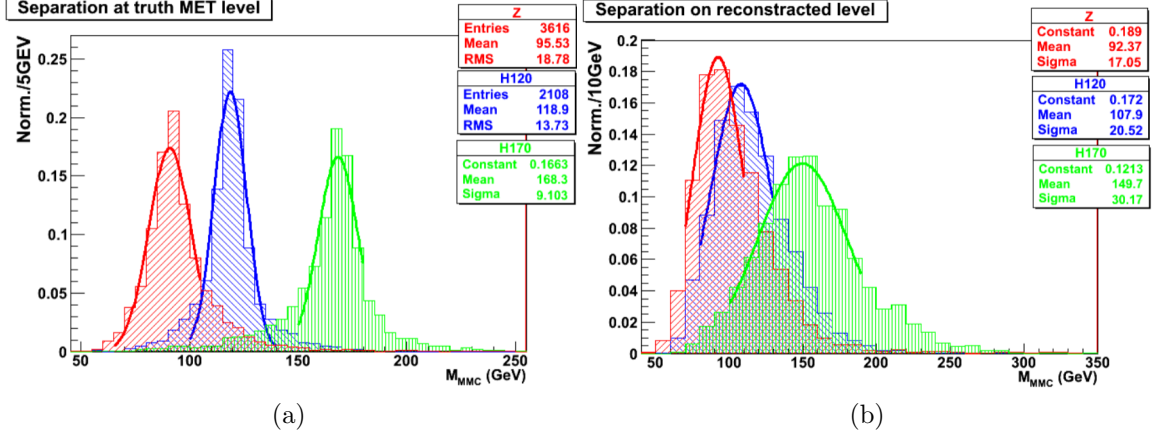


Figure 2.6.6: Reconstructed mass for: (a) true missing energy (4d scan), (b) real missing energy (6d scan): **red**- $Z \rightarrow \tau_{lep}\tau_{lep}$, **blue**- $H_{120} \rightarrow \tau_{lep}\tau_{lep}$ and **green**- $H_{170} \rightarrow \tau_{lep}\tau_{lep}$

where $y = \frac{M_\tau}{2E_l}$. More probable phasespace points ($\cos\theta^* \rightarrow 1$) are related to lower masses (β_τ decreases to $1 - y^2$). Thus when the phasespace expands, the reconstructed mass may drift to lower mass region.

2.6.4 \cancel{E}_T correction method

In order to minimize the effect of missing energy resolution on the di-tau resonance mass, a phasespace-guided correction technique is used. In the range of 3σ (\cancel{E}_T), 6D scan over the phasespace was performed. For each $(\cancel{E}_X, \cancel{E}_Y)$ grid point, the corresponding weight was calculated. The weight is defined as the total phasespace probability for a given value of missing energy that is restricted only to the physical solutions (a physical solution is a solution where the solution exists and satisfy $E_\tau^2 > M_\tau^2$). The weight is defined to be:

$$\omega(\vec{\cancel{E}}_T) = e^{-\frac{|\Delta\cancel{E}_T|}{2\sigma^2}} \int_{\text{physical}} \prod_{i=1}^2 \mathcal{P}_i(\cos\theta_i^*, m_{i,miss}) d\cos\theta_i^* dm_{i,miss} \quad (2.6.16)$$

The larger and more probable phasespace gains a higher weight for the missing energy values. The correction to the missing energy resolution is shown in figure 2.6.7. Using the

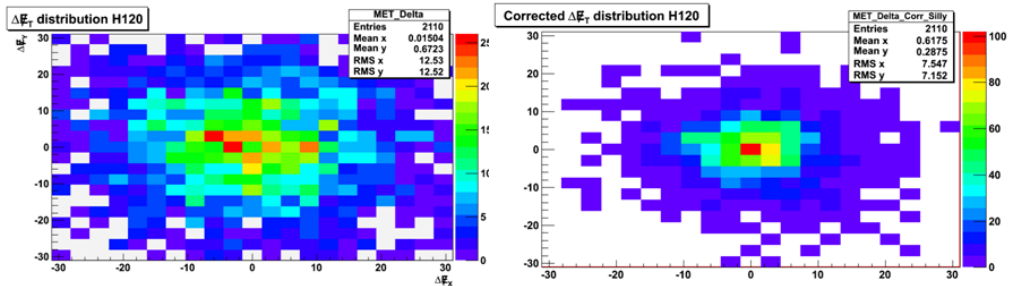


Figure 2.6.7: Missing energy correction from phasespace-guided method in $Z \rightarrow \tau\tau$ decay. Missing energy resolution before (left) and after (right) the correction.

correction method with the corrected missing energy values, a 4D scan is performed, and the di-tau mass is estimated for the corrected missing energy value.

2.7 Results and conclusions

The Modified MMC algorithm, which uses a theory driven approach rather than a MC, shows better mass reconstruction ability than the old algorithm. A comparison between the old and the modified MMC for SM Higgs boson of 120 GeV shown in Fig. 2.7.1. We should notice that the old algorithm was not tuned for this specific MC for the lep-lep channel, thus it shows a shift to the lower masses. The old algorithm reconstructed mass is ~ 100 GeV instead of 120 GeV, while the modified MMC shows a peak at 120 GeV.

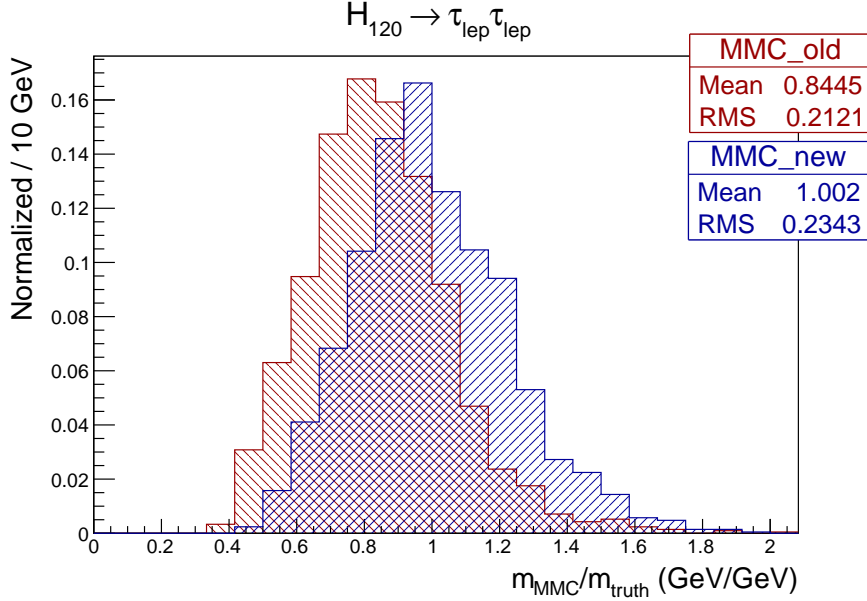


Figure 2.7.1: Comparison between old (MissingMassCalculator-00-00-06) and new modified MMC mass reconstruction algorithms for SM Higgs boson of 120 GeV using preselection cuts.

In addition, the MMC technique shows better performance than the existing mass reconstruction algorithms. The collinear approximation (as mentioned in sec. 2.5.3) cuts events with $x_{1,2} < 0.1$ which gives $\approx 55\%$ signal efficiency while the MMC algorithm does not require such cuts and has a high reconstructed efficiency - $> 97\%$. The effective mass gives a lower separation power than the MMC. A comparison between the collinear and MMC mass are plotted in Fig. 2.7.2 for the expected background in $H \rightarrow \tau\tau \rightarrow e\mu$ channel at $4.6 fb^{-1}$ for the 0 and 1 jet analysis. And a comparison between the effective mass and the MMC is shown in figure 2.7.3.

For 0-jet analysis channel, MMC algorithm gives $\times 2.6$ better sensitivity. The MMC mass also gains a higher efficiency than the collinear approximation for multi-jet analysis. Thus it can be implemented in the multijet analysis by dropping the collinear cut. The modified MMC algorithm may be the promising mass estimator not for $H \rightarrow \tau\tau \rightarrow leplep$ channel only, but for all three sub-channels as well. Nevertheless, future study of this technique can improve the current performance (e.g. analytical modeling of the effect of leptonic p_T cut on the angular distribution).

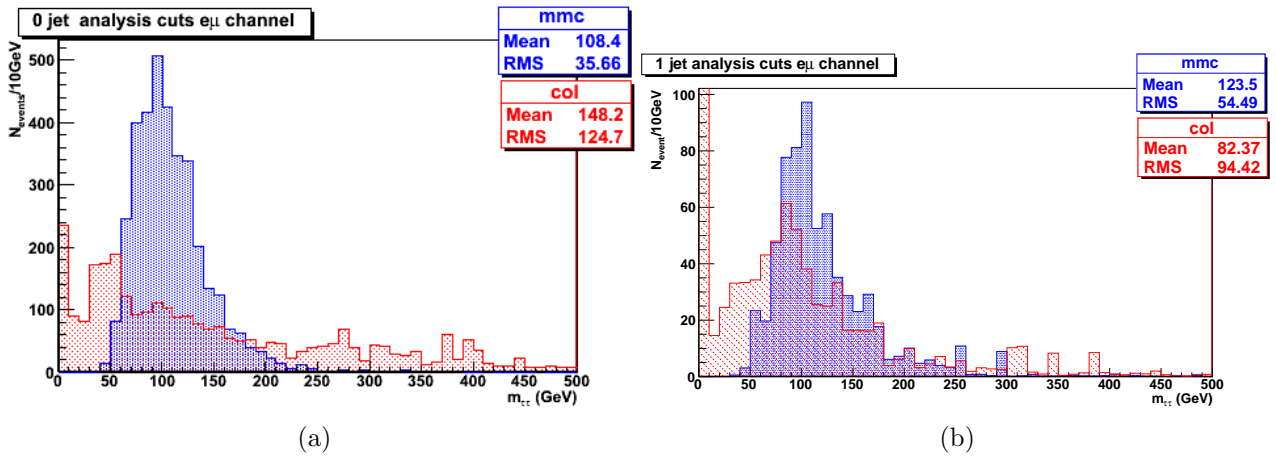


Figure 2.7.2: A comparison between the MMC and the collinear mass performances: (a) 0-jet analysis - using only preselection cuts; (b) 1 jet analysis up to collinear cut

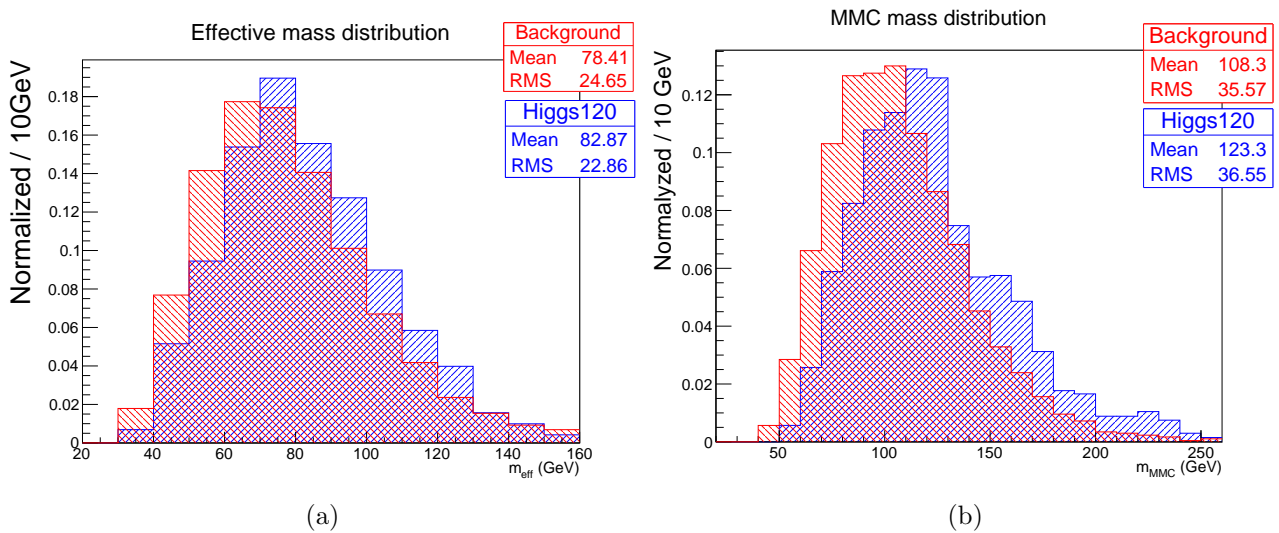


Figure 2.7.3: A comparison between the background and the signal (ggH) for 0 jet analysis: (a) Effective mass (b) MMC mass

Spin Dependent Cross section analysis for XENON100 experiment

3.1 Introduction

According to the Standard model of Cosmology (Λ CDM model), the total mass-energy of the universe is made of dark energy, luminous matter and dark matter. Observations confirm this picture and report that the universe consists of $\sim 72.8\%$ Dark energy [73], $\sim 4.5\%$ ordinary matter¹, and the remaining $\sim 22.7\%$ is the so called Dark matter (see Fig. 3.1.1).

Dark Matter (DM) is a hypothetical matter that does not emit or scatter light, but its mass shows gravitational effects. The Concept of DM is devised from the discrepancy between masses observed in gravitational effects and contained in luminous matter. The term 'Dark matter' was initially coined by Fritz Zwicky who was the first to find evidence for missing (or unseen) mass by applying the virial theorem to the Coma cluster of galaxies.

Over the years, additional observations at various scales (galaxies, clusters of galaxies and the whole universe) supported the existence of DM. Despite these overwhelming evidence, the exact nature of DM remains a mystery. The standard model of particle physics does not contain any heavy, stable, non-baryonic particle, and new physics "beyond the standard model" is highly motivated. Cold Dark Matter (CDM) is the dominant component of the the universe [74] which comprises the local galactic halo. CDM consist of particles having negligible thermal velocity with respect to the Hubble flow, thus they are considered as non-relativistic particles. The most popular candidates for CDM are the Weakly Interacting Massive Particles (WIMPs). The WIMPs could make up a major component of the dark matter in our own galactic halo. A few representative evidence for dark matter are summarized in the next section.

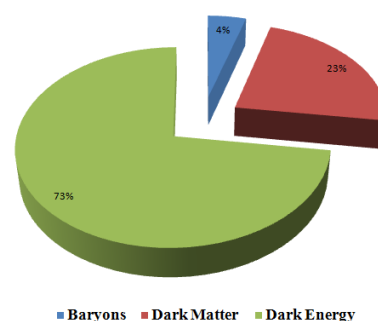


Figure 3.1.1: Current mass Energy Distribution of the Universe

¹Ordinary matter is matter made of neutrons and protons; the jargon for this is baryons, the technical term for particles made of quark triplets

3.1.1 Observational evidence of Dark Matter

Inner-Galactic level - rotation curves: The orbital velocity $v(r)$ of matter (stars or gas) in the galaxy due to the gravitational potential is governed by the Newtonian dynamics:

$$v(r) = \sqrt{\frac{M(r)}{r}} \quad (3.1.1)$$

where $M(r)$ is the mass up to distance r .

The major mass of the galaxy is contained in a visible disk and $M(r)$ is expected to be constant at the outer edges of the galaxy with an expected velocity profile of $v(r) \propto 1/\sqrt{r}$. The observations bring a big surprise: The measured velocity profile at the edge of the galaxy is not falling as expected, and is independent of r [75]. A possible explanation is that the actual mass density profile is $\rho(r) \propto 1/r^2$ (for a spherical mass distribution) and a Dark Matter 'halo' is proposed to exist.

Extra-Galactic level: The existence of additional unseen matter can be proven by virial methods, gravitational lensing and velocity dispersion in groups and clusters of galaxies².

For a gravitational potential the virial theorem states:

$$\langle T \rangle = -\frac{1}{2} \langle V \rangle \quad (3.1.2)$$

where $\langle T \rangle$ is the average kinetic energy and $\langle V \rangle$ is the average potential energy, and the mass can be determined based on the galaxies' velocity. Zwicky was the first to measure the velocity dispersion of galaxies in the Coma cluster based on the virial theorem. He found that objects in the periphery of the Coma cluster orbited faster than expected by the mass inferred by its luminosity [76]. Later many measurements of velocity dispersion were performed, Girardi et. al. have also applied the virial theorem on a sample of about 100 galaxy-clusters from various surveys [77].

Dark matter has also been observed indirectly in galaxy-clusters via gravitational lensing. When light travels near a massive object, its path becomes bent by the gravitational field [78]. If the observer, the massive object and a distant light source are roughly aligned, light is focused as if it passed through an optical lens. By analyzing the image, the mass distribution of the "lens", usually clusters of galaxies, could be determined. A survey with gravitational lensing on 22 galaxies done by Gavazzi et al. [79] shows a consistent mass density profile of $\rho(r) \propto 1/r^2$ across galaxies.

Cosmic Microwave Background (CMB): The CMB was first proposed by Robert Dicke in 1946 and was first detected by Penzias and Wilson in 1964 [80]. Its detection was a crucial support to the Big Bang Theory. The CMB is mostly uniform black body radiation with a mean temperature of $2.725 \pm 0.002^\circ K$ [81]. Small fluctuations in CMB were revealed by WMAP team [73] (CMB Anisotropy). These fluctuations can be used to estimate the radiation, baryon and dark matter densities.

3.2 Direct detection of DM

One of the promising ways to detect CDM is to look for signatures of their nuclear recoil against target nuclei of a terrestrial detector. As our Solar system moves through the galaxy, the relative

²groups $\lesssim 50$ and clusters $\gtrsim 50$ of galaxies

velocity between Earth and the dark matter halo changes leading to annual modulations in the expected (or measured) WIMP scatter rate. Although few experiments claim for a positive annual modulation signal (DAMA/LIBRA with 8.9σ [82] and CoGeNT with $\sim 2.8\sigma$ [83]), other experiments report null results (XENON experiment [84, 85] and CDMSII experiment [86]), leaving a confusing picture that has motivated much theoretical and experimental work in various directions (e.g. see [87]). In the following subsections the mathematical framework of the DM direct detection is presented ³.

3.2.1 DM distribution in MW galaxy

Rotation curves of our galaxy consist of isotropic distribution of DM particles. In our solar system, the local DM density is expected to be $\rho_D = 0.3 \text{GeVcm}^{-3}$ [89]. It is assumed that the velocity of the DM particles follow a Maxwell-Boltzmann distribution, and with respect to an observer on Earth it is given by:

$$f(\mathbf{v}, \mathbf{v}_E) = e^{-(\mathbf{v}+\mathbf{v}_E)^2/v_0^2} \quad (3.2.1)$$

where $v_0 = 220 \frac{\text{km}}{\text{sec}}$ is the characteristic velocity of DM particles [90] and $v_E = 220 \frac{\text{km}}{\text{sec}}$ is the earth velocity relative to the DM distribution [91] ⁴

The DM particles velocity is constrained by the escape velocity that lies within the range $498 \frac{\text{km}}{\text{sec}} < v_{esc} < 608 \frac{\text{km}}{\text{sec}}$ (90%CL) [91], with median likelihood value of $v_{esc} = 544 \frac{\text{km}}{\text{sec}}$. DM particles with faster velocities ($v > v_{esc}$) are no longer bounded.

3.2.2 Rate of WIMP-nucleus interaction

The event rate per unit mass of a target defined as:

$$dR = \frac{N_0}{A} \sigma v dn \quad (3.2.2)$$

where $N_0 = 6.022 \cdot 10^{23} \text{mol}^{-1}$ is the Avogadro number, v is the DM particle velocity, σ is the WIMP-nucleus cross section and dn is differential particle density which is given by:

$$dn = \frac{n_0}{k} f(\mathbf{v}, \mathbf{v}_E) d^3v \quad (3.2.3)$$

where $n_0 = \frac{\rho_D}{M_D}$ is mean dark matter particle number density and k is a normalization factor defined by:

$$k = 4\pi \int_0^{v_{esc}} f(v, v_E) v^2 dv \quad (3.2.4)$$

for $v_{esc} = \infty$ define k_0 to be:

$$k_0 = 4\pi \int_0^{\infty} f(v, v_E) v^2 dv = (\sqrt{\pi} v_0)^3 \quad (3.2.5)$$

and for $|\mathbf{v} + \mathbf{v}_E| = v_{esc}$ we define k_1 to be:

$$k_1 = k_0 \left[\text{erf} \left(\frac{v_{esc}}{v_0} \right) - \frac{2}{\sqrt{\pi}} \frac{v_{esc}}{v_0} e^{-\frac{v_{esc}^2}{v_0^2}} \right] \quad (3.2.6)$$

³Based on work by Lewin & Smith [88]

⁴Due to annual modulations the correction to the earth velocity is $v_E + 15 \sin(2\pi y) \frac{\text{km}}{\text{sec}}$, where y is the fraction of the year [88]

For $v_0 = 220 \frac{km}{sec}$ and $v_{esc} = 544 \frac{km}{sec}$, we obtain $k_1/k_0 = 0.9934$.

For $v_E=0$ and $v_{esc} = \infty$, we define R_0 which is conventionally expressed in units of $kg^{-1}d^{-1}$ or total rate unit (tru):

$$R_0 = \frac{540}{AM_D} \left(\frac{\sigma}{1pb} \right) \left(\frac{\rho_D}{0.4 GeV c^{-2} cm^{-3}} \right) \left(\frac{v_0}{230 km s^{-1}} \right) kg^{-1} d^{-1} \quad (3.2.7)$$

Thus we can express differential rate in the terms defined above to be:

$$dR = R_0 \frac{k_0}{k} \frac{1}{2\pi v_0^4} v f(\mathbf{v}, \mathbf{v}_E) d^3v \quad (3.2.8)$$

The recoil energy of a nucleus struck by a DM particle of kinetic energy $E = \frac{1}{2}M_D v^2$ scattered at angle θ in center-of-mass is $E_R = Er(1 - \cos\theta)/2$, where r is a kinematic factor equals to $\frac{4M_D M_A}{(M_D + M_A)^2}$.

For an isotopic scattering ($\cos\theta \sim Uni(-1, 1)$) in the range $0 \leq E_R \leq Er$ we can write:

$$\frac{dR}{dE_R} = \int_{E_{min}}^{E_{max}} \frac{1}{Er} dR(E) = \frac{1}{E_0 r} \int_{v_{min}}^{v_{esc}} \frac{v_0^2}{v^2} dR(v) \quad (3.2.9)$$

where $v_{min} = v_0 \sqrt{\frac{E_R}{E_0 r}}$ is the minimal WIMP velocity that can give E_R via elastic scattering, and $E_0 = \frac{1}{2}M_D v_0^2$. The differential rate is given by integrating the velocities from v_{min} to v_{esc} ⁵:

$$\frac{dR}{dE_R} = \begin{cases} \frac{k_0}{k_1} \frac{R_0}{E_0 r} \frac{\sqrt{\pi}}{4} \frac{v_0}{v_E} \left[erf\left(\frac{v_{min}+v_E}{v_0}\right) - erf\left(\frac{v_{min}-v_E}{v_0}\right) - \frac{4}{\sqrt{\pi}} \frac{v_E}{v_0} e^{-\frac{v_{esc}^2}{v_0^2}} \right] & v_{min} + v_E < v_{esc} \\ \frac{k_0}{k_1} \frac{R_0}{E_0 r} \frac{\sqrt{\pi}}{4} \frac{v_0}{v_E} \left[erf\left(\frac{v_{esc}}{v_0}\right) - erf\left(\frac{v_{min}-v_E}{v_0}\right) - \frac{2}{\sqrt{\pi}} \frac{\tilde{v}}{v_0} e^{-\frac{v_{esc}^2}{v_0^2}} \right] & |v_{esc} - v_{min}| < v_E \\ 0 & v_{min} > v_E + v_{esc} \end{cases} \quad (3.2.10)$$

where $\tilde{v} = v_E + (v_{esc} - v_{min})$.

By integrating the differential rate in the detector's energy range, the expected rate can be obtained.

3.2.3 Cross section calculation

The differential rate in equation (3.2.10) is a function of the WIMP-nucleus cross section. The cross section at finite energy transfer scales as $\sigma_A(q) = \sigma_A^0 F^2(q)$, where q is the momentum transferred to the target nucleus A by the scattered particle ($q = \sqrt{2M_A E_R}$ where E_R is the recoil energy) and $F^2(q)$ is the form-factor and will be described latter.

The interaction between WIMP to nucleus WIMP-nucleus elastic cross section for spin independent (SI) and spin dependent (SD) interactions for zero momentum transfer can be written as

$$\sigma_A^0 = 4G_F^2 \mu_A^2 C_A \quad (3.2.11)$$

where G_F is Fermi constant, $\mu_A = M_A M_D / (M_A + M_D)$ is the WIMP-nucleus reduced mass and C_A is the 'enhancement factor' defined in ref [89], which depends on the type of the interaction, and is given by:

$$C_A = \begin{cases} \frac{1}{\pi G_F^2} [Z f_p + (A - Z) f_n]^2 & \text{SI} \\ \frac{8}{\pi} [a_p \langle S_p \rangle + a_n \langle S_n \rangle]^2 \frac{J+1}{J} & \text{SD} \end{cases} \quad (3.2.12)$$

⁵Full derivation can be found in Appendix A in ref [88]

where $f_{p,n}$ and $a_{p,n}$ are the effective WIMP-proton or WIMP-neutron coupling constants for SI and SD interaction respectively, $\langle S_{p,n} \rangle = \langle N | S_{p,n} | N \rangle$ is the proton (neutron) spin expectation value, and J is the total nuclear spin.

SI cross section For iso-spin conserving DM interaction same interaction strength for neutron and proton is assumed ($f_p = f_n$)⁶, and the Z term is canceled out, simplifying the cross section expression to:

$$\sigma_A^0 = \frac{4}{\pi} \mu_A^2 f_n^2 A^2 \quad (3.2.13)$$

The above equation can be used to specify the zero momentum-transfer WIMP-neutron interaction: $\sigma_n^0 = \frac{4}{\pi} \mu_n^2 f_n^2$, where μ_n is WIMP-nucleon reduced mass. To allow comparison between different experiments (which may have different target nuclei) it is convenient to express the WIMP-nucleus cross section in term of WIMP-nucleon cross section at zero momentum transfer:

$$\sigma_A(q) = \sigma_n(0) \left(\frac{\mu_A}{\mu_n} \right)^2 A^2 F^2(q) \quad (3.2.14)$$

where μ_n is WIMP-nucleon reduced mass. Thus using cross section from (3.2.14) in equation (3.2.10) one can obtain a desirable expected rate of WIMP-nucleon interactions.

SD cross section In SD interaction WIMP-nucleus cross section, σ_A , can be written as

$$\sigma_A(q) = \frac{32}{\pi} G_F^2 \mu_A^2 (a_p \langle S_p \rangle + a_n \langle S_n \rangle)^2 \frac{J+1}{J} F^2(q) \quad (3.2.15)$$

The definition of C_A normalizes the spin-dependent nuclear form factor $F^2(q)$ used in calculating nuclear recoil energy spectra to unity at $q=0$:

$$F^2(q) = \frac{S(q)}{S(0)} \quad (3.2.16)$$

where

$$S(q) = a_0^2 S_{00}(q) + a_1^2 S_{11}(q) + a_0 a_1 S_{01}(q) \quad (3.2.17)$$

here S_{ij} represent iso-scalar, iso-vector and interference term form factor and $a_0 = a_p + a_n$ and $a_1 = a_p - a_n$ are the iso-scalar and iso-vector coefficients respectively. Both a_p and a_n are defined by various models, hence expressing WIMP-nucleus cross section in terms of WIMP-nucleon cross section becomes problematic.

Form Factors corrections As the momentum transfer increases, such that wavelength h/q is no longer large compared to the nuclear radius, the effective cross section begins to decrease. The Form Factors are presented using a dimensionless parameter $u \propto (qb)^2$ or $u \propto qr_n$, where r_n is the effective nuclear radius and b is the nuclear harmonic-oscillator size parameter defined by:

$$b = \sqrt{\frac{\hbar}{m\omega}} \quad (3.2.18)$$

with $\hbar\omega = 45A^{-1/3} - 25A^{-2/3}$ MeV (taken from Blomqvist-Molinari formula [93]), and $\hbar^2/m = 41.467$ MeV.

Once the cross section is written in the form $\sigma(u) = \sigma_0 F^2(u)$, the results can be expressed in

⁶for iso-spin violating dark matter see [92]

an almost model independent fashion⁷.

For SI interactions the form factors are calculated using Born approximation where the form factor is the Fourier transform of $\rho(r)$, the density distribution of the 'scattering centers':

$$F(q) = \int \rho(r) e^{i\mathbf{q}\cdot\mathbf{r}} d^3\mathbf{r} = \frac{4\pi}{q} \int_0^\infty r \sin(qr) \rho(r) dr \quad (3.2.19)$$

For SI interaction the so-called "folded" charge distribution is used, defined by:

$$\rho(r) = \int \rho_0(r) \rho_1(r - r') dr' \quad (3.2.20)$$

The advantage of using such form is that one can use two trial functions: ρ_0 which essentially defines the nuclear radius and ρ_1 a surface thickness. It sufficient to take for ρ_0 a uniform distribution of radius $R \sim r_0 A^{\frac{1}{3}}$ where $r_0 \sim 1.2$ fm, and for ρ_1 take spherically symmetric distribution. Examples for such distribution are presented in Ref. [94]. The Form Factor in this case is:

$$F(qr_n) = 3 \frac{j_1(qr_n)}{qr_n} \times e^{-(qs)^2/2} \quad (3.2.21)$$

where r_n is the nuclei effective radius and $s = 1$ fm \approx surface thickness [95].

Unfortunately, SD interaction scattering is not nearly as simple. The Form factors are calculated using effective nucleon-nucleon (NN) potentials (e.g. see [96]), and are differ for different isotopes.

3.3 XENON100 experiment

XENON100 is a dual phase (liquid/gas) time projection chamber (TPC), which employs 161 kg of ultra pure liquid xenon (LXe) at a temperature of $\sim -90^\circ\text{C}$ for direct DM searches. Drawing of the detector is shown in Fig 3.3.1a. The sensitive volume consists of 62 kg LXe in an optically decoupled cylindrical tank, surrounded by 99 kg of LXe that provide passive shielding from external radio-active background. Arrays of Photo-Multiplier-Tubes (PMTs) are arranged at the top and the bottom of the detector.

Xenon is a noble gas with a high atomic mass ($A \approx 130$) which gives rise to a strong self shielding ability, and a high sensitivity to SI interaction which scales as $\sigma \propto A^2$. Of all the noble elements, xenon in liquid form has the second highest density at about $3\text{g}/\text{cm}^3$. Natural xenon contains different isotopes, as listed in table 3.1. The Xenon target is poorly sensitive

Table 3.1: Natural (NA) abundance of Xenon isotopes

^{124}Xe	^{126}Xe	^{128}Xe	^{129}Xe	^{130}Xe	^{131}Xe	^{132}Xe	^{134}Xe	^{136}Xe
0.095%	0.089%	1.91%	26.4%	4.07%	21.2%	26.9%	10.4%	8.86%

to SD WIMP-proton interaction due to its even number of protons ($Z = 54$), but it has good sensitivity to WIMP-neutron interaction due to the high fraction of the two odd-neutron isotopes ^{129}Xe and ^{131}Xe which make about half of its volume.

When a particle interacts with the liquid xenon, scintillation light (S1) and ionization electrons (S2) are produced. The primary scintillation light is collected by the array of PMTs and

⁷For SD interaction the treatment is not straightforward due to dependence of $F(q)$ in the specific model (see eq. 3.2.17). For model independent treatment in SD case see section 3.4.1

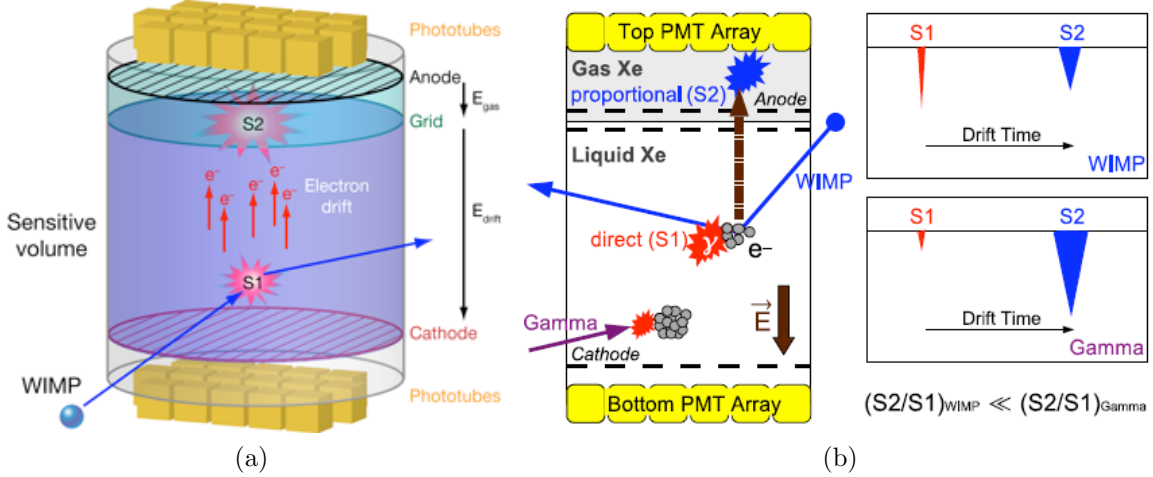


Figure 3.3.1: (a) Drawing of XENON100 TPC (b) Principle of a LXe TPC, providing 3D position information and electron recoil/nuclear recoil discrimination.

becomes the “S1 pulse” while the ionization electrons drift upward at constant drift velocity of $v_d = 1.74\text{mm}/\mu\text{s}$, enter the gas phase, and produce proportional scintillation light that becomes the “S2 pulse” on the top PMT array.

The time and shape of the S1 and the S2 pulses are used to characterize each event: The Z position of the interaction point is reconstructed using the time difference between the S1- and the S2-pulses, and the X-Y position is reconstructed using the localized S2 pattern produced on the top array. The magnitudes of S1 and S2, eventually converted to the number of scintillation photons and ionization electrons provide energy estimation. An important feature of the dual-phase TPC is signal/background discrimination using the S2/S1 ratio which is different for weak interaction scatters (referred to as Nuclear Recoil NR), and for electromagnetic interaction scatters (Electronic Recoil, ER), providing the basis for background discrimination in XENON100 experiment (Fig. 3.3.1b).

3.4 Setting SD limit

XENON100 experiment have the ability to test the DAMA and CoGeNT allowed region, and due to a null signal result set an upper limit for WIMP-nucleon interaction. After the SI limit was presented by the XENON100 collaboration [84], we calculate the SD limit also. In the following section, we summarize the calculation procedure for setting the observed limit as a function of the WIMP-nucleon cross section in the model independent manner.

3.4.1 Model independent approach

WIMP-nucleus cross section is given in Eq. 3.2.15. In SD case both interaction couplings a_n and a_p , depend on the WIMP model, moreover also the form factor depend on the interaction couplings (eq. 3.2.17). To avoid model dependence in limit calculation one can use a simple approach that allows a straightforward comparison in a model independent way [97]. Using equation (3.2.15) we can write WIMP-neutron(proton) cross-section as $\sigma_{n,p} = \frac{24}{\pi} G_F^2 \mu_{n,p}^2 |a_{n,p}|^2$. Now we will assume that only neutrons contribute to the scatter (by setting $a_p = 0$) or only protons ($a_n = 0$) and write the WIMP-nucleon cross section (for pure neutron or pure proton

interaction) in terms of WIMP-proton(neutron) cross section:

$$\sigma_A = \sigma_{p,n} \frac{4}{3} \left(\frac{\mu_A}{\mu_{p,n}} \langle S_{p,n} \rangle \right)^2 \frac{J+1}{J} \quad (3.4.1)$$

3.4.2 Form factors and spin expectation values

The form factors and spin expectation values for xenon odd-neutron isotopes (^{129}Xe and ^{131}Xe) have been calculated by J. Suhonen et al. [98]. We obtained from the author the spin structure functions in numerical form. S_{ij} from eq. 3.2.17 can be obtained from the spin structure functions using conversion formula (18) in ref. [99]:

$$S_{\rho\rho'} = \frac{1}{1 + \delta_{\rho\rho'}} \frac{2J+1}{8\pi} \Omega_\rho \Omega_{\rho'} F_{\rho\rho'}(u) \quad (3.4.2)$$

where $\Omega_{0,1}$ is static spin matrix element, $F_{ij}(u)$ is the spin structure functions, $u = M_A b^2 E_R$ is a dimensionless variable given as a function of the recoil energy and b is the nuclear harmonic-oscillator size parameter given in eq. 3.2.18 which is $b = 2.2872\text{fm}$ for ^{129}Xe , and $b = 2.2923\text{fm}$ for ^{131}Xe .

The static spin matrix elements and the spin expectation values for elastic interactions with a detailed derivation are given in ref. [98] are summarized in Table 3.2.

Table 3.2: Static spin matrix elements (Ω_i) calculated with effective g -factors, ground state spin expectation values ($\langle S_i \rangle$) and total nuclear spin (J) for ^{129}Xe and ^{131}Xe isotopes (CD-Bonn G-matrix calculation - J. Suhonen et.al [98])

	^{129}Xe	^{131}Xe
J	1/2	3/2
$\langle S_p \rangle$	-0.0019	-0.00069
$\langle S_n \rangle$	0.273	-0.125
Ω_0	0.831	-0.286
Ω_1	-0.838	0.284

In previous analysis the used Spin expectation values ($\langle S_{p,n} \rangle$) were calculated using Bonn-A [101] and Nijment II [102] potentials. For ^{129}Xe the magnetic moment agrees within 19% (for the Bonn-A potential), and 52% (for the Nijmegen II potential). The analysis was done using both potentials to estimate the systematic uncertainty associated with using different models (see table 3.3 for detailed comparison for different models and Figure 3.4.2 for comparison of form-factors and 3.4.5b for comparison of differential rate). Current variables were calculated by J. Suhonen et.al [98] by shell model code 'eicode' [103], using effective nucleon-nucleon interactions based on the CD-Bonn G-matrix [104, 101]. The 1-2% agreement with the magnetic moment (using effective g factors) is significantly better than the previous spin structure functions.

For the ^{131}Xe isotope Bonn-A and Nijmegen II potentials agree within 8% and 50% with the measured value of magnetic moment. However, there are additional calculations done by J. Engel using the quasi-particle Tamm-Dancoff approximation (QTDA) [95] which yield a magnetic moment within 1% of the experimental value ⁸.

The Form Factors in the previous analysis were taken from [100] where a six-order polynomials were used. The comparison to the previous parametrization is shown in Figure 3.4.2. We

⁸It has to be borne in mind that J. Suhonen have used a global fit of the g -factors to an extensive set of magnetic moments and obtain an excellent agreement with the measured magnetic moments. Such a global fit is not done in Engel's calculation [105]

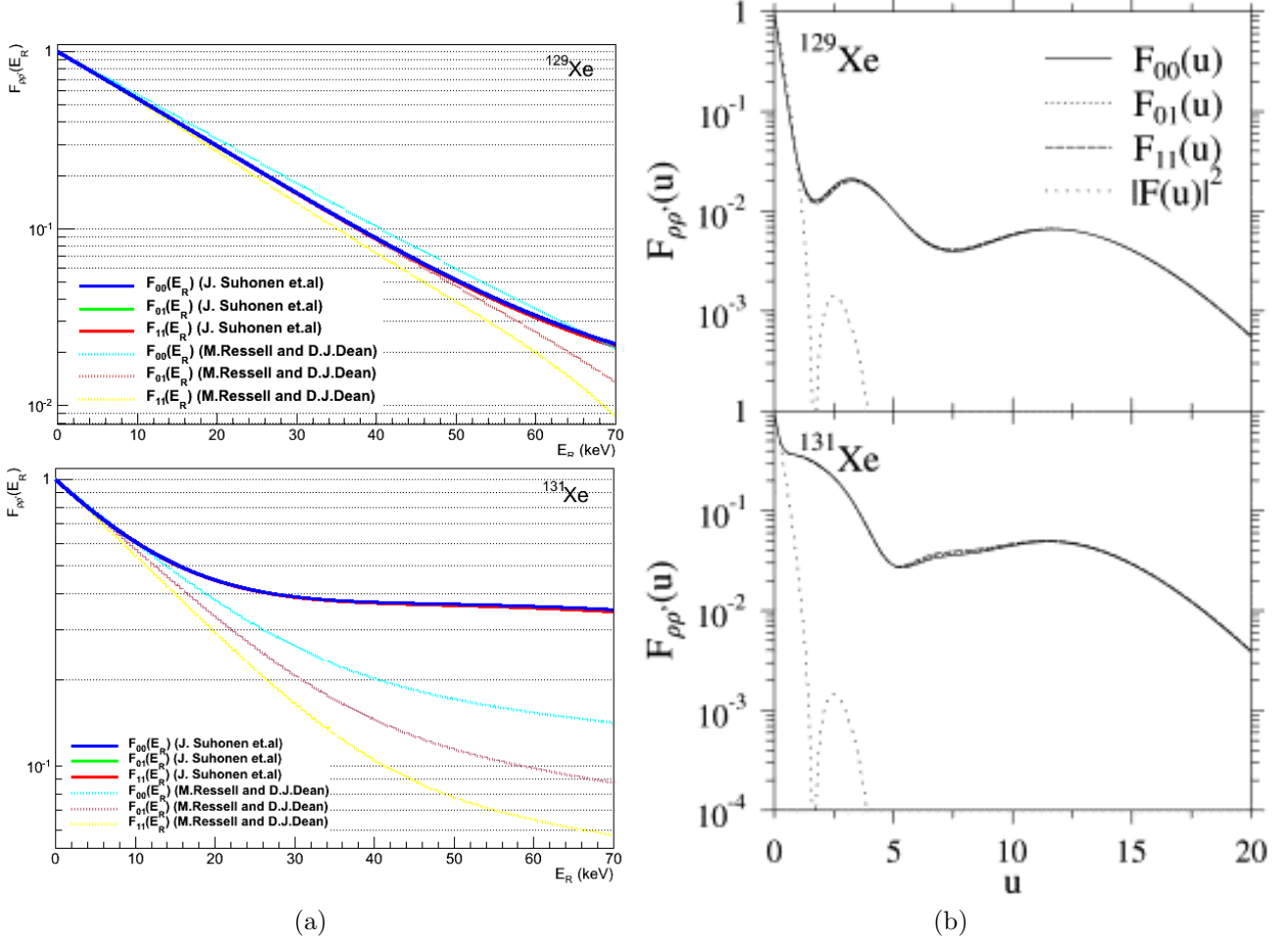


Figure 3.4.1: Form Factors for ^{129}Xe and ^{131}Xe isotopes:

(a) Comparison between form factors using parametrization from previous (M.T. Ressel and D.J. Dean [100] - dashed line) and this (J. Suhonen et al. [98]) analysis. ($E_R = 70\text{keV}$ at $u \cong 1.15$).

(b) Spin structure function $F_{\rho\rho'}(u)$ for elastic WIMP-nucleus scattering, that has been used in this analysis taken from ref. [98].

can see from Figure 3.4.5b and Table 3.3 that the change in the spin expectation values have the dominant impact on the differential rate calculation. For ^{129}Xe ⁹ the squared ratio between the spin parameters is $\left(\frac{\langle S_n^{\text{old}} \rangle}{\langle S_n^{\text{new}} \rangle}\right)^2 \approx 1.73$ for neutrons and $\left(\frac{\langle S_p^{\text{old}} \rangle}{\langle S_p^{\text{new}} \rangle}\right)^2 \approx 217$ for protons (!). Recall from equation 3.4.1 that the differential cross section in SD interaction $\sigma \propto \langle S_{n,p} \rangle^2$, thus the 2 order of magnitude in the square ratio for proton interactions leads to high discrepancy between previous and this analysis in pure proton limit. However, since the pure WIMP-proton interaction is depressed due to the even-proton number of the nuclei, this high difference doesn't play a major role in WIMP-nucleon interactions. It is interesting to note that the form-factor for pure proton interaction increases with the recoil energy, to values that are larger than one. It is probably associated to collective nuclear-structure effect: the scattering is not from one isolated nucleon, and it becomes a coherent effect of many nucleons for certain scattering energies. Somehow the many-particle shell-model wave functions enhance the collective effects for

⁹For ^{131}Xe using QTDA the proton spin expectation values differs in 3 order of magnitude compare to this analysis, so all comparison of differential rate were made using Bonn-A potential

Table 3.3: Spin expectation values and total nuclear spin for ^{129}Xe and ^{131}Xe isotopes for Bonn-A and Nijmegen II potentials and QTDA with comparison to current parameters

	^{129}Xe		^{131}Xe	
	$\langle S_p \rangle$	$\langle S_n \rangle$	$\langle S_p \rangle$	$\langle S_n \rangle$
Bonn-A	0.028	0.359	-0.009	-0.227
Nijmegen II	0.0128	0.300	-0.012	-0.217
QTDA	-	-	-0.041	-0.236
J. Suhonen et.al	-0.0019	0.273	-0.00069	-0.125

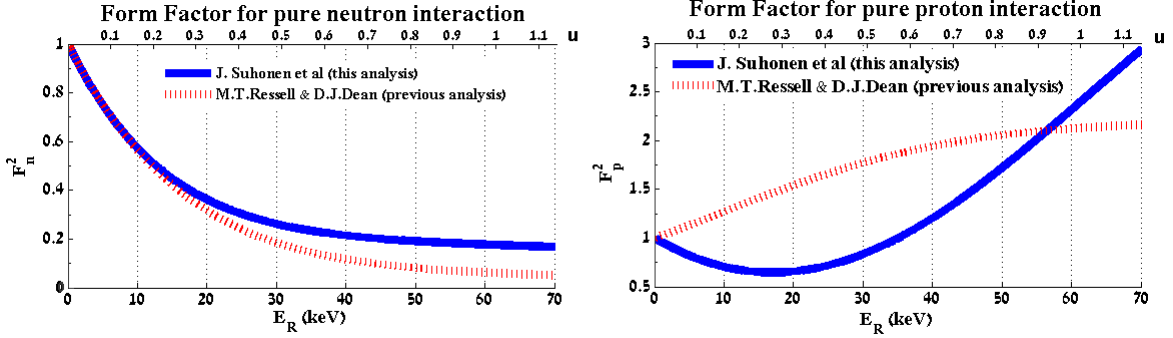


Figure 3.4.2: Comparison for combined Form-Factor $\left(\frac{\sum_A \omega_A F_A^2(q^2)}{\sum_A \omega_A} \right)$ for pure-neutron and pure proton interactions for previous and this analysis (parameter u has been chosen for $A=130$). $M_D = 100\text{GeV}$, $\sigma_{n,p}^0 = 1\text{pb}$.

protons [105].

Using the new nuclear parameters, the cross section is calculated as a function of recoil energy, and the differential rate can be obtained using equation (3.2.10) as a function of the recoil energy.

3.4.3 Systematic unc. from velocity distribution

The WIMP's velocity distribution directly effects the rate calculation, and uncertainty on it may cause systematic effects on the expected rate. The systematic effect from velocity distribution was calculated, and shown here:

Earth velocity correction Due to annual modulations the correction to the earth velocity is $v_E + 15 \cos \omega(t - t_0)$ km/sec, where $\omega = 2\pi/\text{year}$ and $t_0 \cong \text{June 2nd}$ [88]. The systematic effect on the differential rate calculation is negligible. The Fraction of the rate - $\frac{\frac{dR}{dE_R}(v_E=220 \pm 15 \frac{\text{km}}{\text{sec}})}{\frac{dR}{dE_R}(v_E=220 \frac{\text{km}}{\text{sec}})}$ is shown in Figure (3.4.4).

Earth velocity correction effect few percent on the differential rate, and averaged out by integrating over the recoil energy. In a presence of null signal the systematic correction due to earth velocity modulation is negligible.

Escape velocity correction The escape velocity lies within the range $498 \frac{\text{km}}{\text{sec}} < v_{esc} < 608 \frac{\text{km}}{\text{sec}}$ (90%CL) [91], in our calculation we set the escape velocity to be the median likelihood value of $v_{esc} = 544 \pm 33 \frac{\text{km}}{\text{sec}}$ for systematic uncertainty. The systematic uncertainty from the escape velocity found to be small - less than 1% and is shown in Figure 3.4.5.

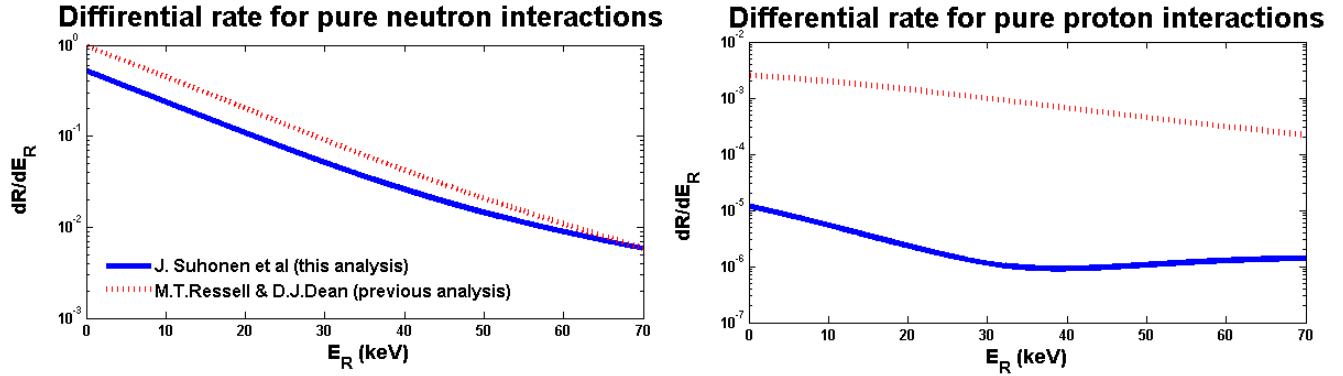


Figure 3.4.3: Comparison of weighted differential rate $\left(\sum_A \omega_A \frac{dR_A}{dE} / \sum_A \omega_A \right)$ for pure-neutron and pure-proton interactions between this and previous parametrization (old spin exp. values were calculated using Born A potentials). $M_D = 100\text{GeV}$, $\sigma_{n,p}^0 = 1\text{pb}$.

3.4.4 Results

Cross section limit plot Using the methodology in section 3.2, we can calculate the expected event rate using the WIMP-nucleon zero momentum transfer cross section and set a limit on the cross section based on the sensitivity of the experiment. The Profile Likelihood (PL) method [106]) was used to calculate the cross section limit plots as a function of WIMP mass. The plots are shown in figure 3.4.6. Limits using new and old nuclear parameters are shown in the plots, we can see that the new pure proton limit is defers ≈ 3 order of magnitude due to different spin expectation values.

3.4.5 Summary

The analysis of 100.9 live days science data acquired during 2010. In the absence of significant signal, an upper limit on the spin-dependent WIMP-nucleon interactions have been derived. The most stringent limit on pure neutron spin-dependent dark matter interactions is obtained excluding previously unexplored region of WIMP parameter space.

It has been found that the nuclear model adopted in the analysis has a significant impact on the sensitivity. To be conservative, we adopt the J. Suhonen [98] nuclear model. Cross-sections above $5.88 \times 10^{-40}\text{cm}^2$ for a WIMP mass of $42\text{GeV}/c^2$ are excluded at 90% confidence level.

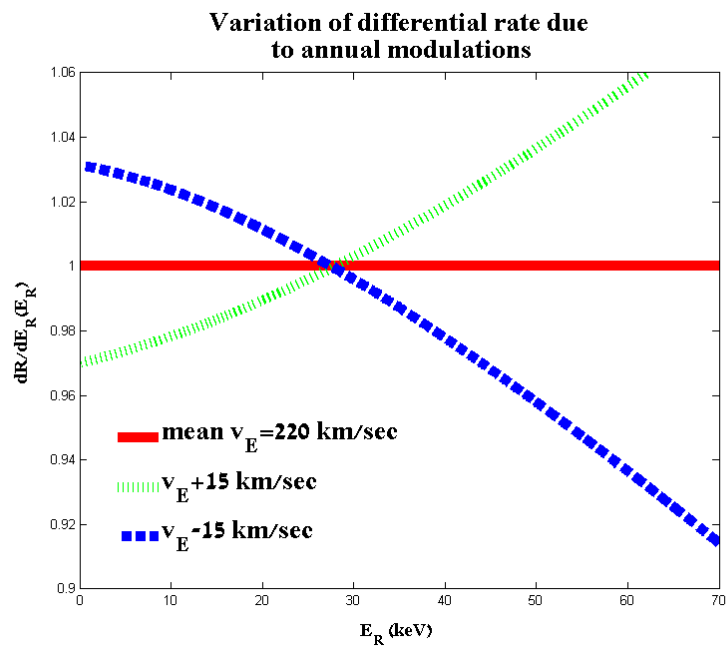


Figure 3.4.4: Fraction between rates for $\sigma_n^0 = 1pb$ and $M_D = 100GeV/c^2$

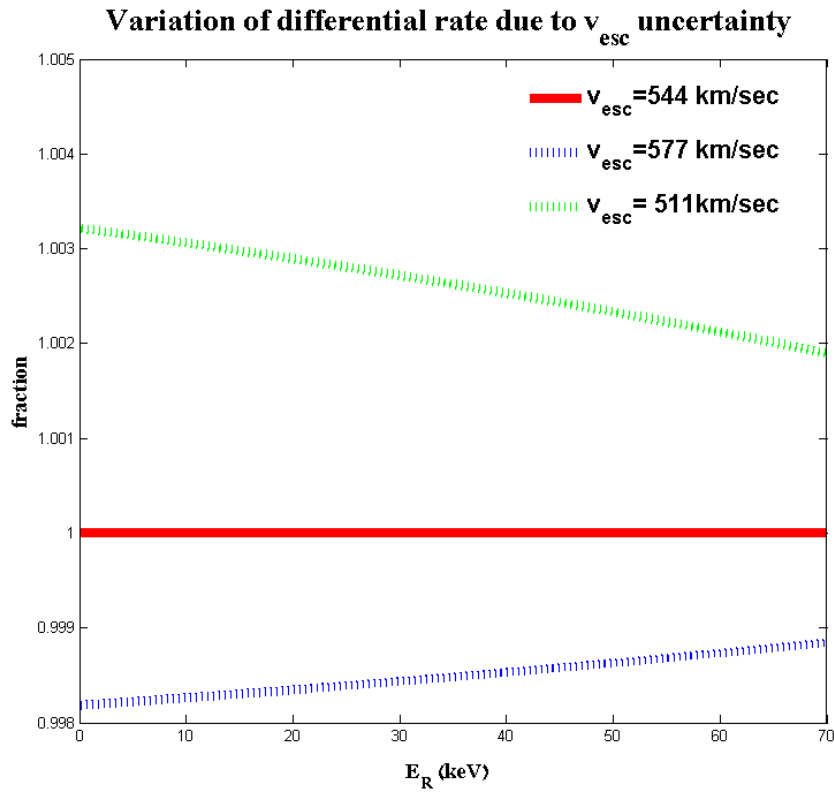
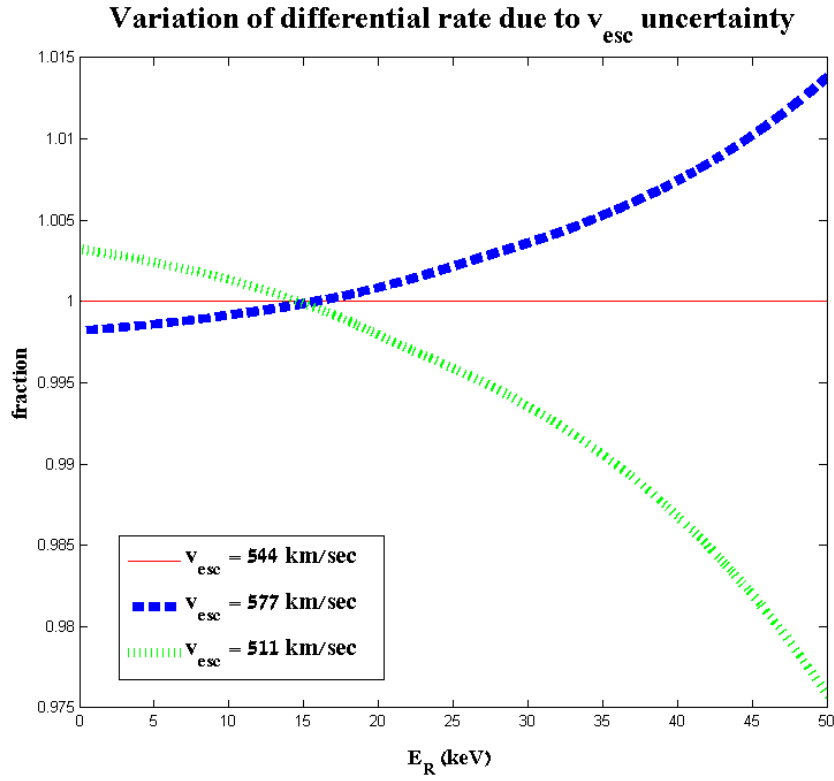


Figure 3.4.5: Fraction $\frac{\frac{dR}{dE_R}(v_{esc}=544 \pm 33 \frac{km}{sec})}{\frac{dR}{dE_R}(v_{esc}=544 \frac{km}{sec})}$ for $\sigma_n^0 = 1pb$ and (a) $M_D = 50 GeV/c^2$; (b) $M_D = 1000 GeV/c^2$

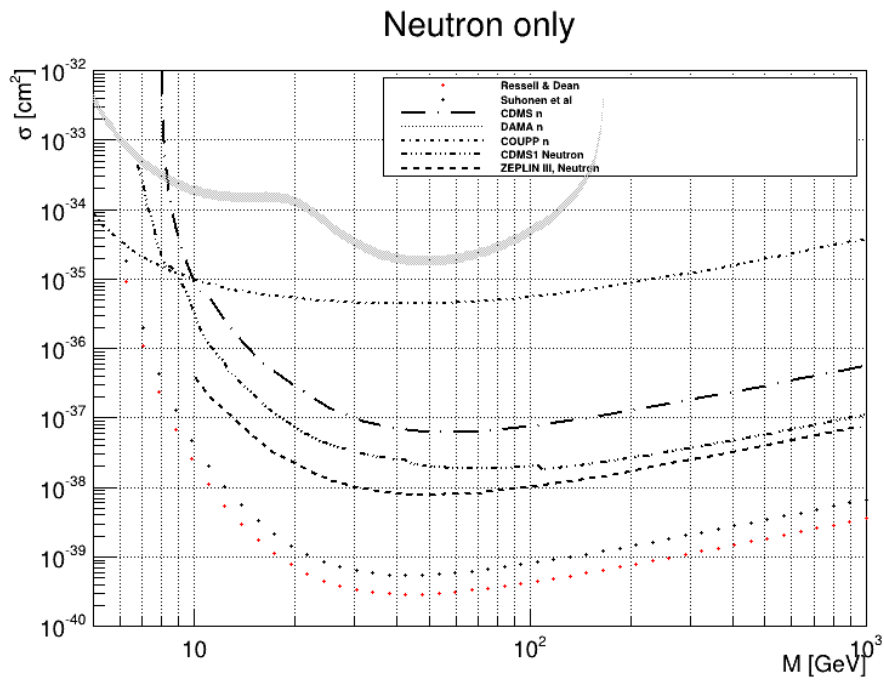
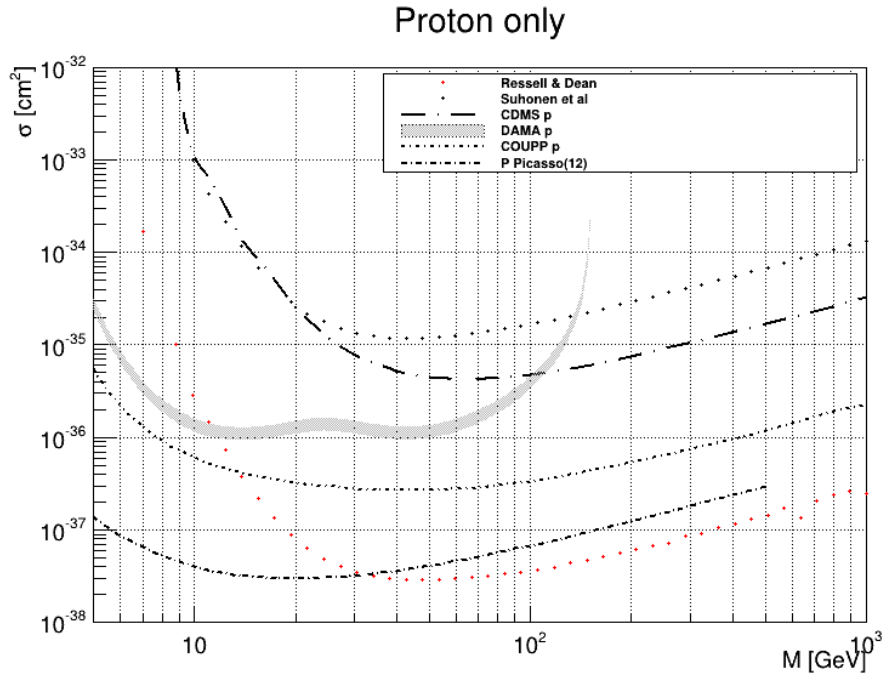


Figure 3.4.6: SD limit plot for (a) pure neutron and (b) pure proton interactions. For Xenon using both nuclear spin parameters and compared to DAMA allowed region, PICASSO [107] and CDMSII limits [86]

List of Figures

1.1.1 Schematic layout of ILC	3
1.1.2 Illustration of a quadrant of SiD	3
1.1.3 Schematic of the RPC	4
1.1.4 Schematic view of MICROMEAS	5
1.1.5 A schematic drawing of the GEM	6
1.1.6 GEM DHCAL Concept	7
1.1.7 Schematic view of the detector with three GEM foils	7
1.1.8 Photograph of typical THGEM electrode and scheme of operation principle	8
1.1.9 THGEM operation principle (GARFIELD simulation)	9
1.1.10 THGEM gain curves for Ne and Ne-CH ₄ mixtures	10
1.2.1 Single- and double-THGEM configurations	11
1.2.2 Charge distribution of muons recorded with a single-THGEM detector and the muon detection efficiency	12
1.2.3 Landau distributions of muons and pions for double-THGEM	13
1.2.4 Landau distributions with a single-THGEM	14
1.2.5 Landau distribution with the RWELL	15
1.3.1 Schematic drawing of the THWELL structure	16
1.3.2 Experimental setup	16
1.3.3 Measured spectra with one/two Cu targets	17
1.3.4 Gain curves for the THWELL and induction-gap configuration	17
1.3.5 Electric field inside the THGEM holes along the central axis	18
1.3.6 Townsend coefficient for Neon/CH ₄ 95:5%	18
1.3.7 Weighting field (\mathbf{E}_w) in the THWELL and induction-gap configurations	20
1.3.8 Signal shapes from the THWELL and induction-gap configurations	21
1.3.9 Ion Drift time	22
1.3.10 Current pulse from I_{MON} during a spark	22
1.3.11 Discharge probability vs gain: THWELL and regular THGEM	23
1.4.1 Resistive WELL configuration	24
1.4.2 Gain curves for THWELL, 10 M Ω /□ RWELL and regular THGEM	25
1.4.3 Pulse shapes for THWELL and RWELL.	25
1.4.4 Discharge probability for the THWELL, RWELL and regular THGEM	26
1.4.5 Rate dependence of the gain in the 10 M Ω /□ RWELL.	27
1.4.6 Schematic of charge dispersion in RWELL	28
1.4.7 Simulation of the charge diffusion on the surface of resistive layer	29
1.4.8 Experimental setup for charge dispersion measurements.	30
1.4.9 Measured signal for neighbor pads	30
1.4.10 Signal propagation measurement	31
1.4.11 Neighbor pad signal amplitude	32
1.5.1 Segmented-GRWELL	33
1.5.2 A segmented-GRWELL layout	33

1.5.3 Field lines and drift of the electrons for $E_{DRIFT}=0.2,1\text{kV/cm}$	34
1.5.4 Effective volume above the band	34
1.5.5 Collection efficiency Simulation	35
1.5.6 Diffusion coefficients for Ne/CH ₄ (5%) mixture	36
1.5.7 Transparency measurement	36
1.6.1 Semi-resistive THCOBRA detector	38
2.1.1 Higgs decay BR and width	41
2.2.1 LHC integrated luminosity	43
2.2.2 The ATLAS detector	44
2.4.1 Higgs production mechanism at the LHC	48
2.4.2 SM Higgs production cross section	48
2.5.1 Distributions of Effective and Visible mass	52
2.5.2 Collinear mass distribution vs $\Delta\phi$ cut	53
2.5.3 Probability distribution functions $\mathcal{P}(\Delta R, \mathbf{p}_\tau)$	55
2.5.4 Reconstruction resolution	56
2.6.1 Scheme of τ lepton decay kinematics	57
2.6.2 Distribution of $\mathcal{P}(\theta)$	57
2.6.3 Distribution of ΔR in forward and central regions	58
2.6.4 Distribution $\mathcal{P}(\cos\theta, m_{miss})$ for unbiased τ decay (no cuts)	59
2.6.5 Distributions of $\cos\theta^*$ distribution vs lepton p_T cut.	61
2.6.6 MMC performance: MET ideal vs. reconstructed	62
2.6.7 Missing energy correction	62
2.7.1 Comparison between old and new MMC	63
2.7.2 A comparison between the MMC and the collinear mass	64
2.7.3 MMC separation	64
3.1.1 Current mass Energy Distribution of the Universe	65
3.3.1 XENON100 TPC scheme	71
3.4.1 Form Factors ($F_{\rho\rho'}(q)$) for different NN potential models	73
3.4.2 Comparison for combined FF	74
3.4.3 Comparison between differential rates using different NN potentials	75
3.4.4 Annual modulation systematics	76
3.4.5 Escape velocity uncertainty	77
3.4.6 SD limit	78

List of Tables

1.1	Spark charge and spark and signal fraction at the anode measured with the THWELL and induction gap configurations	23
2.1	Gauge bosons in the Standard Model	45
2.2	Fermionic content of the SM	45
2.3	Cross-sections for various background channels	49
3.1	Natural (NA) abundance of Xenon isotopes	70
3.2	Static spin matrix elements (Ω_i) calculated with effective g -factors, ground state spin expectation values ($\langle S_i \rangle$) and total nuclear spin (J) for ^{129}Xe and ^{131}Xe isotopes (CD-Bonn G-matrix calculation - J. Suhonen et.al [98])	72
3.3	Spin expectation values and total nuclear spin for ^{129}Xe and ^{131}Xe isotopes for Bonn-A and Nijmegen II potentials and QTDA with comparison to current parameters	74

Bibliography

- [1] James Brau, Yasuhiro Okada, and Nicholas Walker. Ilc reference design report volume 1 - executive summary, 2007. [2](#)
- [2] M. Oreglia H. Aihara, P. Burrows. SiD Letter of Intent. *Letter of Intent for SiD detector concept presented to ILC IDAG*, 2009. [2](#), [3](#), [4](#), [7](#)
- [3] M.A. and Thomson. Particle flow calorimetry and the pandorapfa algorithm. *Nuclear Instruments and Methods in Physics Research Section A: Accelerators, Spectrometers, Detectors and Associated Equipment*, 611(1):25 – 40, 2009. [2](#), [4](#)
- [4] Ugo Amaldi. Fluctuations in calorimetry measurements. *Physica Scripta*, 23(4A):409, 1981. [4](#)
- [5] R. Santonico and R. Cardarelli. Development of resistive plate counters. *Nuclear Instruments and Methods in Physics Research*, 187(23):377 – 380, 1981. [4](#), [9](#), [24](#)
- [6] Jose Repond. Analysis of dhcal muon events. In *TIPP 2011 Conference, Chicago, June 9 - 14, 2011*. [4](#), [6](#)
- [7] Y. Giomataris, Ph. Rebourgeard, J.P. Robert, and G. Charpak. MICROMEGAS: a high-granularity position-sensitive gaseous detector for high particle-flux environments. *Nuclear Instruments and Methods in Physics Research Section A: Accelerators, Spectrometers, Detectors and Associated Equipment*, 376(1):29 – 35, 1996. [4](#), [5](#)
- [8] C. Adloff et al. Recent results of micromegas sdhcal with a new readout chip. [5](#), [6](#)
- [9] Fabio Sauli and Archana Sharma. MICROPATTERN GASEOUS DETECTORS. *Annual Review of Nuclear and Particle Science*, 49(1):341–388, 1999. [6](#)
- [10] B. Ketzer et al. Triple GEM tracking detectors for COMPASS. *Nuclear Science, IEEE Transactions on*, 49(5):2403 – 2410, oct 2002. [5](#)
- [11] J. Yu et al. Development of large area gem chambers. 1999. [6](#)
- [12] P. Jeanneret. *Time Projection Chambers and detection of neutrinos*. PhD thesis, Neuchâtel University, 2001. [6](#)
- [13] R. Chechik, A. Breskin, C. Shalem, and D. Mormann. Thick GEM-like hole multipliers: properties and possible applications. *Nuclear Instruments and Methods in Physics Research Section A: Accelerators, Spectrometers, Detectors and Associated Equipment*, 535(12):303 – 308, 2004. [6](#)
- [14] M Cortesi, R Alon, R Chechik, A Breskin, D Vartsky, and V Dangendorf. Investigations of a thgem-based imaging detector. *Journal of Instrumentation*, 2(09):P09002, 2007. [6](#), [32](#)

- [15] R. Chechik, M. Cortesi, A. Breskin, D. Vartsky, D. Bar, and V. Dangendorf. Thick GEM-like (THGEM) detectors and their possible applications. *ECONF0604032*, 0025, 2006. 6
- [16] A. Breskin et al. A concise review on THGEM detectors. *Nuclear Instruments and Methods in Physics Research Section A: Accelerators, Spectrometers, Detectors and Associated Equipment*, 598(1):107 – 111, 2009. 7, 8
- [17] A. Breskin et al. CsI-THGEM gaseous photomultipliers for RICH and noble-liquid detectors. *Nuclear Instruments and Methods in Physics Research Section A: Accelerators, Spectrometers, Detectors and Associated Equipment*, 639(1):117 – 120, 2011. 8
- [18] GARFIELD 9. Simulation of gaseous detectors. <http://garfield.web.cern.ch/garfield/>. 9, 34
- [19] C.K. Shalem, R. Chechik, A. Breskin, and K. Michaeli. Advances in Thick GEM-like gaseous electron multipliers. Part I: atmospheric pressure operation. *NUCL.INSTRUM.METH.A*, 558:475, 2006. 7, 9
- [20] C.K. Shalem, R. Chechik, A. Breskin, K. Michaeli, and N. Ben-Haim. Advances in thick GEM-like gaseous electron multipliers Part II: Low-pressure operation. *Nuclear Instruments and Methods in Physics Research Section A: Accelerators, Spectrometers, Detectors and Associated Equipment*, 558(2):468 – 474, 2006. 7
- [21] R. Chechik, A. Breskin, and C. Shalem. Thick GEM-like multipliers a simple solution for large area UV-RICH detectors. *Nuclear Instruments and Methods in Physics Research Section A: Accelerators, Spectrometers, Detectors and Associated Equipment*, 553(12):35 – 40, 2005. 7
- [22] M. Cortesi et al. THGEM operation in Ne and Ne/CH₄. *JINST*, 4:08001, 2009. 7, 8, 9, 10
- [23] F. Bartol, M. Bordessoule, G. Chaplier, M. Lemonnier, and S. Megtert. The C.A.T. Pixel Proportional Gas Counter Detector. *J. Phys. III France*, 6(3):337–347, 1996. 8
- [24] R Bellazzini et al. The well detector. *Nuclear Instruments and Methods in Physics Research Section A: Accelerators, Spectrometers, Detectors and Associated Equipment*, 423(1):125 – 134, 1999. 8
- [25] H. Cho et al. Operating Characteristics of Open and Closed-End Gas Electron Multipliers. *Journal of the Korean Physical Society, Detectors and Associated Equipment*, 42(1):56 – 59, 2003. 8
- [26] M. Alfonsi et al. Performance Measurements on closed geometry GEM-like detectors. *MPGD2009 - Crete, the 12th of June 2009*. 8
- [27] *Electron avalanches and breakdown in gases*. Butterworths, London U.K., 1964. 8
- [28] P.Fonte V.Peskov. Research on discharges in micropattern and small gap gaseous detectors. Technical report, RD51 collaboration, 2009. 8
- [29] A.A. et al. Aarts. Discharge Protection and Ageing of Micromegas Pixel Detectors,. In *Nuclear Science Symposium Conference Record, 2006. IEEE*. 9

- [30] P. Fonte. A new type of spark-protected parallel mesh chamber. *Nucl. Instr. and Methods in Phys. Res.* **9**
- [31] RuiRui Fan et al. Micromegas with resistive anode. In *Nuclear Science Symposium Conference Record (NSS/MIC), 2009 IEEE*, pages 690 –693, Nov 2009. **9**
- [32] C D R Azevedo et al. Towards THGEM UV-photon detectors for RICH: on single-photon detection efficiency in Ne/CH₄ and Ne/CF₄. *Journal of Instrumentation*, 5(01):P01002, 2010. **9**
- [33] F. Sauli. *Principles of operation of multiwire proportional and drift chambers*. CERN (Series). CERN, 1977. **10, 16, 17, 19**
- [34] M. Alfonsi. RD51 GEM Telescope: results from June 2010 test beam and work in progress. *RD51 Miniweek, July 20th, 2010*. **10**
- [35] K. Karakostas et al. Micromegas telescope for the RD51 Test Beams. *XXVIII Workshop on Recent Advances in Particles Physics and Cosmology*, 26 March 2010. **10**
- [36] K. Karakostas et al. A slow control system for RD51 test facilities. *RD51 Note Number: 2011-011*. **10**
- [37] D. et al. Freytag. Kpix, an array of self triggered charge sensitive cells generating digital time and amplitude information. *IEEE Nucl. Sci. Symp. Conf. Rec.*, 2008. **10**
- [38] MAXWELL 3D. Ansoft co. pittsburg. PA, USA. **16, 20**
- [39] Magboltz 7. Transport of electrons in gas mixtures. <http://magboltz.web.cern.ch/magboltz/>. **18, 19, 34**
- [40] S. Ramo. Currents Induced by Electron Motion. *Proceedings of the IRE*, 27(9):584 – 585, sept. 1939. **19**
- [41] Glenn F. Knoll. *Radiation Detection and Measurement*. Wiley, 4 edition, 2010. **19**
- [42] H. J. Oskam and V. R. Mittelstadt. Ion Mobilities in Helium, Neon, and Argon. *Phys. Rev.*, 132:1435–1444, Nov 1963. **19**
- [43] M.S. Dixit and A. Rankin. Simulating the charge dispersion phenomena in Micro Pattern Gas Detectors with a resistive anode. *Nuclear Instruments and Methods in Physics Research Section A: Accelerators, Spectrometers, Detectors and Associated Equipment*, 566(2):281 – 285, 2006. **24**
- [44] Vladimir Smakhtin et al. Position resolution and efficiency measurements with large scale Thin Gap Chambers for the super LHC. *Nuclear Instruments and Methods in Physics Research Section A: Accelerators, Spectrometers, Detectors and Associated Equipment*, 628(1):177 – 181, 2011. **24**
- [45] G. Battistoni, P. Campana, V. Chiarella, U. Denni, E. Iarocci, and G. Nicoletti. Resistive cathode transparency. *Nuclear Instruments and Methods in Physics Research*, 202(3):459 – 464, 1982. **25**

- [46] C Iacobaeus et al. The development and study of high-position resolution ($50\mu\text{m}$) RPCs for imaging X-rays and UV photons. *Nuclear Instruments and Methods in Physics Research Section A: Accelerators, Spectrometers, Detectors and Associated Equipment*, 513(12):244 – 249, 2003. 26
- [47] S Duval et al. On the operation of a micropattern gaseous UV-photomultiplier in liquid-Xenon. *Journal of Instrumentation*, 6(04):P04007, 2011. 26
- [48] M.S. Dixit, J. Dubeau, J.-P. Martin, and K. Sachs. Position sensing from charge dispersion in micro-pattern gas detectors with a resistive anode. *Nuclear Instruments and Methods in Physics Research Section A: Accelerators, Spectrometers, Detectors and Associated Equipment*, 518(3):721 – 727, 2004. 26
- [49] J.F.C.A. Veloso, C.A. Santos, F. Pereira, C.D.R. Azevedo, F.D. Amaro, J.M.F. dos Santos, A. Breskin, and R. Chechik. Thcobra: Ion back flow reduction in patterned thgem cascades. *Nuclear Instruments and Methods in Physics Research Section A: Accelerators, Spectrometers, Detectors and Associated Equipment*, 639(1):134 – 136, 2011. 37, 38
- [50] LHC Higgs Cross Section Working Group, S. Dittmaier, C. Mariotti, G. Passarino, and R. Tanaka (Eds.). Handbook of LHC Higgs Cross Sections: 1. Inclusive Observables. *CERN-2011-002*, CERN, Geneva, 2011. 40, 41, 48
- [51] CMS Collaboration. Combined result of searches for the standard model Higgs boson in pp collisions at $\sqrt{s} = 7$ TeV. *CERN-PH-EP-2012-023*, CERN, Geneva, 2011. 40
- [52] ATLAS Collaboration. Combined search for the standard model higgs boson using up to 4.9 fb^{-1} of pp collision data at $\sqrt{s} = 7$ tev with the ATLAS detector at the LHC. *Physics Letters B*, 710(1):49 – 66, 2012. 40
- [53] Search for the Standard Model Higgs boson in the $H \rightarrow \tau^+\tau^-$ decay mode with 4.7 fb^{-1} of ATLAS data at $\sqrt{s}=7$ tev. Technical Report ATLAS-CONF-2012-014, CERN, Geneva, Mar 2012. 41
- [54] A. Elagin, P. Murat, A. Pranko, and A. Safonov. A new mass reconstruction technique for resonances decaying to $\tau\tau$. *Nuclear Instruments and Methods in Physics Research Section A: Accelerators, Spectrometers, Detectors and Associated Equipment*, 654(1):481 – 489, 2011. 41, 54, 55, 56
- [55] Lyndon Evans and Philip Bryant. Lhc machine. *Journal of Instrumentation*, 3(08):S08001, 2008. 42
- [56] E. Eichten, I. Hinchliffe, K. Lane, and C. Quigg. Supercollider physics. *Rev. Mod. Phys.*, 56:579–707, Oct 1984. 42
- [57] The ATLAS Collaboration. The ATLAS Experiment at the CERN Large Hadron Collider. *Journal of Instrumentation*, 3(08):S08003, 2008. 42, 44
- [58] *Gauge theory of elementary particle physics*. Oxford University Press, 1984. 45
- [59] K Nakamura and Particle Data Group. Review of particle physics. *Journal of Physics G: Nuclear and Particle Physics*, 37(7A):075021, 2010. 45, 57
- [60] Peter W. Higgs. Broken Symmetries and the Masses of Gauge Bosons. *Phys. Rev. Lett.*, 13:508–509, Oct 1964. 46

- [61] D. Rainwater, D. Zeppenfeld, and K. Hagiwara. Searching for $h \rightarrow \tau\tau$ in weak boson fusion at the cern lhc. *Phys. Rev. D*, 59:014037, Dec 1998. 48, 51
- [62] S. et al. Asai. Prospects for the search for a standard model higgs boson in atlas using vector boson fusion. *The European Physical Journal C - Particles and Fields*, 32:s19–s54, 2004. 10.1140/epjcd/s2003-01-010-8. 48, 51
- [63] B. Mellado, W. Quayle, and Sau Lan Wu. Prospects for the observation of a higgs boson with associated with one high jet at the lhc. *Physics Letters B*, 611:60 – 65, 2005. 48, 51
- [64] E Barberio, K Bierwagen, U Blumenschein, T Bristow, X Chen, A Ferrer, L Fiorini, C Gumpert, K Hanawa, Y Hernandez, J Kroseberg, B Mellado, K Mochizuki, Y Pan, S Psoroulas, T Schwindt, T Shao, O Silbert, C Solans, J Valls, T Vickey, and Y Zhu. Search for the standard model higgs boson in the decay mode $H \rightarrow \tau^+\tau^- \rightarrow \ell\ell + 4\nu$ in proton-proton collisions at $\sqrt{s}=7$ tev with the atlas detector. Technical Report ATL-COM-PHYS-2011-1611, CERN, Geneva, Mar 2012. 49
- [65] The ATLAS Collaboration. Measurement of the $w \rightarrow l\nu$ and $z/\gamma^* \rightarrow ll$ production cross sections in proton-proton collisions at $\sqrt{s} = 7$ tev with the atlas detector. *Journal of High Energy Physics*, 2010, 2010. 10.1007/JHEP12(2010)060. 50
- [66] The ALTAS Collabiration. *Expected performance of the ATLAS experiment: detector, trigger and physics*. CERN, Geneva, 2009. 50
- [67] Matteo Cacciari, Gavin P. Salam, and Gregory Soyez. The anti- k_t jet clustering algorithm. *Journal of High Energy Physics*, 2008(04):063, 2008. 50
- [68] The ATLAS Collaboration. Performance of missing transverse momentum reconstruction in proton-proton collisions at $\sqrt{s} = 7$ TeV with ATLAS detector. *The European Physical Journal C - Particles and Fields*, 72:1–35, 2012. 10.1140/epjc/s10052-011-1844-6. 50
- [69] R.K. Ellis, I. Hinchliffe, M. Soldate, and J.J. Van Der Bij. Higgs decay to $\pi^+\pi^-$: A possible signature of intermediate mass higgs bosons at high energy hadron colliders. *Nuclear Physics B*, 297(2):221 – 243, 1988. 51, 52
- [70] O. Silbert et al. Modified MMC. *ATLAS: HSG4 group meeting*, 24 May 2011. 58
- [71] P. Beckmann. *A history of [pi] (pi)*. St. Martin’s Press, 1971. 60
- [72] G. Cardano. *Artis Magnæ, Sive de Regulis Algebraicis Liber*. 1545. 60
- [73] N. Jarosik et al. Seven-year Wilkinson Microwave Anisotropy Probe (WMAP) Observations: Sky Maps, Systematic Errors, and Basic Results. *The Astrophysical Journal Supplement Series*, 192(2):14, 2011. 65, 66
- [74] G R Blumenthal, S M Faber, J R Primack, and M J Rees. Formation of galaxies and large-scale structure with cold dark matter. *Nature*, 311(5986):517–525, 1984. 65
- [75] V. C. Rubin, W. K. J. Ford, and N. . Thonnard. Rotational properties of 21 SC galaxies with a large range of luminosities and radii, from NGC 4605 /R = 4kpc/ to UGC 2885 /R = 122 kpc/. *Astrophysical Journal*, 238:471–487, June 1980. 66
- [76] Fritz Zwicky. Luminous and dark formations of intergalactic matter. *Physics Today*, 6(4):7–11, 1953. 66

- [77] Marisa Girardi, Giuliano Giuricin, Fabio Mardirossian, Marino Mezzetti, and Walter Boschin. Optical mass estimates of galaxy clusters. *The Astrophysical Journal*, 505(1):74, 1998. 66
- [78] Albert Einstein. LENS-LIKE ACTION OF A STAR BY THE DEVIATION OF LIGHT IN THE GRAVITATIONAL FIELD. *Science*, 84(2188):506–507, 1936. 66
- [79] Raphael Gavazzi et al. The Sloan Lens ACS Survey. IV. The Mass Density Profile of Early-Type Galaxies out to 100 Effective Radii. *The Astrophysical Journal*, 667(1):176, 2007. 66
- [80] A. A. Penzias and R. W. Wilson. A Measurement of Excess Antenna Temperature at 4080 Mc/s. *Astrophysical Journal*, 142:419–421, July 1965. 66
- [81] Noterdaeme, P., Petitjean, P., Srianand, R., Ledoux, C., and López, S. The evolution of the cosmic microwave background temperature. *A&A*, 526:L7, 2011. 66
- [82] R. Bernabei et al. New results from DAMA/LIBRA. *The European Physical Journal C - Particles and Fields*, 67:39–49, 2010. 10.1140/epjc/s10052-010-1303-9. 67
- [83] J. I. Collar et al. Search for an Annual Modulation in a p -Type Point Contact Germanium Dark Matter Detector. *Phys. Rev. Lett.*, 107:141301, Sep 2011. 67
- [84] E. Aprile et al. Dark Matter Results from 100 Live Days of XENON100 Data. *Phys. Rev. Lett.*, 107:131302, Sep 2011. 67, 71
- [85] E. Aprile et al. Limits on Spin-Dependent WIMP-Nucleon Cross Sections from the XENON10 Experiment. *Phys. Rev. Lett.*, 101:091301, Aug 2008. 67
- [86] Z. Ahmed et al. Results from a Low-Energy Analysis of the CDMS II Germanium Data. *Phys. Rev. Lett.*, 106:131302, Mar 2011. 67, 78
- [87] Kfir Blum. DAMA vs. the annually modulated muon background. *arXiv:1110.0857v1 [astro-ph.HE]*, Oct 2011. 67
- [88] J.D. Lewin and P.F. Smith. Review of mathematics, numerical factors, and corrections for dark matter experiments based on elastic nuclear recoil. *Astroparticle Physics*, 6(1):87 – 112, 1996. 67, 68, 74
- [89] Gerard Jungman, Marc Kamionkowski, and Kim Griest. Supersymmetric dark matter. *Physics Reports*, 267(5-6):195 – 373, 1996. 67, 68
- [90] J. Brand and L. Blitz. The Velocity Field of the Outer Galaxy. *Astronomy and Astrophysics*, 275:67, August 1993. 67
- [91] Martin C. Smith et al. The RAVE survey: constraining the local Galactic escape speed. *Monthly Notices of the Royal Astronomical Society*, 379(2):755–772, 2007. 67, 74
- [92] Jonathan L. Feng, Jason Kumar, Danny Marfatia, and David Sanford. Isospin-violating dark matter. *Physics Letters B*, 703(2):124 – 127, 2011. 69
- [93] J. Blomqvist and A. Molinari. Collective 0^- vibrations in even spherical nuclei with tensor forces. *Nuclear Physics A*, 106(3):545 – 569, 1968. 69

- [94] Richard H. Helm. Inelastic and elastic scattering of 187-mev electrons from selected even-even nuclei. *Phys. Rev.*, 104:1466–1475, Dec 1956. [70](#)
- [95] J. Engel. Nuclear form factors for the scattering of weakly interacting massive particles. *Physics Letters B*, 264(1-2):114 – 119, 1991. [70](#), [72](#)
- [96] R. Machleidt, K. Holinde, and Ch. Elster. The bonn meson-exchange model for the nucleonnucleon interaction. *Physics Reports*, 149(1):1 – 89, 1987. [70](#)
- [97] D.R. Tovey et al. A new model-independent method for extracting spin-dependent cross section limits from dark matter searches. *Physics Letters B*, 488(1):17 – 26, 2000. [71](#)
- [98] P. Toivanen, M. Kortelainen, J. Suhonen, and J. Toivanen. Dark-matter detection by elastic and inelastic LSP scattering on ^{129}Xe and ^{131}Xe . *Physics Letters B*, 666(1):1 – 4, 2008. [72](#), [73](#), [75](#), [81](#)
- [99] E. Holmlund, M. Kortelainen, T.S. Kosmas, J. Suhonen, and J. Toivanen. Microscopic calculation of the LSP detection rates for the ^{71}Ga , ^{73}Ge and ^{127}I dark-matter detectors. *Physics Letters B*, 584(1-2):31 – 39, 2004. [72](#)
- [100] M. T. Ressel and D. J. Dean. Spin-dependent neutralino-nucleus scattering for $a \sim 127$ nuclei. *Phys. Rev. C*, 56:535–546, Jul 1997. [72](#), [73](#)
- [101] Morten Hjorth-Jensen, Thomas T.S. Kuo, and Eivind Osnes. Realistic effective interactions for nuclear systems. *Physics Reports*, 261(3-4):125 – 270, 1995. [72](#)
- [102] V. G. J. Stoks, R. A. M. Klomp, C. P. F. Terheggen, and J. J. de Swart. Construction of high-quality NN potential models. *Phys. Rev. C*, 49:2950–2962, Jun 1994. [72](#)
- [103] J. Toivanen. Computer code eicode. 2004. [72](#)
- [104] R. Machleidt. High-precision, charge-dependent bonn nucleon-nucleon potential. *Phys. Rev. C*, 63:024001, Jan 2001. [72](#)
- [105] J. Suhonen. (private communication). [72](#), [74](#)
- [106] Glen Cowan, Kyle Cranmer, Eilam Gross, and Ofer Vitells. Asymptotic formulae for likelihood-based tests of new physics. *The European Physical Journal C - Particles and Fields*, 71:1–19, 2011. 10.1140/epjc/s10052-011-1554-0. [75](#)
- [107] S. Archambault et al. Dark matter spin-dependent limits for WIMP interactions on ^{19}F by PICASSO. *Physics Letters B*, 682(2):185 – 192, 2009. [78](#)